

12-8-2016

Design and Construction of a Multispectral Camera for Spectral and Colorimetric Reproduction

Yixuan Wang
yw8017@rit.edu

Follow this and additional works at: <http://scholarworks.rit.edu/theses>

Recommended Citation

Wang, Yixuan, "Design and Construction of a Multispectral Camera for Spectral and Colorimetric Reproduction" (2016). Thesis. Rochester Institute of Technology. Accessed from

Design and Construction of a Multispectral Camera for Spectral and Colorimetric Reproduction

Yixuan Wang

December 8, 2016

COLLEGE OF SCIENCE
ROCHESTER INSTITUTE OF TECHNOLOGY
ROCHESTER, NEW YORK

CERTIFICATE OF APPROVAL

Masters DEGREE THESIS

The M.S. Degree Thesis of Yixuan Wang
has been examined and approved by two members of the
Color Science faculty as satisfactory for the thesis
required for the Master of Science degree

Dr. Roy S. Berns, Advisor Date

Dr. Mark D. Fairchild Date .

**Design and Construction of a Multispectral
Camera for Spectral and Colorimetric
Reproduction**

Yixuan Wang

M.S. Tsinghua University, PUMC, Beijing, China, 2012

B.S. Nankai University, Tianjin, China, 2009

A Thesis Submitted in
Partial Fulfillment of the Requirements for the
Degree of Masters of Science in Color Science

Munsell Color Science Laboratory
Program of Color Science
College of Science
Rochester Institute of Technology
Rochester, New York
December 2016

Signature of Author _____

Accepted by _____
Dr. Mark D. Fairchild, Graduate Program Director Date

Yixuan Wang

Design and Construction of a Multispectral Camera for Spectral and Colorimetric Reproduction

M.S. DEGREE THESIS, December 8, 2016

Advisor: Dr. Roy S. Berns

Committee Chair: Thesis Chair

Committee Members: Dr. Mark D. Fairchild and Thesis Committee Member 2

Rochester Institute of Technology

College of Science

1 Lomb Memorial Dr

14623 and Rochester

Dedication

This thesis is dedicated to my family for their love and support.

Abstract

Multi-spectral imaging and spectral reflectance reconstruction can be used in cultural-heritage institutes to digitalize their collections for documentation purposes. It can be used to simulate artwork under any lighting condition, and to analyze colorants that were used. The basic idea of a multi-spectral imaging system is to sub-sample spectral reflectance factor, producing results similar to a spectrophotometer. The sampled data are used to reconstruct reflectance for the visible spectrum.

In this thesis, a wide band multispectral camera was designed and constructed to achieve high spectral and color accuracy as well as high image quality.

Noise propagation theory was introduced and tested. A seven channel band-pass filter set was modeled using Gaussian functions and optimized to yield high spectral and colorimetric reproduction accuracy as well as low colorimetric noise. Single and "sandwich" filters were selected from off-the-shelf absorption filters using the Gaussian bandpass filter model. Experiments were conducted to test the spectral, color and noise performance of the novel sandwich filters and compared with interference filters. The novel sandwich filters led to increased colorimetric accuracy along with a reduction colorimetric noise.

This imaging system will be used as part of a recommended workflow for museum archiving, and will be an important addition to the spectral imaging capabilities at MCSL.

Acknowledgement

First, I would like to thank my advisor, Dr. Roy S. Berns for inspiring my interest in solving the problems, for giving me the valuable opportunity to work with him, and being my role model as a researcher. I also thank my advisory committee member Dr. Mark Fairchild for his thoughtful comments and suggestions.

I would like to thank people in the Program of Color Science for their support, in particular Valerie Hemink for her patient assistance with the administrative tasks, constant support, and positivity. I would like to express my sincere thanks to Dr. Susan Farnand, Dr. Michael Murdoch and Dr. David Wyble for sharing their knowledge, answering my questions, and providing advice.

I would like to thank all my fellow students over the years, and with special thanks to Ben Bodner, Nargess Hassani, Christopher Thorstenson, Brittany Cox, Katherine Carpenter, Morteza Maali Amiri and Gaurav Sheth for all their help and friendship.

I would like to thank Farhad Abed, Yuta Asano, Jennifer Kruschwitz, Adria Fores and Max Derhak for kind advice and support at the beginning of my time in MCSL.

I would like to thank the Andrew W. Mellon Foundation for financial support of this thesis.

I would like to express my gratitude to my husband Can, my son Anthony and my parents for their love and inseparable emotional support.

Contents

List of figures	xii
List of tables	xvi
1 Introduction	1
Narrow Band Capture	1
Trichromatic Camera with Absorption Filters	2
Wide Band Capture	2
2 Literature Review and Related Work	4
2.1 Multispectral Imaging Systems	4
2.1.1 Spectral Scanning	5
Fourier-transform-spectroscopy-based Imaging System	6
2.1.2 Narrow-band Capture	8
Multiple-Narrow-Band-Filter-Based Imaging System .	8
LCTF-Based Imaging System	8
2.1.3 Wide-band Capture	9
2.1.4 Dual-RGB Capture	12
2.2 Spectral Reconstruction Techniques	14
Pseudo-inverse	15
Principal Component Analysis	16
2.3 Multispectral Imaging System Characterization and Calibration	17
2.4 Noise Modeling and Propagation	18
2.4.1 Noise Modeling	19
2.4.2 Color Noise Propagation	20

3 Modeling and Optimizing Spectral Sensitivity Considering Noise Propagation	24
3.1 Spectral Sensitivity Modeling	24
3.2 Trichromatic Spectral Sensitivity Optimization Modeling	25
3.2.1 Color Space Transformation Modeling	26
3.2.2 Optimization Procedure	26
3.2.3 Results and Discussions	30
RGB Filter Set	30
CMY Filter Set	32
3.3 Filter Optimization for a Seven-Channel Multispectral Camera	34
Theoretical Gaussian Filters	34
3.4 Conclusions	38
4 Schott "Sandwich Filter" Selection	39
4.1 Theory	39
4.2 Fitting Gaussians	40
4.3 Subsets Selection Method	53
4.4 Conclusions	58
5 Single Schott Filter Selection	59
5.1 Filter Selection Method and Results	59
5.2 Conclusions	67
6 Experimental Verification	68
6.1 Apparatus	68
6.2 Experimental	73
6.2.1 Scene Set Up	73
6.2.2 Imaging	73
6.2.3 Image Processing and Spectral Reconstruction	76
6.2.4 Spectral and Colorimetric Accuracy Evaluation	80
Spectral Accuracy Evaluation	80
Colorimetric Accuracy Evaluation	80
6.3 Spectral and Colorimetric Reproduction Results and Discussion	81

6.3.1	Evaluation of Filter Sets	81
Spectral and Colorimetric Accuracy Evaluation Results	81	
T-Test Results	87	
Discussion	90	
6.3.2	Evaluation of Calibration Targets	92
T-Test Results	92	
Discussion	97	
6.4	Conclusions	102
7	Conclusions and Future Work	103
7.1	Conclusions	103
7.2	Future Work	106
References		107
A Appendix A: Specific filter sets selected in Chapter 4		114
B Appendix B: Spectral and colorimetric reproduction plots for Chapter 6		116

List of Figures

2.1	Schematic representation of a multispectral image cube displaying both spectral and spatial information	5
2.2	Michelson interferometer [Sun, 2010]	6
2.3	(a) liquid crystal spectral encoder (b) LCTF, lens, camera assembly (c) a corresponding photo of the system from [Hegyi and Martini, 2015]	7
2.4	LCTF, camera,lens assembly from [Hensley and Wyble, 2012] .	9
2.5	Schematic of the VASARI scanner lighting system [Martinez et al., 2002]	11
2.6	Sinar CTM camera system	13
2.7	A schematic view of a multispectral imaging system	14
2.8	Linear image formation pipeline and noise modeling	20
3.1	Left: RGB-type sensor with peak wavelength of 595nm, 550nm, 450nm and half bandwidth of 40nm for all; Right: CMY-type sensor with peak wavelength 595nm,550nm,450nm and half bandwidth of 40nm for all.	25
3.2	A workflow of the trichromatic sensor modeling and optimization.	29
3.3	RMS derived from the red filters with various peak wavelengths and bandwidths.	31
3.4	ΔE_{00} derived from the red filters with various peak wavelengths and bandwidths.	31
3.5	Noise σ derived from the red filters with various peak wavelengths and bandwidths.	31
3.6	RMS derived from the cyan filters with different peak wavelength and bandwidth.	32

3.7	ΔE_{00} derived from the cyan filters with different peak wavelength and bandwidth.	33
3.8	Noise σ derived from the cyan filters with different peak wavelength and bandwidth.	33
3.9	A workflow of the optimization of seven channel bandpass filter set modeling.	35
3.10	Optimal seven bandpass filters.	36
3.11	Lines: estimated color matching function using the optimal seven bandpass filters. Circle marked lines: standard color matching function.	37
4.1	Filters selected from Schott database.	43
4.2	Filters selected from Schott database. The second sandwich filter was replaced by 450nm interference filter.	44
4.3	Filters selected from Schott database. The seventh sandwich filter incorporated KG5.	45
4.4	Filters selected from Andover database.	46
4.5	Filters selected from Andover database. The seventh sandwich filter incorporated KG5.	47
4.6	Estimated and reference spectral reproduction.	50
4.7	Estimated and reference colorimetric reproduction for the APT using the Andover B filter set.	51
4.8	Spectral transmittance of the final selected filters	52
4.9	A flowchart of the subsets selection method.	54
4.10	Histograms of ΔE_{00} , noise and RMS.	55
4.11	K-means classification results.	56
5.1	A flowchart of the single Schott filter selection.	60
5.2	The spectral transmittance of the UV/IR cut visible bandpass filter.	61
5.3	Histograms of ΔE_{00} , noise and RMS for single Schott filter selection.	62
5.4	K-means classification results for single Schott filter selection.	63
5.5	Selected filter transmittance and system spectral sensitivity for single Schott filter selection.	64

5.6	Estimated and reference spectral and colorimetric reproduction for single Schott filter selection.	65
5.6	Estimated and reference spectral and colorimetric reproduction for single Schott filter selection. (cont.)	66
6.1	The nominal quantum efficiency of the KAF-50100 sensor. (http://www.icamera.com/spec_sheets/ML50100.pdf)	68
6.2	The modulation transfer function (MTF) of the Rodenstock lens. (http://www.rodenstock-photo.com/Archiv/e_Rodenstock_Printing_CCD_43-62_8230.pdf)	69
6.3	The spectral transmittances of the interference filter set.	70
6.4	Camera setup.	71
6.5	Four targets. Top left: APT. Top right: CCSG. Bottom left: Target Justin. Bottom right: Target Timo.	72
6.6	Scene geometry.	73
6.7	Spectral reflectance of the ColorChecker SG white patch (blue line) and the white board (red line).	75
6.8	Experimental workflow.	76
6.9	The distribution of the pairwise difference of Q metric between the absorption filters and interference filters among all verification patches (1122), and its fitting of a normal distribution.	89
6.10	Colorimetric reproduction comparison for APT used as calibration target and the target Timo used as the verification target for the sandwich absorption filters and the interference filters.	98
6.11	CCSG normal map. Curved patches are labeled with red circles.	99
6.12	Colorimetric reproduction comparison for the target Timo used as the verification target for the sandwich absorption filters.	100
6.13	The discrepancy between the measured and reconstructed spectral reflectances for the two sets of filters for Target Timo. APT was used as the calibration target. The Target Timo was used as the verification target.	101

B.1	Colorimetric reproduction comparison for the four targets used as the calibration targets for the sandwich absorption filters. . .	117
B.1	Colorimetric reproduction comparison for the four targets used as the calibration targets for the sandwich absorption filters. . .	118
B.1	Colorimetric reproduction comparison for the four targets used as the calibration targets for the sandwich absorption filters. . .	119
B.1	Colorimetric reproduction comparison for the four targets used as the calibration targets for the sandwich absorption filters. . .	120
B.2	ΔE_{00} for APT calibration.	121
B.3	ΔE_{00} histogram for APT calibration.	122
B.4	Lightness reproduction for APT calibration.	123
B.5	Spectral reflectance estimation error for APT calibration. . . .	124
B.6	Spectral reflectance estimation multiplots for APT calibration. .	125

List of Tables

3.1	Optimal seven filter spectral sensitivity for $\alpha = 0.3, \beta = 0.3$	37
3.2	Color transformation matrix for the optimal seven filter spectral sensitivity for $\alpha = 0.3, \beta = 0.3$	37
4.1	The $\Delta E_{00,\sigma}$ and $RMSE$ of the APT using each listed filter set. .	49
4.2	The final selected filters, available from the Andover Corporation.	49
5.1	The names of the selected filters in Fig.5.5.	61
5.2	Results of selected filters in Fig.5.5.	61
6.1	Results of the spectral and colorimetric reproduction and noise for the sandwich absorption and interference filters. Calibration target: Timo. Verification targets: APT, Justin, and CCSG.	82
6.2	Results of the spectral and colorimetric reproduction and noise for the sandwich absorption and interference filters. Calibration target: APT. Verification targets: Timo, Justin, and CCSG.	83
6.3	Results of the spectral and colorimetric reproduction and noise for the sandwich absorption and interference filters. Calibration target: Justin. Verification targets: Timo, APT, and CCSG.	84
6.4	Results of the spectral and colorimetric reproduction and noise for the sandwich absorption and interference filters. Calibration target: CCSG. Verification targets: Timo, APT, and Justin.	85
6.5	The average verification average results of the spectral and colorimetric reproduction and noise for the sandwich absorption and interference filters for different calibration targets. The combined metric $Q = 0.3 \times 100 \times RMSE + 0.3 \times \Delta E_{00} + 0.4 \times noise$	86

6.6	The difference between the average verification data of the sandwich filters and interference filters. T-Test was applied on all verification data. Numbers in red color: the results of the absorption filters are significantly lower than that from the interference filters. Numbers in green color: the results of the interference filters are significantly lower than that from the absorption filters.	90
6.7	T-Test p-Values. Numbers in red color: the results of the absorption filters are significantly lower than that from the interference filters. Numbers in green color: the results of the interference filters are significantly lower than that from the absorption filters.	90
6.8	Percentage mean difference of the results of sandwich absorption filters compared to the interference filters	91
6.9	Calibration target ΔE_{00} t-test comparison for absorption filters. The reported data are the difference between the column targets and the row targets (column-row). For negative mean values, the T-test examines whether the results from the column targets are significantly lower than that from the row targets, and the values with significance (p-value < 0.05) are labeled in red color; for positive mean values, the T-test examines whether the results from the row targets are significantly lower than that from the column targets, and the values with significance (p-value < 0.05) are labeled in green color.	93
6.10	Calibration target RMSE t-test comparison for absorption filters. The reported data are the difference between the column targets and the row targets (column-row). For negative mean values, the T-test examines whether the results from the column targets are significantly lower than that from the row targets, and the values with significance (p-value < 0.05) are labeled in red color; for positive mean values, the T-test examines whether the results from the row targets are significantly lower than that from the column targets, and the values with significance (p-value < 0.05) are labeled in green color.	94

6.11	Calibration target noise T-Test comparison for absorption filters. The reported data are the difference between the column targets and the row targets (column-row). For negative mean values, the T-Test examines whether the results from the column targets are significantly lower than that from the row targets, and the values with significance (p-value < 0.05) are labeled in red color; for positive mean values, the T-Test examines whether the results from the row targets are significantly lower than that from the column targets, and the values with significance (p-value < 0.05) are labeled in green color.	94
6.12	Calibration target ΔE_{00} T-Test comparison for interference filters. The reported data are the difference between the column targets and the row targets (column-row). For negative mean values, the T-Test examines whether the results from the column targets are significantly lower than that from the row targets, and the values with significance (p-value < 0.05) are labeled in red color; for positive mean values, the T-Test examines whether the results from the row targets are significantly lower than that from the column targets, and the values with significance (p-value < 0.05) are labeled in green color.	95
6.13	Calibration target RMSE T-Test comparison for interference filters. The reported data are the difference between the column targets and the row targets (column-row). For negative mean values, the T-Test examines whether the results from the column targets are significantly lower than that from the row targets, and the values with significance (p-value < 0.05) are labeled in red color; for positive mean values, the T-Test examines whether the results from the row targets are significantly lower than that from the column targets, and the values with significance (p-value < 0.05) are labeled in green color.	95

6.14	Calibration target noise T-Test comparison for interference filters. The reported data are the difference between the column targets and the row targets (column-row). For negative mean values, the T-Test examines whether the results from the column targets are significantly lower than that from the row targets, and the values with significance (p-value < 0.05) are labeled in red color; for positive mean values, the T-Test examines whether the results from the row targets are significantly lower than that from the column targets, and the values with significance (p-value < 0.05) are labeled in green color.	96
A.1	Schott B.	114
A.2	Andover A.	114
A.3	Schott D.	115
A.4	Andover C.	115

Introduction

Multispectral imaging and spectral reflectance reconstruction can be used in cultural-heritage institutions to digitalize their collections for documentation purposes. It can be used to simulate artwork under any lighting condition, and to analyze what type of colorants were used. The basic idea of a multispectral imaging system is to sub-sample spectral reflectance factor, producing results similar to a spectrophotometer. The sampled data are used to reconstruct reflectance for the visible spectrum. There are three basic schemes to build a multispectral imaging system: bandpass filters with a monochrome imager, absorption filters with a monochrome imager, and absorption filters with a trichromatic digital camera. The Munsell Color Science Laboratory (MCSL) currently has multispectral imaging systems that correspond to the first and the third schemes: a liquid crystal tunable filter (LCTF) with a monochrome CCD camera and a dual-RGB Sinar 86H Color To Match (CTM) camera.

Narrow Band Capture

The first multispectral camera currently available at MCSL uses narrow band sampling and a monochrome digital camera. An LCTF imaging system uses tunable filters to provide bandpass filtration with a continuous tunable center wavelength in the range of 400nm to 730nm. However, this system has several drawbacks that make it impractical for cultural-heritage studio imaging. This system has very low optical throughput because of its low transmittance at short wavelengths. The image resolution is low and the image quality is poor because of the low signal-to-noise-ratio (SNR) of this system. Further spatial corrections are required to compensate for angular dependency of LCTF transmittance. Therefore, the LCTF is not practical for cultural-heritage studio imaging.

A similar system that consists of a monochrome camera and thirty-one interference filters with 10nm bandpass has been used for cultural-heritage imaging at several institutions and academic laboratories [Burns, 1997]. The resulting image quality is better and the system's optical throughput is high compared to the LCTF, by employing a higher resolution sensor and filters with higher transmission. However, this approach is still not practical. The registration for thirty-one images is complicated and time consuming, and only achieves good results with difficulty. This scheme is not considered in this thesis since the goal of this thesis is to develop an instrument that is applicable in a studio environment, rather than a scientific instrument.

Trichromatic Camera with Absorption Filters

The second MCSL system utilizes two absorption filters with a trichromatic digital camera. It is also called the "dual-RGB" method. Currently, the only commercial system that uses the dual-RGB technique with the utilization of professional medium format cameras is the Sinar CTM camera. This scheme is convenient since only two captures are needed to give the information of five channels (the spectral sensitivities of the two green channels with two different filters are nearly identical, so only one of them is used).

This scheme produces highly accurate colorimetric reproduction. However, it does not produce sufficient spectral accuracy. For example, the spectral reproduction is not accurate enough for pigment mapping [Abed, 2014].

Wide Band Capture

A multi-spectral imaging system with wide band capture is developed in this thesis. This system has relatively high spectral and colorimetric reproduction accuracy. The spectral reproduction achieved by estimating the spectral reflectance of the scene using the output signals of the imaging system.

The output signals of the imaging system are the integration of the spectral radiance of the light source interacting with the spectral reflectance of the scene, weighted by the spectral transmittance of the optical path and the spectral sensitivity of the sensor. The colorimetric reproduction achieved by estimating the tristimulus values directly from the output camera signal using nonlinear optimization.

A good compromise between spectral accuracy and simplicity resulted. This system employed seven wide band filters with a monochrome camera. The number of filters was determined using principal component analysis of pigment data sets. For artwork, the spectral reflectance shapes of pigments are always smooth, so no less than six eigenvectors are needed to generate desirable colorimetric and spectral accuracy [Burns, 1997]. With wider bandwidth and higher transmittance compared to an LCTF, this system has higher optical throughput. However, registration is required because imaging systems with filter wheels are not repeatable.

High spectral and color accuracy is not sufficient for cultural heritage imaging. Image quality, in terms of sharpness and noise, is also an essential requirement. For the dual-RGB multi-spectral imaging system, MCSL has achieved high image quality and color accuracy. The objective of this thesis is to achieve similar image quality and color accuracy and improved spectral estimation accuracy.

Customized filters are prohibitively expensive. Thus, all filters of this multi-spectral imaging system are selected from off-the-shelf products, which enables this system to be easily reproduced and widely used in cultural-heritage studio imaging. The goal of this thesis is to develop a multi-spectral imaging system that will be used as part of a recommended workflow for museum archiving and will be an important addition to spectral capabilities at MCSL.

Literature Review and Related Work

2.1 Multispectral Imaging Systems

The traditional means of digitalizing cultural heritage is trichromatic imaging. It relies on metamerism in the sense that two objects that achieve a visual match can have different spectral reflectances. Multispectral imaging could be considered an extension of trichromatic imaging. It samples and records spectral reflectance for accurate spectral reflectance estimation and color reproduction, addressing the issue of metamerism, i.e., the viewing experience depending on the viewing condition [MacDonald, 2006].

Spectral reflectance factor is undersampled in a lower dimensional space in a multispectral imaging system. In spectral images, each pixel value is a vector that represents a projection from the space of the spectral reflectance to the space associated with the imaging system, which is determined by a combination of the illumination and the device spectral sensitivities [Liang, 2012].

More spectral information could be produced by increasing the number of capturing channels, and accordingly, demanding a more sophisticated device. Therefore, there is always a trade-off between measurement accuracy, cost, capturing speed, and hardware and software complexity [Berns, 2005].

Using high-resolution and high SNR sensors, spectral and spatial information can be attained simultaneously. The spectrum of each pixel in the image can be calculated from the spectral images that contain both spectral and spatial information (Fig. 2.1) [Fischer and Kakoulli, 2006].

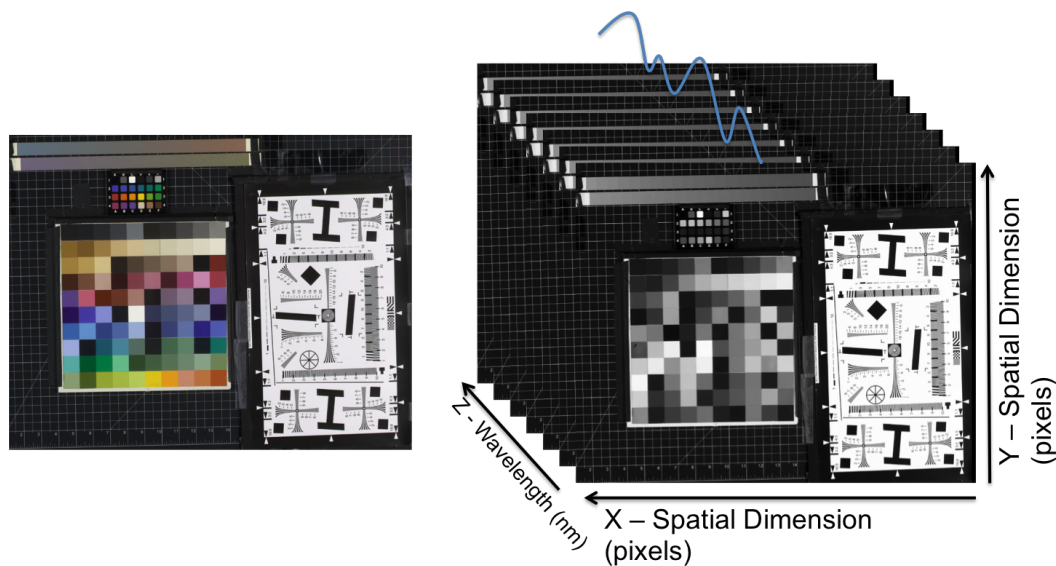


Fig. 2.1. – Schematic representation of a multispectral image cube displaying both spectral and spatial information

2.1.1 Spectral Scanning

A simple scheme to measure the spectral information is complete spectral scanning, also known as hyper-spectral imaging. Spectral information of each pixel is measured and recorded independently. The imaging system consists of a light source, a filter system to disperse the light and an imager for the acquisition of spectral information. Three basic configurations for complete spectral scanning are point scan, line scan and plane scan [Geladi et al., 2007].

A complete spectral scanning based imaging system was developed in Italy. This system is a line-scanning imaging system, consisting of a spectrograph, a monochrome CCD and a scanning table. Images are captured with spectral resolution of 2nm, a spectral range of 400nm to 700nm, and spatial resolution of 3.5 lines/mm. Capturing time is dependent on the scanning area. For example, this system can scan an area of $120 \times 140 \text{ cm}^2$ in three hours. The

color accuracy was assessed using a set of standard tiles with an average of $0.49 \Delta E_{94}^*$ [Antonioli et al., 2004], [Novati et al., 2005], [Brusco et al., 2006].

Fourier-transform-spectroscopy-based Imaging System

A self interference device can generate an interferogram which reveals spectral information by performing an inverse Fourier transform. A Michelson interferometer is one of the simplest and most widely-used two-beam interferometers (Fig. 2.2). The beam splitter splits the light from the light source into two beams, which are reflected by the mirrors and recombined by the same beam splitter. The optical path difference between the two beams is introduced from the moving mirror. The detector generates and records the interferograms [Sun, 2010].

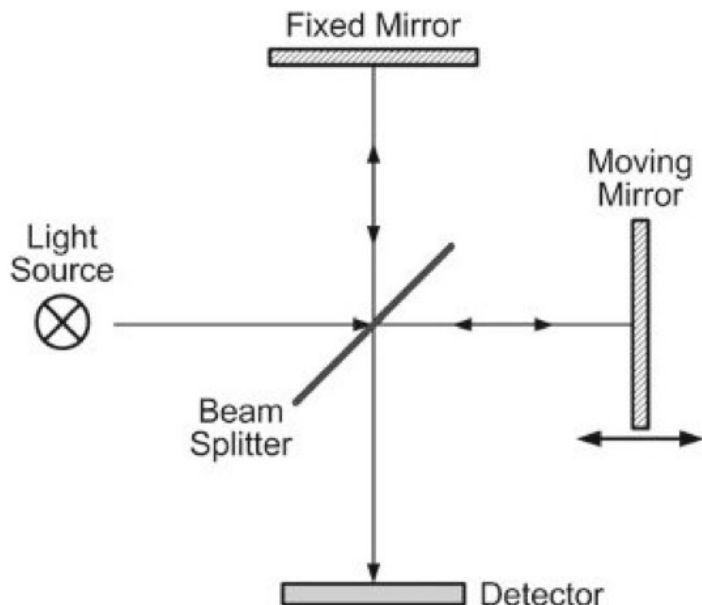


Fig. 2.2. – Michelson interferometer [Sun, 2010]

A novel method based on Fourier transform spectroscopy is presented in [Hegyi and Martini, 2015] (Fig. 2.3), which has a varying-voltage driving

scheme and a double-nematic structure addressing the second-order angular dependence of the path delay. The approach is also based on the Fourier transform of the optical wavelength. It has the advantage of high optical throughput and spectral multiplexing. This approach used the varying-voltage driven double-nematic liquid crystal to solve the problem of vibration-sensitivity of traditional Michelson interferometer based Fourier transform spectroscopy and the problem of wavelength-dependent spatial non-uniformity of the single-nematic liquid crystal. The trade-offs between imaging speed and spectral resolution is selectable through software. These efforts make it possible to combine the system with common CMOS image sensors to form a practical hyperspectral imaging system.

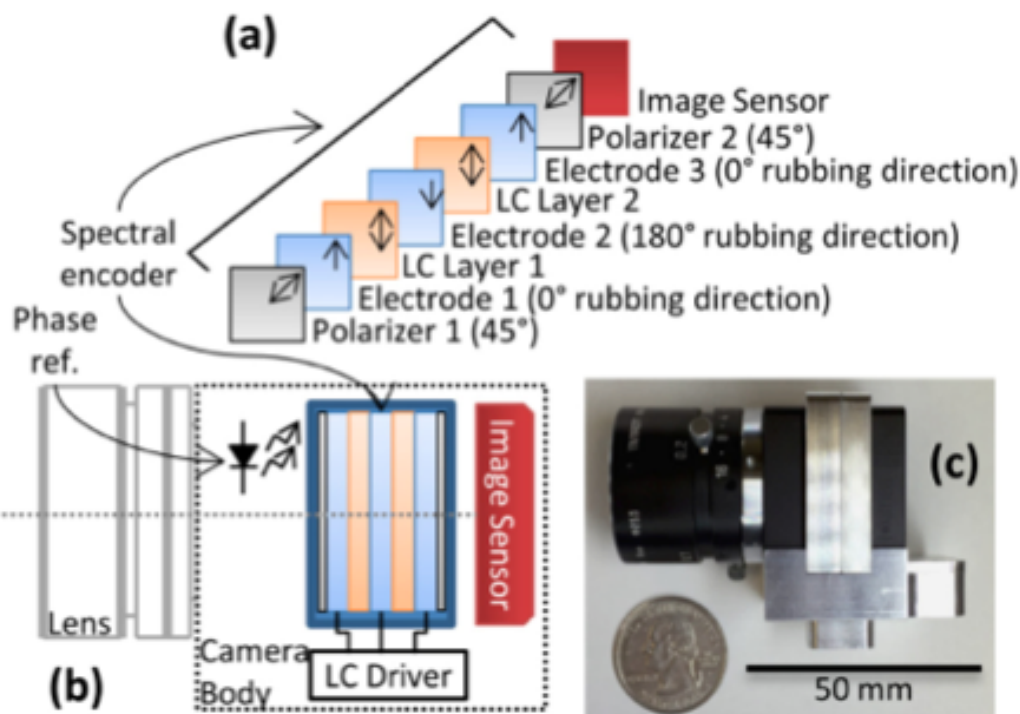


Fig. 2.3. – (a) liquid crystal spectral encoder (b) LCTF, lens, camera assembly (c) a corresponding photo of the system from [Hegyi and Martini, 2015]

Scanning spectral systems are not used in studios because of their complexity, cost, and low resolution.

2.1.2 Narrow-band Capture

A classic scheme of building a narrow-band imaging system is to position narrow-band filters in front of a monochrome imager. The filters can be a set of narrow-band optical or interference filters mounted in a filter wheel or Liquid Crystal Tunable Filters (LCTF).

Multiple-Narrow-Band-Filter-Based Imaging System

The multiple narrow-band-filter-based imaging system captures multi-channel spectral images by rotating the filters in a filter wheel mounted in front of the sensor or lens. The per-pixel spectral reflectances are estimated from the spectral images [Yamaguchi et al., 2001], [Tominaga et al., 2004], [Fukuda et al., 2005], [MacDonald et al., 2013]. The drawbacks of this scheme include time consuming measurements, complex image registration, geometric distortion and the high cost of customized filters [Brauers et al., 2008], [Novati et al., 2005], [Fischer and Kakoulli, 2006], [Bianco et al., 2011], [MacDonald, 2006].

LCTF-Based Imaging System

A stack of polarizers and tunable liquid crystal plates are used to build the birefringent filter in this approach [Kaye, 1983]. The transmittance of the LCTF is electronically tuned by modulating voltage. The LCTF is polarization sensitive [Gat, 2000]. The Munsell Color Science Laboratory (MCSL) developed and evaluated an LCTF-based imaging system (Fig. 2.4), which employed a Quantix astronomical-grade monochrome sensor in 31 bands to collect spectral information [Imai et al., 2002] [Hensley and Wyble, 2012]. The spectral sensitivity of the LCTF-based imaging system varies across the image plane. The wavelength-dependent spatial non-uniformity can be corrected by

a regression-based method [Berns et al., 2015]. The LCTF imaging system provides rapid and vibrationless capturing, as well as flexible selection of any wavelength [Abed, 2014]. However, this imaging system has low optical throughput because of its low transmission. The LCTF aperture size often limits the sensor size, and hence, resolution. Moreover, the high cost, complexity and the large storage capacity requirements make the LCTF-based imaging system inapplicable for cultural-heritage imaging.



Fig. 2.4. – LCTF, camera,lens assembly from [Hensley and Wyble, 2012]

2.1.3 Wide-band Capture

This scheme uses a smaller set of wide bandpass filters with large bandwidth to capture spectral images. Spectral reconstruction algorithms are necessary for imagery and spectral reflectance estimation. The sampling interval can be reduced without sacrificing the spectral accuracy because the spectral reflectances of the pigments used in cultural-heritage generally have a smooth shape [Day, 2003]. It is reported that the wide-band capturing approach has similar results as the narrow-band scheme in terms of spectral error [Imai et al., 2000]. This scheme is comparably inexpensive when off-the-shelf filters

are employed. The capturing is more efficient. With a high resolution imager, the system can produce high spatial resolution because of its high SNR. It can achieve a good balance among cost, speed and accuracy. The drawback of this scheme is that the filter changing process always leads to system vibration, necessitating further image registration. Considerable research has been performed on the number and spectral properties of multispectral cameras for cultural-heritage applications [Taplin and Berns, 2005], [Fischer and Kakoulli, 2006], [Bianco et al., 2011], [Schmitt et al., 1999]. However, no recognized standard has been established.

A seven channel imaging system (Fig. 2.5) was developed in the Visual Arts System for Archiving and Retrieval of Images (VASARI) program, which was supported by the National Gallery in London, England and a consortium of European universities and companies for the documentation and archiving of cultural heritage [MacDonald, 2006], [Martinez et al., 2002]. The imaging system consisted of a 12-bit monochrome camera and a tungsten light source with seven wide bandpass filters. This configuration has an active illumination system, whose filtration layout is in front of the light source instead of the sensor. The imaging system captures artwork piece by piece using a scanning table and merges all pieces together for a high-resolution image (20,000 x 20,000 pixels). The color difference between the estimated and measured data was $1.1\Delta E_{ab}^*$. The drawback of this system is that the system movement process introduces complex geometric distortion in the image, which was barely remedied by image superposition and registration.

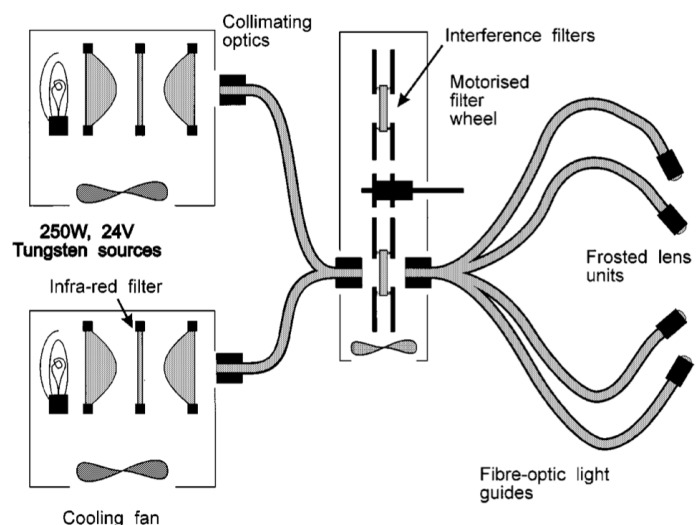


Fig. 2.5. – Schematic of the VASARI scanner lighting system [Martinez et al., 2002]

2.1.4 Dual-RGB Capture

A set of broadband absorption filters with a high-resolution trichromatic sensor is a practical and inexpensive multispectral imaging scheme. Two three-channels images are generated from two captures and are assembled into a six channel spectral image. The capture and registration processes are more convenient compared with other multispectral imaging schemes [Taplin and Berns, 2005]. However, only five channels are used for spectral reconstruction, since the spectral sensitivities of the two green channels are nearly identical. Unfortunately, its spectral reproduction accuracy is insufficient for pigment mapping [Abed, 2014].

The dual-RGB capturing system used in the MCSL is a Sinar 86H CTM (Color To Match) system (Fig. 2.6), which is based on a trichromatic camera combined with two absorption filters. The filters were selected from off-the-shelf filters for high spectral reproduction accuracy [Berns et al., 2004], [Berns et al., 2005]. A matrix-R-based spectral reconstruction technique was developed for preserving high colorimetric accuracy, with the usage of the Sinar CTM imaging system and combined into the MCSL spectral imaging framework [Zhao et al., 2005], [Zhao and Berns, 2007].



Fig. 2.6. – Sinar CTM camera system

2.2 Spectral Reconstruction Techniques

Spectral reconstruction refers to the techniques by which spectral reflectance of the scene is estimated using the output signals of the imaging system. A linear optical model of image acquisition (Fig. 2.7) is used in most of the spectral reconstruction algorithms [Haneishi et al., 2000], [Ribes and Schmitt, 2008], [Ribes et al., 2008], [Schmitt et al., 1999], [Hardeberg, 2001].

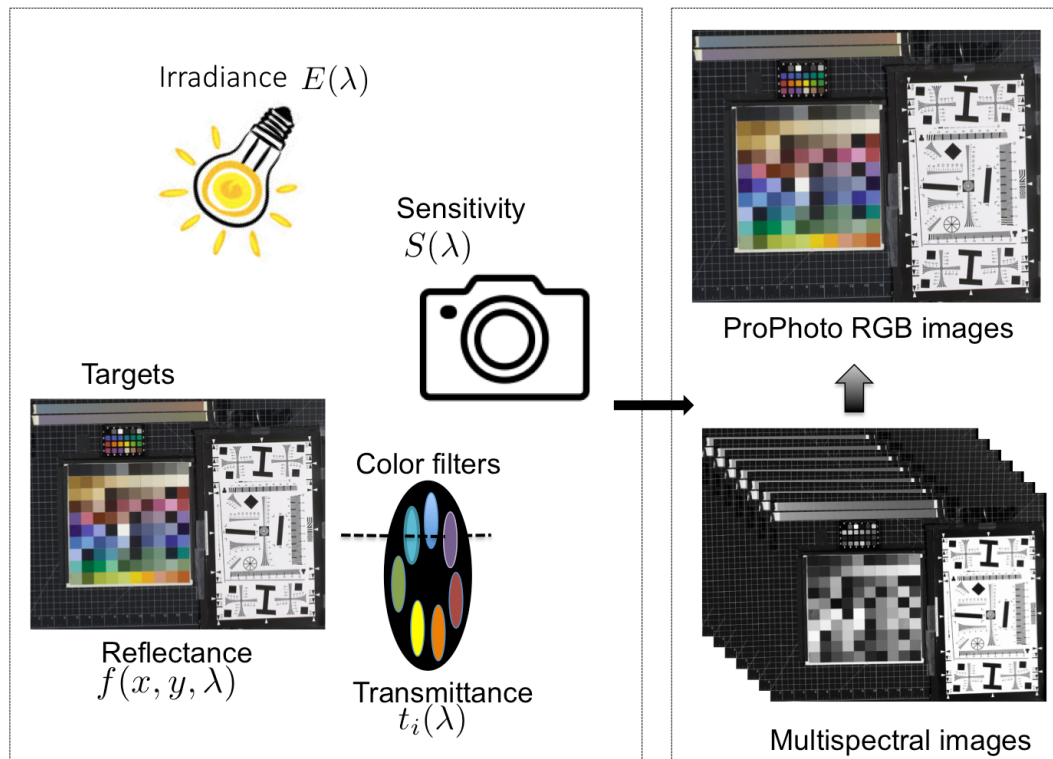


Fig. 2.7. – A schematic view of a multispectral imaging system

The output signal of the imaging system, G , is the integration of the spectral irradiance, E , of the light source interacting with the spectral reflectance, F , of the scene, weighted by the spectral transmission, T , of the optical path and the spectral sensitivity, S , of the sensor, and additive noise, N .

$$G = EFTS + N \quad (2.1)$$

The imaging system sensitivity C can be defined as the product of the spectral radiance of the light source, the spectral transmission of the optical path and the spectral sensitivity of the sensor:

$$C = ETS \quad (2.2)$$

Thus, Eq. 2.1 can be written as:

$$G = CF + N \quad (2.3)$$

An estimated spectral reflectance F of the scene is transformed from the output camera signal G in Eq. 2.3, which is the basis of most of the spectral reconstruction algorithms.

Pseudo-inverse

The estimated spectral reflectance is not unique since the dimensionality of the spectral reflectance is larger than the number of camera channels. Mathematically, this is an ill-posed problem in which the solution for F is not unique.

- **Direct Measurement** The spectral reflectance can be estimated as the product of the pseudo-inverse of the C and the camera signal G , neglecting the additive noise. Matrix C is estimated by characterizing all the components of the system in Fig. 2.7 directly. However, it is complicated and time consuming to produce monochromatic light to characterize the spectral sensitivity of the camera. Furthermore, this method is very sensitive to small errors[Abed, 2014].
- **Target-based Characterization** The matrix C can also be estimated using a target of colors, whose spectral and colorimetric data are pre-measured. Common targets are the Xrite ColorChecker Classic and Dig-

ital ColorChecker SG. This method is referred to as target-based reconstruction [Hardeberg, 2001], [Ribes and Schmitt, 2008]. This method is practical and inexpensive compared to the direct measurement method. The pseudo-inverse target-based characterization method was proved to lead the smallest spectral and colorimetric errors compared to Kubelka-Munk and PCA methods [Abed, 2014].

Principal Component Analysis

The spectral reflectance F can be estimated using principal component analysis (PCA):

$$F = \Phi\alpha \quad (2.4)$$

where Φ is the set of principal components, α is the set of corresponding scalar weights. Φ is computed from the eigen-decomposition of the covariance matrix of the training targets, arranged in descending order [Burns, 1997]. α can be estimated using the camera signal G :

$$\alpha = AG \quad (2.5)$$

From Eq. 2.5, the least-square transformation matrix A can be expressed using G :

$$A = \alpha G^\dagger \quad (2.6)$$

The Φ and A of the validation data set are assumed to be the same as those of the training data set. Therefore, the spectral reflectance F of the validation data set can be estimated using the output camera signal G :

$$F = \Phi\alpha = \Phi_0 AG = \Phi_0 A_0 G = \Phi_0 \alpha_0 G_0^\dagger G \quad (2.7)$$

where the sub-zero represents the data from the training data set.

The basis vectors are orthogonal. The spectral reconstruction error always decreases when the number of bases increases, but with minor gains beyond eight [Burns, 1997].

2.3 Multispectral Imaging System Characterization and Calibration

Characterization is defined as connecting a device-dependent space to a device-independent space for a calibrated device [Sharma and Bala, 2002]. Spectral characterization is the procedure by which the multispectral camera output signal is converted to spectral reflectance.

Multispectral imaging systems consist of different optical and electronic components. Such systems require calibration to correct the systematic defects and random errors that are introduced during image capture. Multispectral imaging system calibration is to achieve a fixed output signal for a pre-determined input, including regular procedures of calibrating CCD images (the linearity of the detector, dark current correction, flat-fielding) and the calibration for spectral response of the system [Sharma and Bala, 2002].

Sources of error are explained in section 2.4.1. Dark current noise and flare is calibrated by taking dark images of a black trap with the same camera settings. Taking images of a uniform white target using the same camera setting and lighting condition can correct the systematic noise as well as the spatial inhomogeneity of illumination.

Calibration for spectral response of the system requires images of a standard monochromatic source at each wavelength. The spectral reflectance at each pixel R_i is given by

$$R_i(\lambda) = R_W(\lambda)g \frac{(I_i(\lambda) - D_i(\lambda))f_i(\lambda)}{\sum_n[(W_i(\lambda) - DW_i(\lambda))f_i(\lambda)]/n} \quad (2.8)$$

where λ is the central wavelength of the spectral channel, R_w is the spectral reflectance ground truth, I_i is the digital counts for the target image, D_i is the digital counts for the black trap image with the same camera settings, f_i is the flat-fielding correction factor, W_i is the digital counts for the monochromatic source image, DW_i is the corresponding black trap image with the same camera settings, n is the pixel number over which to average the monochromatic source image [Liang, 2012].

Many researches have focused on target based calibration methods, where the parameters of the model are computed based on the spectral reconstruction of standard targets whose spectral and colorimetric properties are pre-measured [Liang et al., 2005], [Ribés et al., 2005], demonstrating that the capturing geometries is one of the key factors that impacts the validity of the calibration. The appearance of objects often depends on the capturing geometries, which increases the complexity of the characterization process. Keeping the measurement geometry consistent with the viewing geometry, or using the same imaging geometry for comparison between materials is recommended [Hong et al., 2001], [Barnard and Funt, 2002], [Cheung et al., 2004], [Nyström, 2007]. Moreover, for the devices whose spectral properties are dependent with capturing geometries, such as LCTF whose transmission shifts with incident angles, extra calibration procedures are needed [Berns et al., 2015], [Hong et al., 2001], [Green and MacDonald, 2011], [Sharma and Bala, 2002], [Liang, 2012].

2.4 Noise Modeling and Propagation

A multispectral imaging system requires a spectral image transformation between color spaces, including spectral reflectance, tristimulus values, CIELAB coordinates and various RGB encoding such as sRGB and ProPhotoRGB. However, noise or uncertainty is inevitable and arises from various sources, e.g., dark current, shot noise, read noise, etc. A noise model is needed to

make the impact of uncertainty arising from various sources understandable and predictable. The knowledge of noise propagation allows the comparison of observed performance in various color spaces, and discrimination of the error introduced by approximations to color space transformation from intrinsic error.

2.4.1 Noise Modeling

There are various sources of noises and they behave differently. Camera image noise are categorized into two types: per-pixel sensor noise and systematic noise across the sensor [Gow et al., 2007] . There are three types of per-pixel sensor noise: The first is dark current noise. It comes from thermally generated electrons. It is scene-independent and has exponential temperature dependence. It is dominant for long exposures. Cooling the sensor, subtracting dark frame, and averaging multiple shorter exposures can mitigate dark noise. The second is photon shot noise. It results from random arrival of photons, revealing quantum nature of light. It is scene-dependent, Poisson- distributed and proportional to the square root of the signal. The third per-pixel type of noise is read noise and analog-digital-convertor (ADC) noise, which is from defective pixels, voltage fluctuations of ADC and amplifiers. It is determined by the speed of the readout process. It is scene-independent, nearly zero-mean Gaussian-distributed. Read noise is amplified by the gain factor in propagation, so it is very important for dark pixels.

Systematic noise is the variation across the sensor, including fixed pattern noise, which is per-pixel biased; pixel readout non-uniformity; and dark current variations, which result from "hot pixels". This noise is minimized during calibration.

The linear image formation pipeline and noise modeling are shown in Fig. 2.8, and Eqs. 2.9 and 2.10.

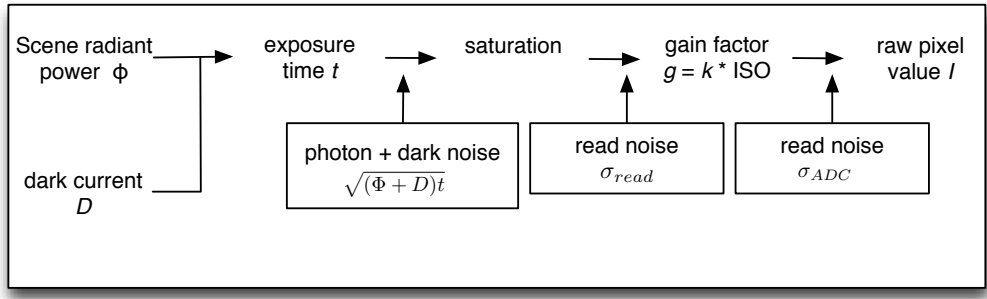


Fig. 2.8. – Linear image formation pipeline and noise modeling

Linear image formation:

$$I = \min((\Phi + D)t \cdot g + I_0 + n, I_{max}) \quad (2.9)$$

Where I_0 is the black offset. n is the noise. I_{max} is the saturation level. Other variables are shown in Fig. 2.8.

The sensor noise model is shown in Eq. 2.10:

$$Var(n) = (\Phi + D)t \cdot g^2 + \sigma_{read}^2 \cdot g^2 + \sigma_{ADC}^2 \quad (2.10)$$

Photon shot noise is the dominant noise in bright pixels. In dark pixels, read and ADC noise are dominant. In high ISO settings, the pre-gain noise, photon noise and read noise have the most influence. The dark noise, which is thermal dependent, is the dominant noise for long exposures.

2.4.2 Color Noise Propagation

As described in [Burns and Berns, 1997], the noise in RGB channels is independent with each other. Therefore, the off-diagonal elements in the covariance matrix Σ_0 equal to zero. However, the transformation from camera signals to XYZ and from XYZ to $L^*a^*b^*$ introduce off-diagonal terms and lead to color noise. This is shown below for an RGB camera.

RGB is converted to XYZ :

$$XYZ = M * RGB \quad (2.11)$$

where M is:

$$M = \begin{pmatrix} m_{11} & m_{12} & m_{13} \\ m_{21} & m_{22} & m_{23} \\ m_{31} & m_{32} & m_{33} \end{pmatrix} \quad (2.12)$$

Next, XYZ is converted to $L^*a^*b^*$:

$$L^* = 116f\left(\frac{Y}{Y_n}\right) - 16 \quad (2.13)$$

$$a^* = 500 \left[f\left(\frac{X}{X_n}\right) - f\left(\frac{Y}{Y_n}\right) \right] \quad (2.14)$$

$$b^* = 200 \left[f\left(\frac{Y}{Y_n}\right) - f\left(\frac{Z}{Z_n}\right) \right] \quad (2.15)$$

where

$$f(t) = \begin{cases} t^{1/3} & \text{if } t > (\frac{6}{29})^3 \\ \frac{1}{3} \left(\frac{29}{6}\right)^2 t + \frac{4}{29} & \text{otherwise} \end{cases} \quad (2.16)$$

The covariance matrix Σ_2 is:

$$\Sigma_2 = JM\Sigma_0M^TJ^T \quad (2.17)$$

then the diagonal elements of Σ_2 are

$$\Sigma_2(1, 1) = \left(\frac{\partial L^*}{\partial Y}\right)^2 (m_{21}^2 + m_{22}^2 + m_{23}^2) \quad (2.18)$$

$$\begin{aligned}\Sigma_2(2, 2) = & \left(\frac{\partial a^*}{\partial X}\right)^2 (m_{11}^2 + m_{12}^2 + m_{13}^2) \\ & + 2 \frac{\partial a^*}{\partial X} \frac{\partial a^*}{\partial Y} (m_{11}m_{21} + m_{12}m_{22} + m_{13}m_{23}) \\ & + \left(\frac{\partial a^*}{\partial Y}\right)^2 (m_{21}^2 + m_{22}^2 + m_{23}^2)\end{aligned}\quad (2.19)$$

$$\begin{aligned}\Sigma_2(3, 3) = & \left(\frac{\partial b^*}{\partial Y}\right)^2 (m_{21}^2 + m_{22}^2 + m_{23}^2) \\ & + 2 \frac{\partial b^*}{\partial X} \frac{\partial b^*}{\partial Z} (m_{21}m_{31} + m_{22}m_{32} + m_{23}m_{33}) \\ & + \left(\frac{\partial b^*}{\partial Z}\right)^2 (m_{31}^2 + m_{32}^2 + m_{33}^2)\end{aligned}\quad (2.20)$$

If the object is gray and the light source is illuminant E, $X = Y = Z, X_n = Y_n = Z_n$. Then $\frac{X^{-\frac{2}{3}}}{X_n^{\frac{1}{3}}}, \frac{Y^{-\frac{2}{3}}}{Y_n^{\frac{1}{3}}}$ and $\frac{Z^{-\frac{2}{3}}}{Z_n^{\frac{1}{3}}}$ have the same value, notated by variable A. The diagonal elements in Σ_2 is $(\Delta L^*)^2, (\Delta a^*)^2, (\Delta b^*)^2$, then Eqs. 2.18- 2.20 can be approximated as

$$(\Delta L^*)^2 \simeq \left(\frac{116A}{3}\right)^2 (m_{21}^2 + m_{22}^2 + m_{23}^2) \quad (2.21)$$

$$(\Delta a^*)^2 \simeq \left(\frac{500A}{3}\right)^2 [(m_{11} - m_{21})^2 + (m_{12} - m_{22})^2 + (m_{13} - m_{23})^2] \quad (2.22)$$

$$(\Delta b^*)^2 \simeq \left(\frac{200A}{3}\right)^2 [(m_{21} - m_{31})^2 + (m_{22} - m_{32})^2 + (m_{23} - m_{33})^2] \quad (2.23)$$

Noise can be approximated as

$$\text{noise} = \sqrt{\Delta L^{*2} + \Delta a^{*2} + \Delta b^{*2}} \quad (2.24)$$

Thus, the color transformation matrix impacts the color noise propagation in the course of the color transformation by enlarging the $(\Delta L^*)^2, (\Delta a^*)^2, (\Delta b^*)^2$ to different degrees. Thus, multispectral systems producing the same colorimetric accuracy can have dissimilar color noise depending on its spectral sensitivities. For example, Kuniba demonstrated that a CMY camera resulted in much greater color noise than an RGB camera although the CMY camera had lower intrinsic noise [Kuniba and Berns, 2009]. This type of noise is an important factor when designing filters for multispectral imaging.

Modeling and Optimizing Spectral Sensitivity Considering Noise Propagation

This chapter will describe a computational simulation method by modeling both RGB- and CMY-type filter sets, and assessing the color reproduction and noise due to a color transformation. The trade-off between color reproduction and noise will be described. Optimization will be performed to determine the spectral sensitivities that yield the smallest ΔE_{00} , the lowest noise, or a compromise of the two goals. A seven-channel bandpass filter set was modeled and optimized to yield high spectral and colorimetric reproduction accuracy as well as low noise. The objective is to provide insights as to the influence of design choices, such as signal encoding and filter selection.

3.1 Spectral Sensitivity Modeling

The spectral sensitivity model should meet physical restrictions. The transmittance should be larger than zero and not exceed unity. The shape of the spectral transmittance should be smooth. A model in [Kuniba and Berns, 2009] is applied here. Example plots are shown in Fig. 3.1.

The spectral sensitivity curves of RGB-type sensors are defined with Gaussian functions:

$$S_i(\lambda) = e^{-\frac{(\lambda - \lambda_i)^2}{w_i^2}} \quad (3.1)$$

where λ is wavelength, λ_i is peak wavelength, and w_i is the half bandwidth. $i = R, G, B$. Similarly, the CMY sensors are also described by Gaussian functions:

$$C(\lambda) = \begin{cases} 0 & \text{if } \lambda > \lambda_c \\ 1 - e^{-\frac{(\lambda-\lambda_c)^2}{w_c^2}} & \text{if } \lambda \leq \lambda_c \end{cases} \quad (3.2)$$

$$M(\lambda) = 1 - e^{-\frac{(\lambda-\lambda_M)^2}{w_M^2}} \quad (3.3)$$

$$Y(\lambda) = \begin{cases} 1 - e^{-\frac{(\lambda-\lambda_Y)^2}{w_Y^2}} & \text{if } \lambda \leq \lambda_Y \\ 0 & \text{if } \lambda > \lambda_Y \end{cases} \quad (3.4)$$

3.2 Trichromatic Spectral Sensitivity Optimization Modeling

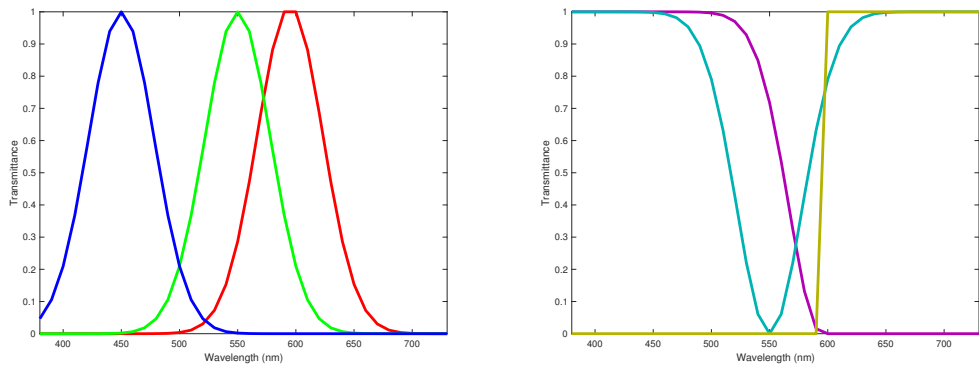


Fig. 3.1. – Left: RGB-type sensor with peak wavelength of 595nm, 550nm, 450nm and half bandwidth of 40nm for all; Right: CMY-type sensor with peak wavelength 595nm, 550nm, 450nm and half bandwidth of 40nm for all.

3.2.1 Color Space Transformation Modeling

The color transformation matrix \mathbf{M} is defined as

$$\mathbf{M} = \begin{pmatrix} m_1 & m_2 & m_3 \\ m_4 & m_5 & m_6 \\ m_7 & m_8 & m_9 \end{pmatrix} \quad (3.5)$$

where

$$\begin{pmatrix} X/X_n \\ Y/Y_n \\ Z/Z_n \end{pmatrix} = \mathbf{M} \times \begin{pmatrix} C_1/C_{1,n} \\ C_2/C_{2,n} \\ C_3/C_{3,n} \end{pmatrix} \quad (3.6)$$

and

$$m_1 + m_2 + m_3 = m_4 + m_5 + m_6 = m_7 + m_8 + m_9 = 1 \quad (3.7)$$

m_1 to m_9 are the coefficients in the color transformation matrix. X_n, Y_n, Z_n are the tristimulus value of white. When the input is neutral, the output is neutral. The corresponding constraints are shown in Eq. 3.7, which enable the neutral camera signal to be mapped to the colorimetric neutral output. The C_1 to C_3 are the camera signal of either RGB- or CMY-type respectively:

$$C_i = \int_{\lambda_1}^{\lambda_2} S_{i,\lambda} \times L_\lambda \times R_\lambda \quad (3.8)$$

where $S_{i,\lambda}$ corresponds to the sensor spectral sensitivity, L_λ is the spectral radiance of the light source, and R_λ is the spectral reflectance of a sample.

3.2.2 Optimization Procedure

D50 was used as the illuminant along with the 1931 standard observer. The Xrite ColorChecker SG (CCSG) was used as the training data set to optimize

the color transformation matrix. The Artist Paint Target (APT) was used as the validation data set.

The effects of the peak wavelength and the bandwidth of the RGB filter sets on color accuracy and noise were studied in [Kuniba and Berns, 2009]. A cost function:

$$(\overline{\Delta E_{94}^*}^2 + \alpha \bar{\sigma}^2)^{1/2} \quad (3.9)$$

was used to find the optimal filter set for different α s, where α is a weighting number, $\bar{\sigma}^2$ is the propagated color noise (Eq. 3.11). It was demonstrated that when α changes in the optimal filter set, the peak wavelength of the red filter changes immensely, while that of the green and blue filters almost stay the same. In other words, the effect of the red filter is dominant over the effects of the other two filters in terms of the trade-off between color accuracy and noise. Therefore, in this thesis, only the spectral sensitivity of the red filter was studied.

The color transformation matrix was optimized non-linearly to minimize Q (fminunc in MATLAB, trust-region algorithm), which is defined as:

$$Q = \alpha \times 100 \times RMS + \beta \overline{\Delta E_{00}} + (1 - \alpha - \beta) \bar{\sigma} \quad (3.10)$$

where α and β are weighting parameters. An equal weighting ($\alpha = \beta = 0.3$) was chosen for the optimization. In different applications, different weighting factors could be used and would lead to different results. RMS is the root-mean-square error between the calculated and measured spectral reflectance. σ is the propagated color noise for neutral patches from the color transformation matrix:

$$\sigma = (\Delta L^*{}^2 + \Delta a^*{}^2 + \Delta b^*{}^2)^{1/2} \quad (3.11)$$

and ΔL^* , Δa^* and Δb^* are calculated in eq. 2.13 to eq. 2.15. The matrix used to calculate σ is:

$$\mathbf{M} = (XYZ)_{cal} * C^\dagger \quad (3.12)$$

where $(XYZ)_{cal}$ is the XYZ calculated from the predicted spectral reflectances; while the spectral reflectances are predicted as the product of the camera signal and the updated \mathbf{M}_0 during the optimization.

The result of the pseudo-inverse matrix \mathbf{M}_0 was used as the starting value:

$$\mathbf{M}_0 = R_{\lambda,i} * C_{i,n}^\dagger \quad (3.13)$$

where $R_{\lambda,i}$ is the spectral reflectance of the i th patch; $C_{i,n}$ is the camera signal of the i th patch of CCSG. For RGB and CMY type of camera, $n = 3$.

CCSG data were used as the training set. The APT data were used as the validation set.

The workflow of the optimization is shown in Fig. 3.2.

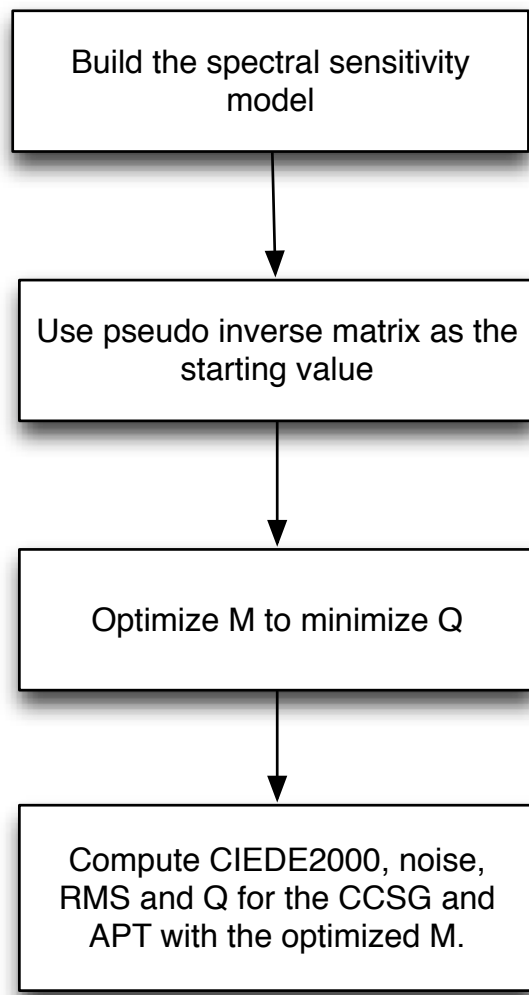


Fig. 3.2. – A workflow of the trichromatic sensor modeling and optimization.

3.2.3 Results and Discussions

RGB Filter Set

It is shown in Fig. 3.3 that the root-mean-square error decreases when red filter peak wavelength becomes longer, which can be explained by the wider range of the spectral transmittance of the filter set. The range of RMS is 0.035-0.06.

For peak wavelength > 605nm, ΔE_{00} increases when peak wavelength becomes longer (Fig.3.4), which can be explained by the decreasing similarity between the red channel spectral sensitivity and long-wavelength lobe of the \bar{x} color matching function. The range of ΔE_{00} is 1.0-4.5. For peak wavelengths greater than 605nm, in general, noise decreases when the peak wavelength becomes longer (Fig.3.5), which is in line with the result in [Kuniba and Berns, 2009]. Thus, there is a trade-off between the noise and color accuracy. Since the bandwidths of the sensitivity curve were the same for all the cases, the increase of noise for short peak wavelengths cannot be explained by the collection of more photons. This result can be explained in terms of noise propagation. The noise amplification at the color transformation step becomes larger due to the increasing overlaps of the spectral transmission curves between red and green filters when the peak red moves towards shorter wavelengths.

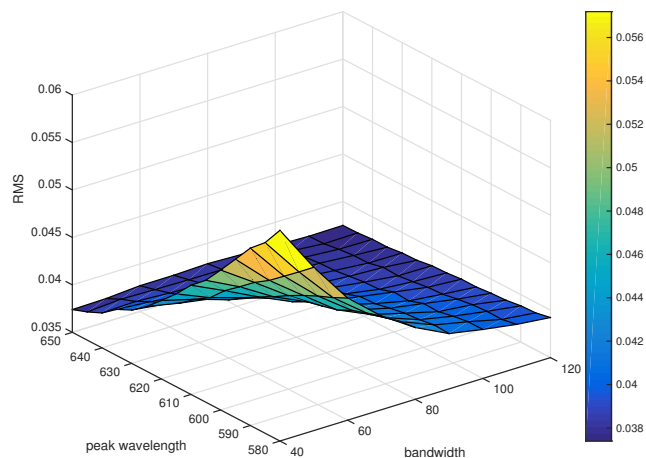


Fig. 3.3. – RMS derived from the red filters with various peak wavelengths and bandwidths.

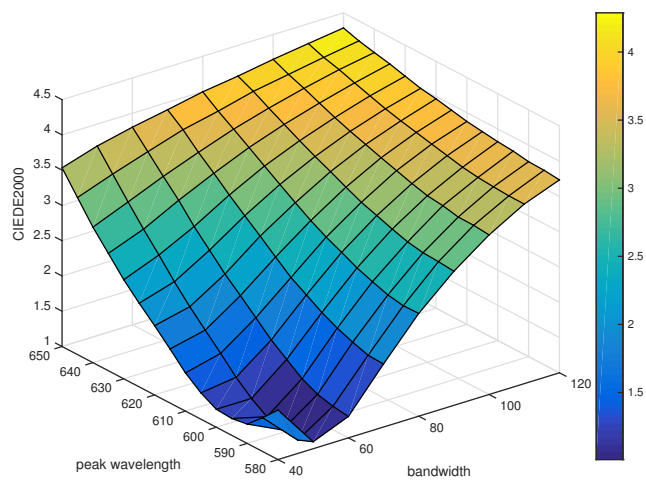


Fig. 3.4. – ΔE_{00} derived from the red filters with various peak wavelengths and bandwidths.

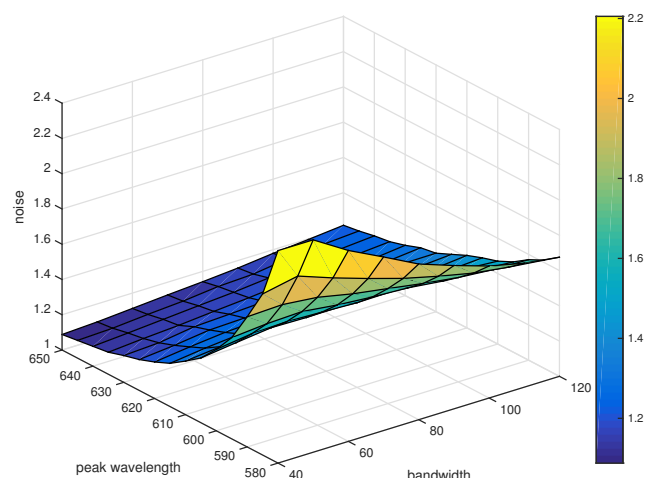


Fig. 3.5. – Noise σ derived from the red filters with various peak wavelengths and bandwidths.

CMY Filter Set

The CMY filter set was assessed using the same method as that of the RGB filter set described above. The cyan filter was chosen for the same reason as why the red filter was chosen in the RGB filter set. The results for $\alpha = 0.3$, $\beta = 0.3$ are shown in Fig. 3.6, 3.7 and 3.8. The noise amplitude is much larger than that of the RGB filters. It can be explained by the noise amplification at the color transformation step due to the larger overlaps of the spectral transmission curves between the CMY filters. The ΔE_{00} amplitude is also larger than that of the RGB filters, which could be explained by the dissimilarity between the spectral sensitivity shapes of the CMY and color matching functions. Again, [Kuniba and Berns, 2008] found similar results, verifying the method of optimization used in this thesis.

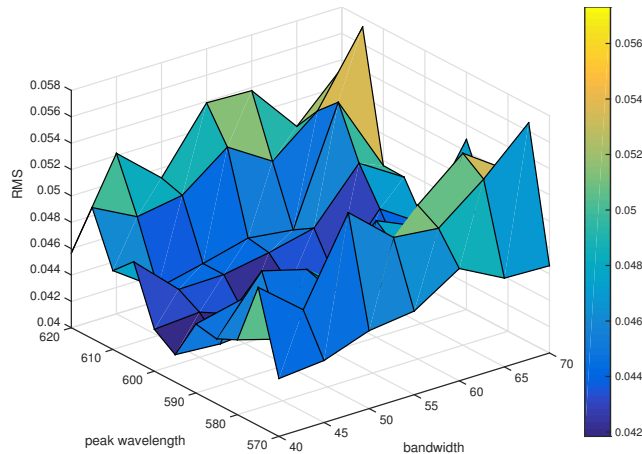


Fig. 3.6. – RMS derived from the cyan filters with different peak wavelength and bandwidth.

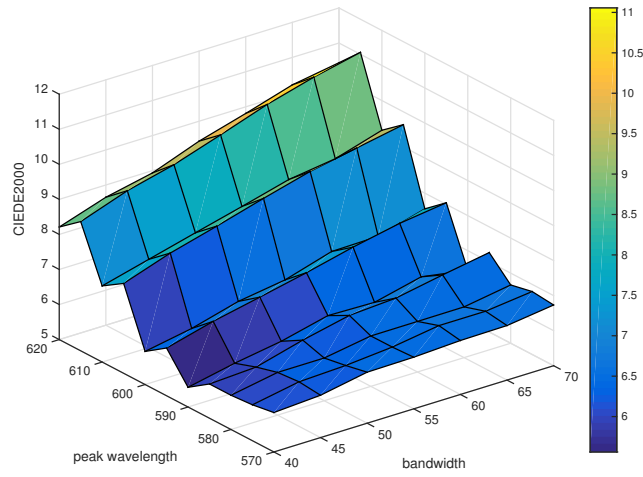


Fig. 3.7. – $\overline{\Delta E_{00}}$ derived from the cyan filters with different peak wavelength and bandwidth.

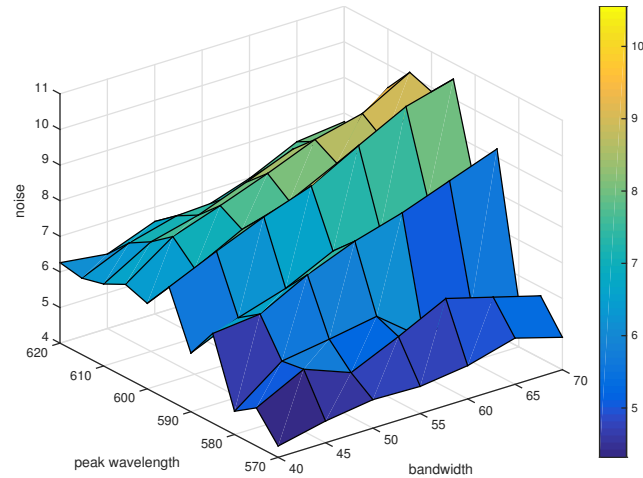


Fig. 3.8. – Noise σ derived from the cyan filters with different peak wavelength and bandwidth.

3.3 Filter Optimization for a Seven-Channel Multispectral Camera

Theoretical Gaussian Filters

The optimal set of seven bandpass filters for D50 illumination and a monochrome camera manufactured by Finger Lakes Instrumentation Company was calculated using a similar method. The monochrome camera will be used to build the spectral imaging system in the following chapters.

A matrix including the peak wavelengths $\lambda = 400, 450, 500, 550, 600, 650, 700\text{nm}$ with identical half bandwidths $w = 60\text{nm}$ was used as the starting value to minimize Q, defined in Eq. 3.14.

$$Q = \alpha(100\overline{RMS}) + \beta\overline{\Delta E_{00}} + (1 - \alpha - \beta)\bar{\sigma} \quad (3.14)$$

where RMS is the root-mean-square error of the spectral reflectance difference between the measured data and predicted data, and it is scaled by 100 to agree with the order of magnitude of ΔE_{00} and σ . α and β are the weighting factors of the RMS and the ΔE_{00} . An equal weighting ($\alpha = \beta = 0.3$) was chosen for the optimization. In different applications, different weighting factors could be used and may lead to different results. For example, the weighting of the RMSE could be raised if the goal is to achieve high spectral reproduction accuracy. The work flow is shown in Fig. 3.9. The result is shown in Fig. 3.10. The corresponding data are shown in Table. 3.1.

The color transformation matrix is shown in Table 3.2. The second, fourth and fifth channel (with peak wavelengths of 449nm, 551nm and 596nm) have a higher contribution to tristimulus value Z, Y and X, in line with color matching functions.

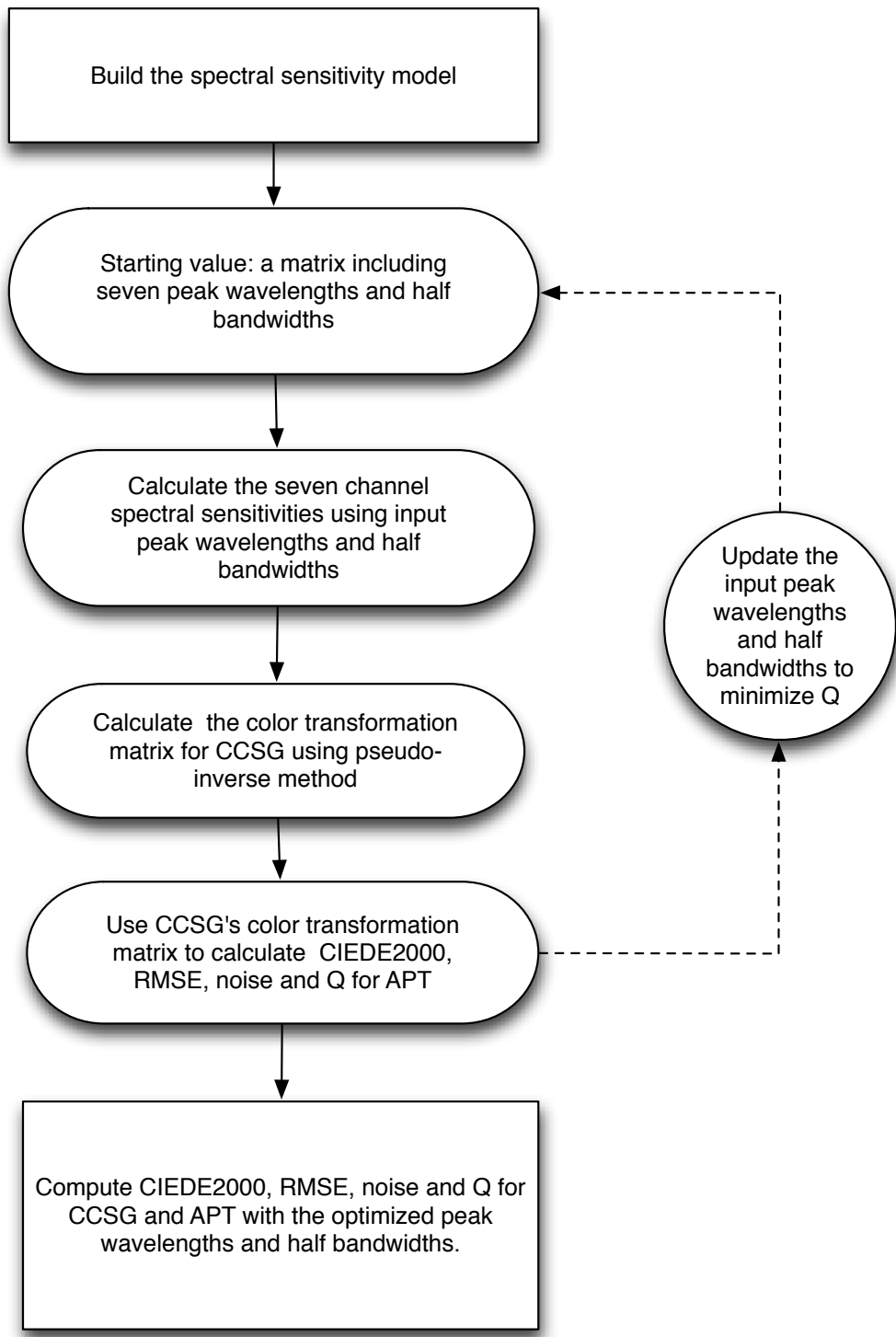


Fig. 3.9. – A workflow of the optimization of seven channel bandpass filter set modeling.

The approximated color matching functions(Fig. 3.11) are the product of the seven filter spectral sensitivities and their corresponding optimal color transformation matrix. The color matching functions were well approximated by the seven filter sensitivities. μ -factor [Vora and Trussell, 1993] is a colorimetric performance metric with respect to the mean-square error between a set of color matching functions and its estimation, expressed as:

$$\mu = \text{Trace}(S' A^\dagger * A' * S^\dagger)/3 \quad (3.15)$$

where S is the product of estimated color matching function and the viewing illuminant radiance, A is the product of standard color matching function and imaging illuminant radiance[Vora and Trussell, 1993]. For the optimized seven filter set, $\mu = 0.983$, which represents a highly accurate color matching function estimation.

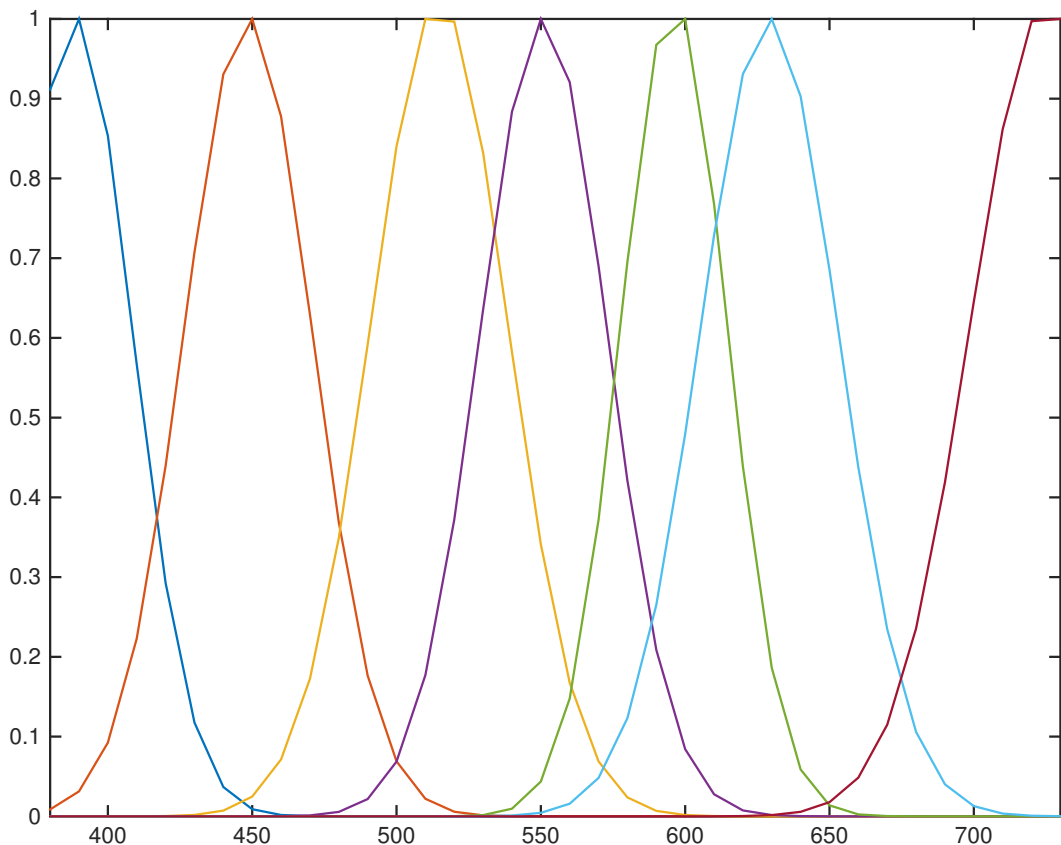


Fig. 3.10. – Optimal seven bandpass filters.

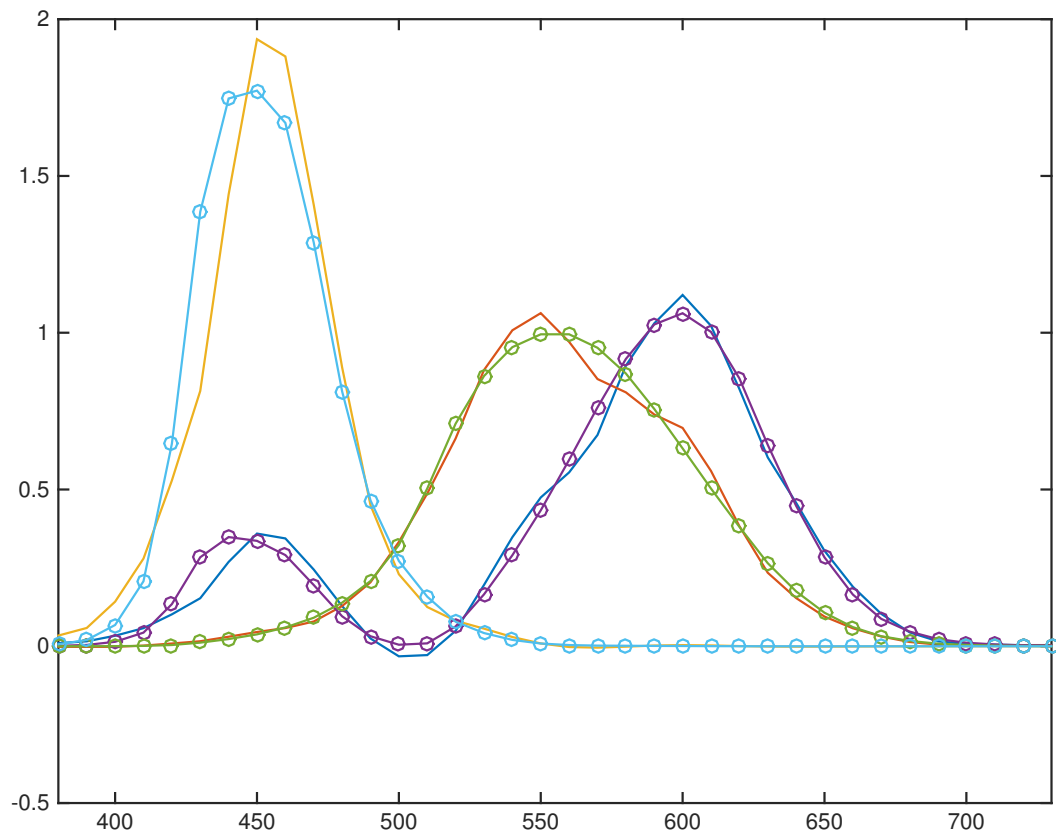


Fig. 3.11. – Lines: estimated color matching function using the optimal seven bandpass filters. Circle marked lines: standard color matching function.

Tab. 3.1. – Optimal seven filter spectral sensitivity for $\alpha = 0.3$, $\beta = 0.3$.

peak wavelength (nm)	389	449	515	551	596	629	725
half-bandwidth (nm)	28	31	34	31	26	34	37

Tab. 3.2. – Color transformation matrix for the optimal seven filter spectral sensitivity for $\alpha = 0.3$, $\beta = 0.3$.

0.308	1.931	-0.576	1.892	6.23	1.033	-0.139
0.349	-0.893	3.167	6.891	0.537	0.781	-0.156
0.91	10.9	-1.471	0.911	-0.651	0.208	-0.056

3.4 Conclusions

The spectral sensitivities of RGB and CMY filter sets were modeled by Gaussian functions and optimized with the considerations of RMSE, color accuracy, and noise. It was shown that the ΔE_{00} of the RGB filter set is convergent, i.e., for all bandwidths, when the peak wavelength increases, the ΔE_{00} decreases first, achieves its minimum and then increases. For longer peak wavelengths, there is a trade-off between color accuracy and noise. Longer peak wavelengths generate less noise but larger ΔE_{00} . The propagated noise of the CMY filter set is much higher than that of the RGB filter set, which can be explained by the noise amplification at the color transformation step due to the large overlaps between the spectral transmission curves of the CMY filters.

The techniques and results were expanded compared to [Kuniba and Berns, 2009] in these aspects: Firstly, the propagated noise of neutral patches was used in the cost function. In [Kuniba and Berns, 2009], the propagated noise of all patches in the targets was used in the cost function. The two results agree with each other very well in terms of the trade-off between color accuracy and noise. Secondly, a trend of how color difference and noise changes among all combinations of peak wavelengths and bandwidths was explored in this thesis. However, only the optimal combination of peak wavelengths and bandwidths was shown in [Kuniba and Berns, 2009]. Lastly, the inclusion of spectral estimation in the optimization cost function yielded lower noise than the result in [Kuniba and Berns, 2009].

A seven bandpass filter set was modeled and optimized using the same technique. The inclusion of the metric RMSE in the cost function ensured accurate spectral reconstruction. The optimal Gaussian filter set had higher colorimetric reproduction accuracy than the interference filter set analyzed in the previous chapter.

Schott "Sandwich Filter"

Selection

Schott filters can be glued together to produce bandpass shapes, which can be used to build the multispectral camera. A glued pair of Schott filters will be called a "sandwich filter" as an abbreviation in the following discussions. Two methods were tested to find the optimal set of sandwich filters. For the first method, sandwich filters were selected having the most similar spectral transmittance as the theoretical Gaussian filters derived in the previous chapter. For the second method, sandwich filters whose peak wavelengths were equally spaced across the spectrum of interest were tested as candidate filters and selected according to their spectral and colorimetric reproduction accuracy.

4.1 Theory

The spectral transmittance $T_{combination,\lambda}$ of the combination of two candidate filters ($T_{1,\lambda}, T_{2,\lambda}$) was calculated using the following equation:

$$T_{combination,\lambda} = T_{1,\lambda} \cdot T_{2,\lambda} / \max(T_{1,\lambda} \cdot T_{2,\lambda}) \quad (4.1)$$

The normalization is equivalent to setting optimal camera exposure. Eq.4.2 was used to calculate filter spectral transmittance from filters with different thickness and known spectral transmittance inside a filter.

$$T_{2,\lambda} = T_{1,\lambda}^{l_2/l_1} \quad (4.2)$$

where T_λ is the spectral transmittance inside a filter. l is filter thickness. This equation can be derived from Bougeur's (Lambert's) Law [Swinehart, 1962]:

$$\epsilon cl = A = \log_{10}\left(\frac{1}{T}\right) \quad (4.3)$$

where A is absorbance, which is proportional to concentration c and thickness l ; ϵ is molar absorptivity or molar extinction coefficient and is a measure of the probability of the electronic transition. The spectral transmittance $T_{2,\lambda}$ of the filter whose thickness is l_2 can be calculated using the known transmittance and thickness of another filter which has the same concentration c using Lambert's Law:

$$T_{2,\lambda} = T_{1,\lambda} 10^{\epsilon c(l_1 - l_2)} \quad (4.4)$$

where ϵ and c can be replaced using Eq.4.5 to get Eq. 4.2.

$$\epsilon c = \frac{\log_{10}\left(\frac{1}{T_{1,\lambda}}\right)}{l_1} \quad (4.5)$$

Eq. 4.1-4.5 require internal transmittance. The assumption is that the difference between the internal and external transmittance is not significant. These data were provided by Schott. Although compensating for refractive index discontinuity will change transmittance slightly, this effect was considered negligible for filter selection and was ignored.

4.2 Fitting Gaussians

Two candidate FLI filter wheels with different filter sizes were used in this thesis. Both had the limitation of a maximum of 6mm thickness of the filter. Thus, the sandwich filters were selected to meet this requirement. 3mm+2mm and 3mm+3mm were tested. The selection was based on the available Schott filter spectral database and also those sold by the Andover

Corporation (<https://www.andovercorp.com/products/colored-glass/general-specifications/>).

Since the optimized spectral sensitivities of the filters have Gaussian shapes, the width and peak wavelength position of the candidate filters should be located within a limited continuous solid. Therefore, the Schott filters were pre-selected. Filters whose spectral transmittance shape were smooth and with single or double peaks locating between 400nm-700nm were selected. The number of candidate filters was reduced from 64 to 52 for the Schott database, and 41 to 33 for the Andover database.

The root-mean-square error between each sandwich filter and each theoretical Gaussian filter was calculated. The optimal sandwich filters should have similar shapes as the theoretical Gaussian filters, and the optical throughputs should be high. Therefore, the filter combinations whose RMSE is the smallest and peak spectral transmittance larger than 0.3 (or any other reasonable minimum peak to meet the application requirements) were selected as candidate filters.

For the Schott database, the seven filters most similar to theoretical Gaussian filters were selected. The camera signals calculated using Eq. 2.3, and the transmittance was optimized as described previously.

The RMSE, ΔE_{00} , noise, and Q values for the APT target are shown in Table 4.1. Same method was used to calculate the results of the interference filters. The results of the interference filter are shown in the first row in the table for comparison. Then, the results from the theoretical Gaussian filters are shown.

For the seven filters selected from the Schott database, the results are shown in the table as “Schott A”. The transmittances of the selected filters and the system spectral sensitivity are shown in Fig. 4.1. However, the first filter (1# as an abbreviation) had a peak at long wavelengths. 2# did not fit the 2#

Gaussian filter well. The spectral transmittance of 7# should be reduced since the sensor was highly sensitive.

An interference filter whose peak wavelength is 450nm was used to replace the 2# of Schott A set since 2# of Schott A didn't fit the 2# Gaussian filter well. Results are shown in Table 4.1 as "Schott B" and Fig. 4.2. The 2# still did not fit well and the ΔE_{00} was higher than the previous selection.

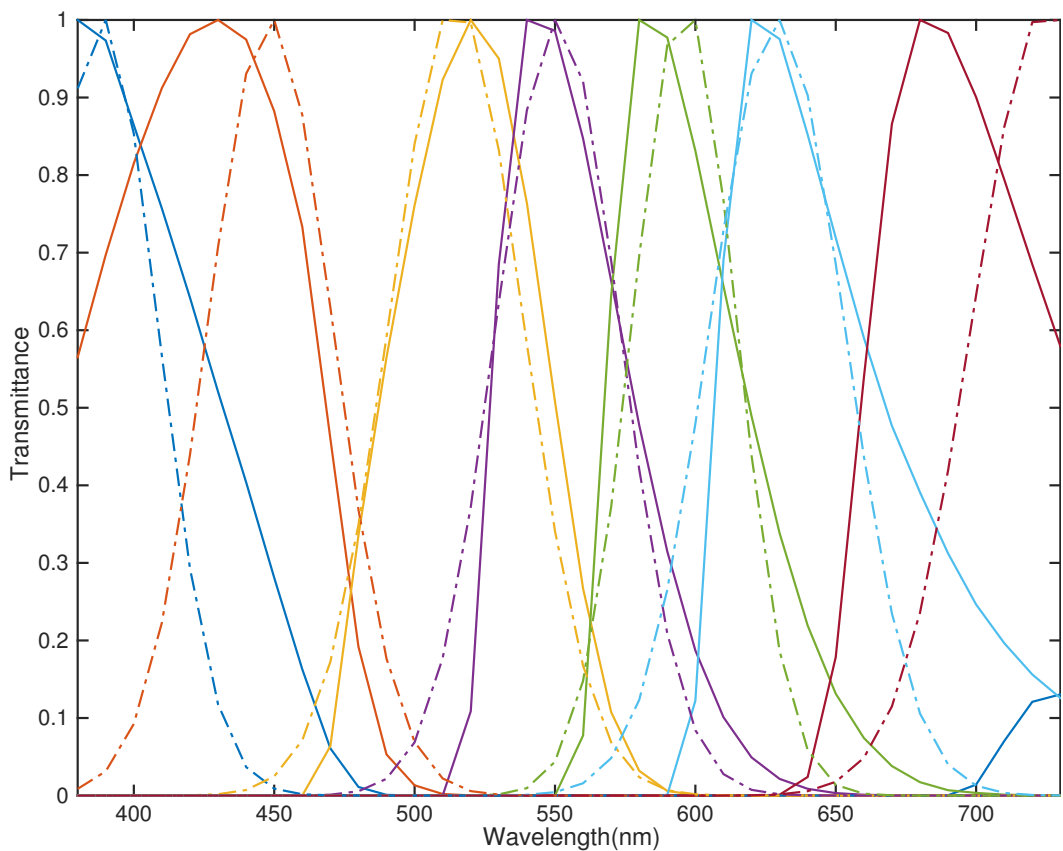
Schott KG 5 filter was used to replace one of the 7# filters because of its lower near-IR spectral transmittance. Results are shown in Table 4.1 as "Schott C" and Fig. 4.3.

The same method was used to select filters from the Andover database. The results are shown in Table 4.1 as "Andover A" and in Fig. 4.4.

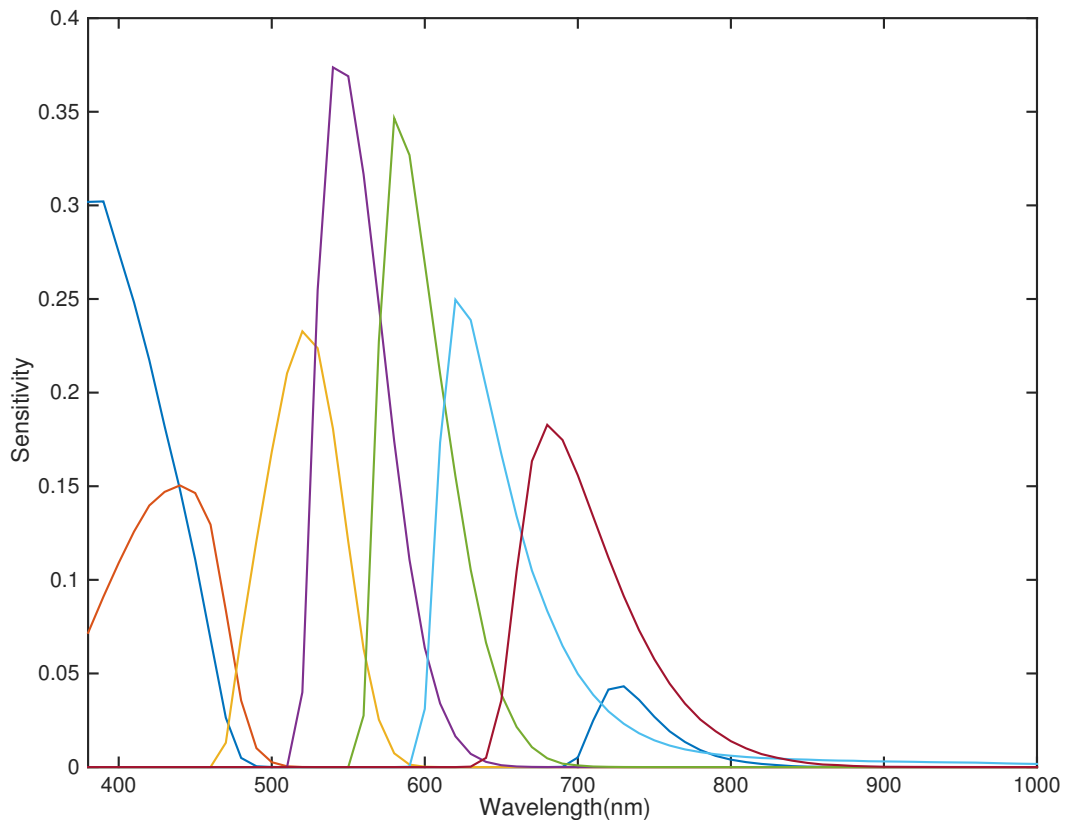
KG5 was used to replace one of the 7# filters. The results are shown in Table 4.1 as "Andover B" and Fig. 4.5.

The same method was used to calculate Gaussian filters (Table 4.1 "theoretical Gaussian filters with UVIR") for the FLI with UV/IR cut filters first, and select filters to fit the Gaussian filters from the Schott (Table 4.1 "Schott D", "Schott E" (7# was replaced by KG5 and RG655)) and Andover database (Table 4.1 "Andover C"). Filters with 2mm and 3mm thickness were selected using the same method and the results are shown in Table 4.1 "5mm Schott".

Comparing the ΔE_{00} , RMSE, noise, and Q results, as well as considering the near IR throughputs, the set named "Andover B" was selected as the final sandwich filter set. The throughput of the fourth channel (the channel which is closest to V_λ) is the highest, important for perceived image quality. The estimated spectral and colorimetric reproduction are shown in Fig. 4.6 and 4.7. The filter names of "Andover B" are shown in Table 4.2. The spectral transmittances are shown in Fig. 4.8.

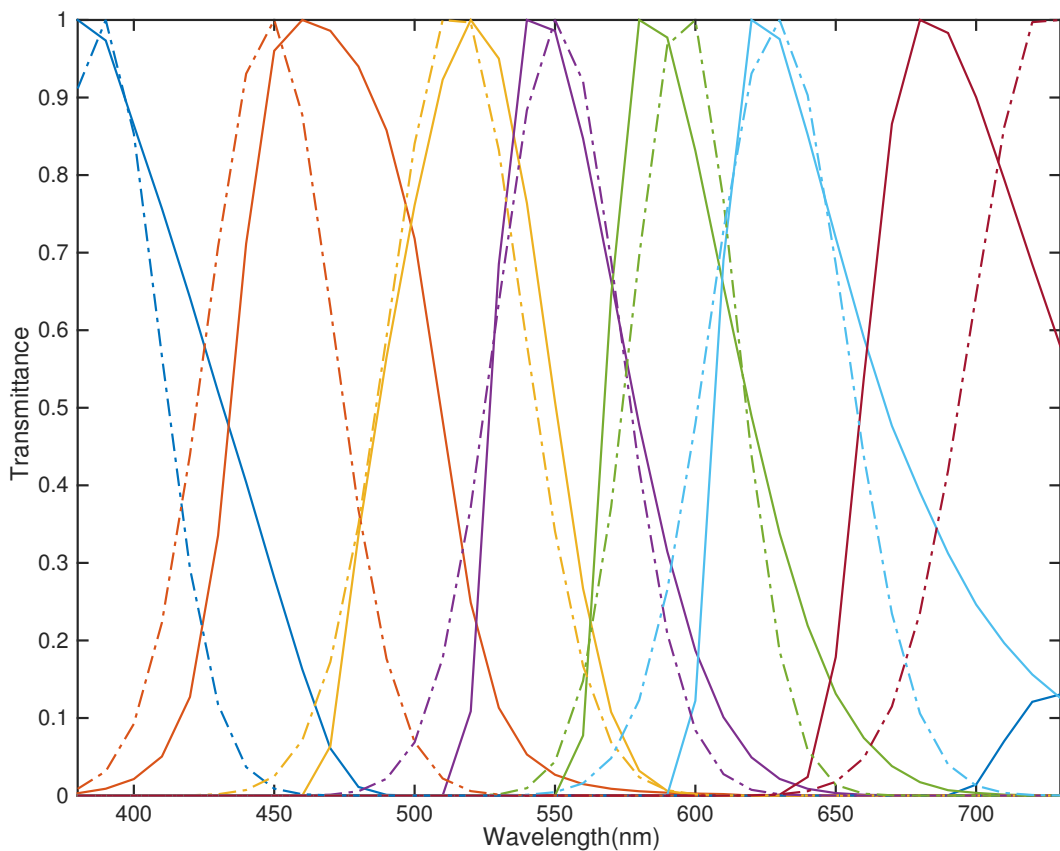


(a) Normalized spectral transmittance. Dash lines: theoretical Gaussian filters. Solid lines: selected sandwich filters.

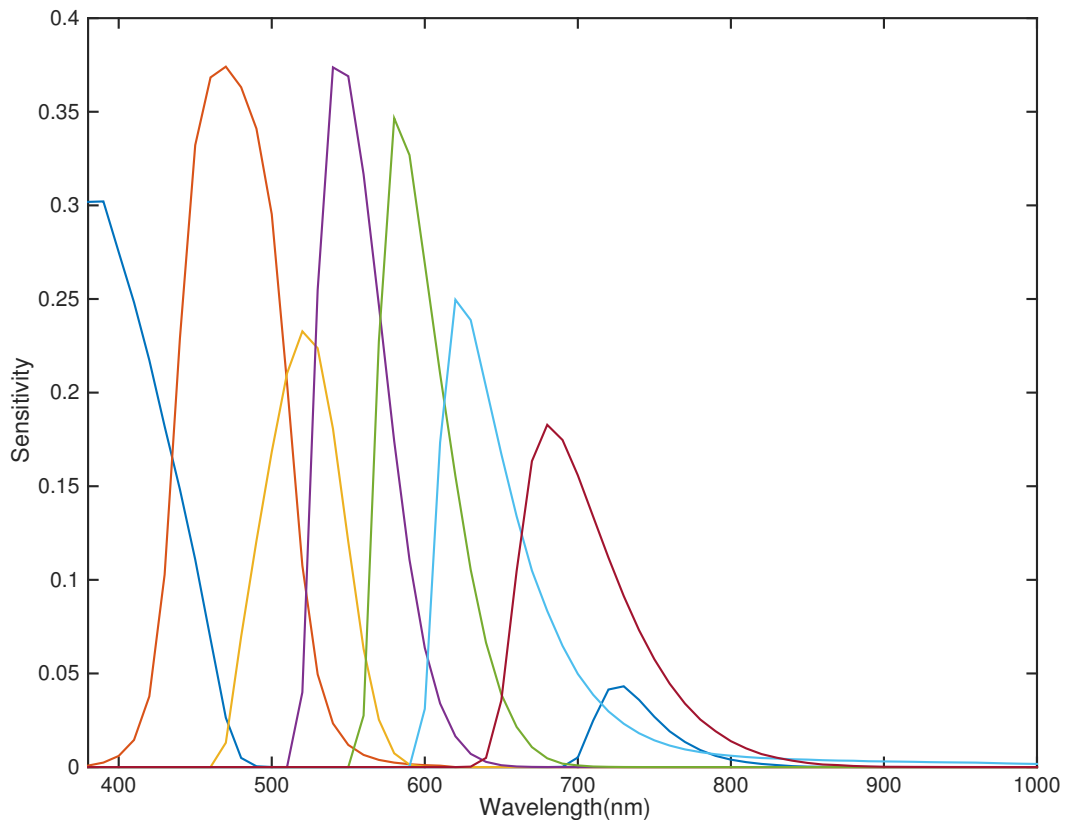


(b) Spectral sensitivity of the whole system including the FLI sensor and filters.

Fig. 4.1. – Filters selected from Schott database.

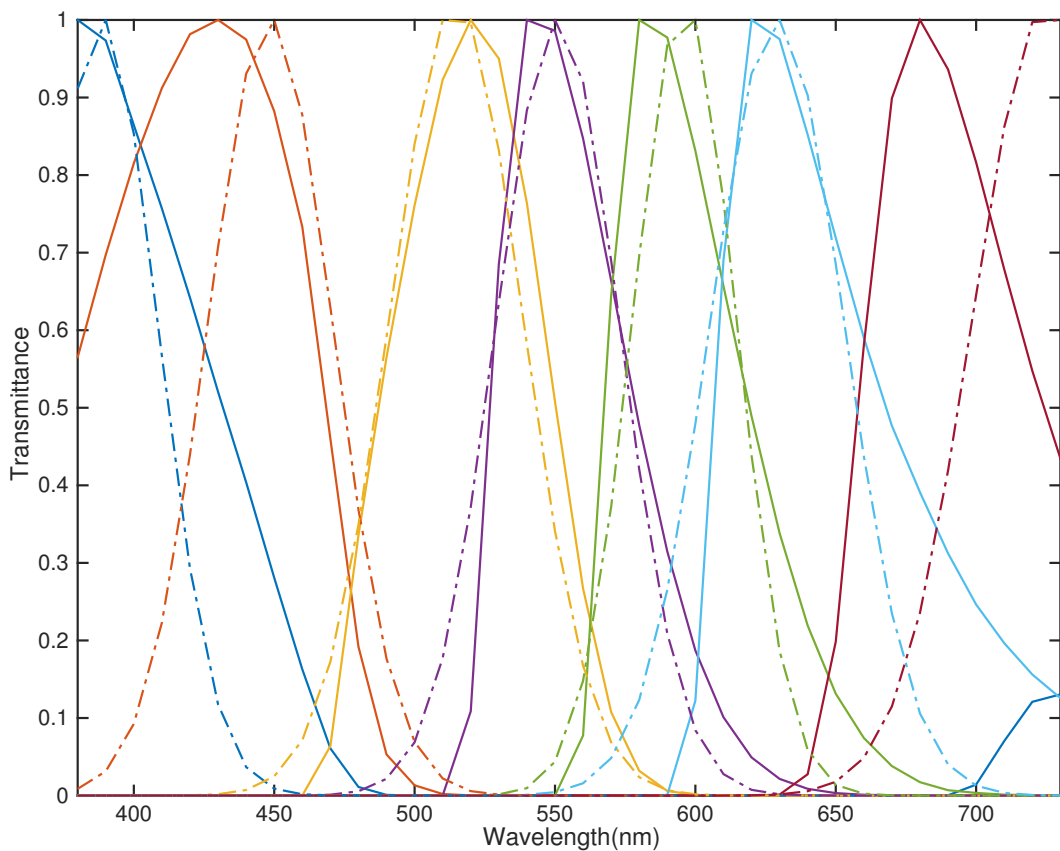


(a) Normalized spectral transmittance. Dash lines: theoretical Gaussian filters. Solid lines: selected sandwich filters.

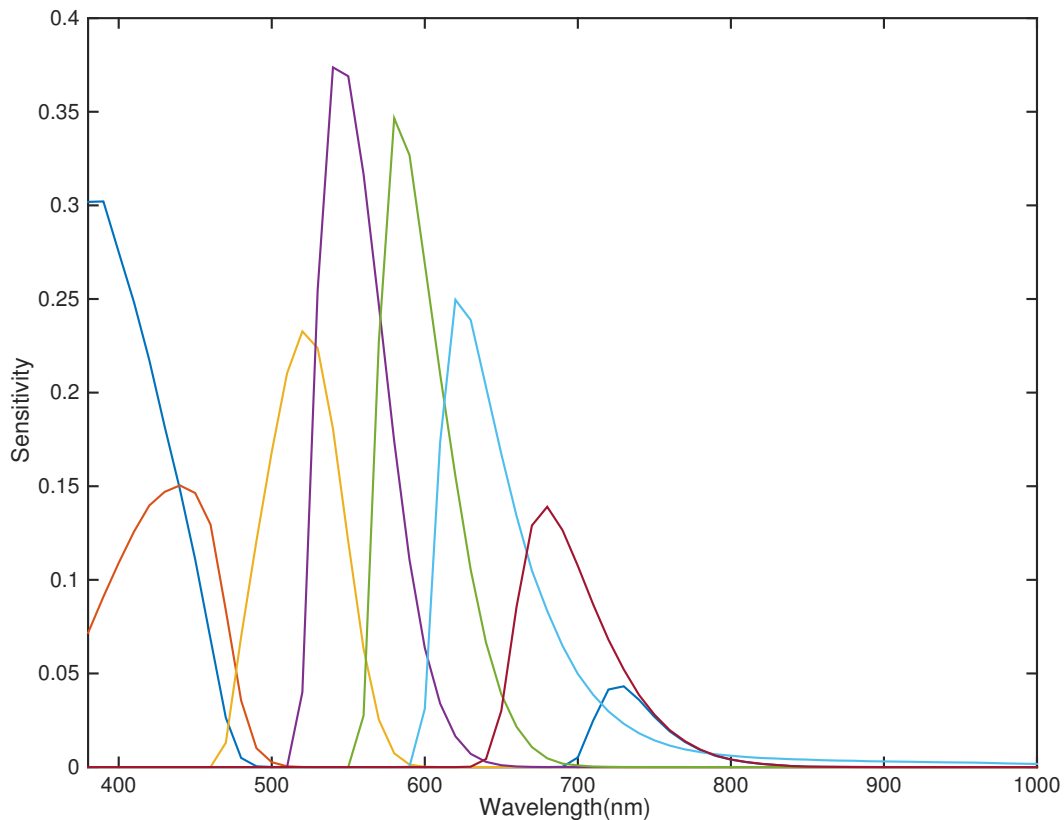


(b) Spectral sensitivity of the whole system including the FLI sensor and filters.

Fig. 4.2. – Filters selected from Schott database. The second sandwich filter was replaced by 450nm interference filter.

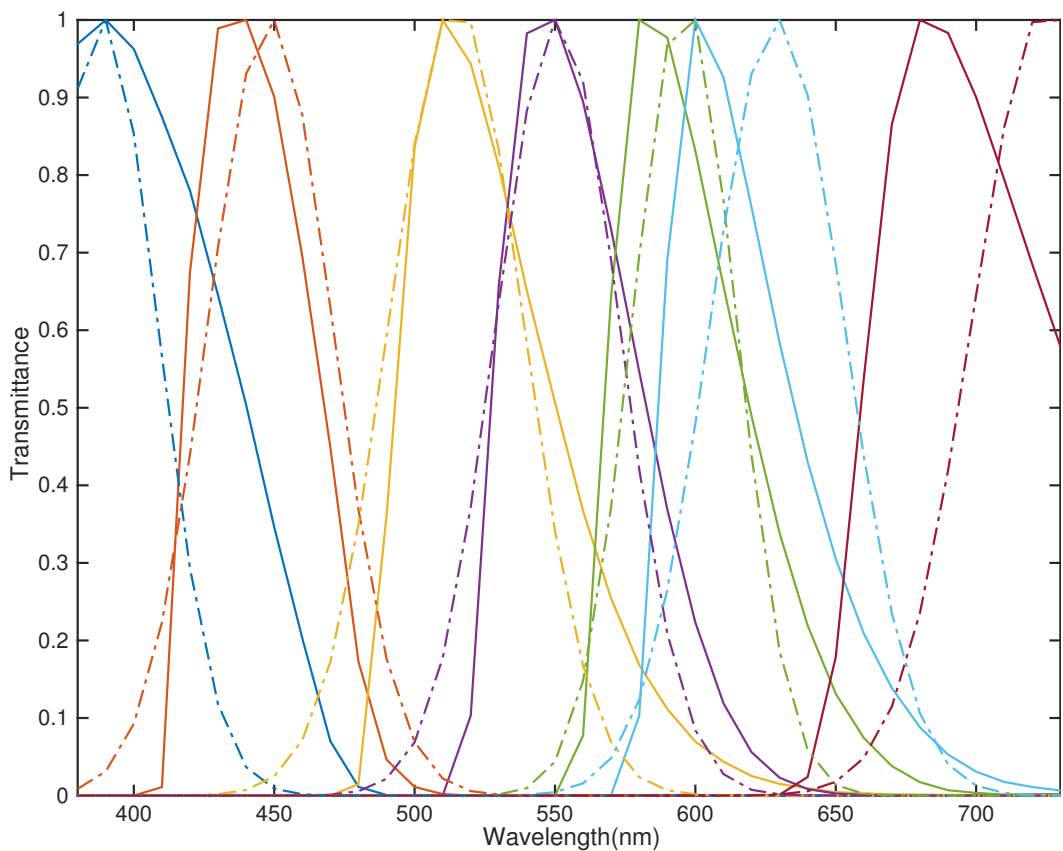


(a) Normalized spectral transmittance. Dash lines: theoretical Gaussian filters. Solid lines: selected sandwich filters.

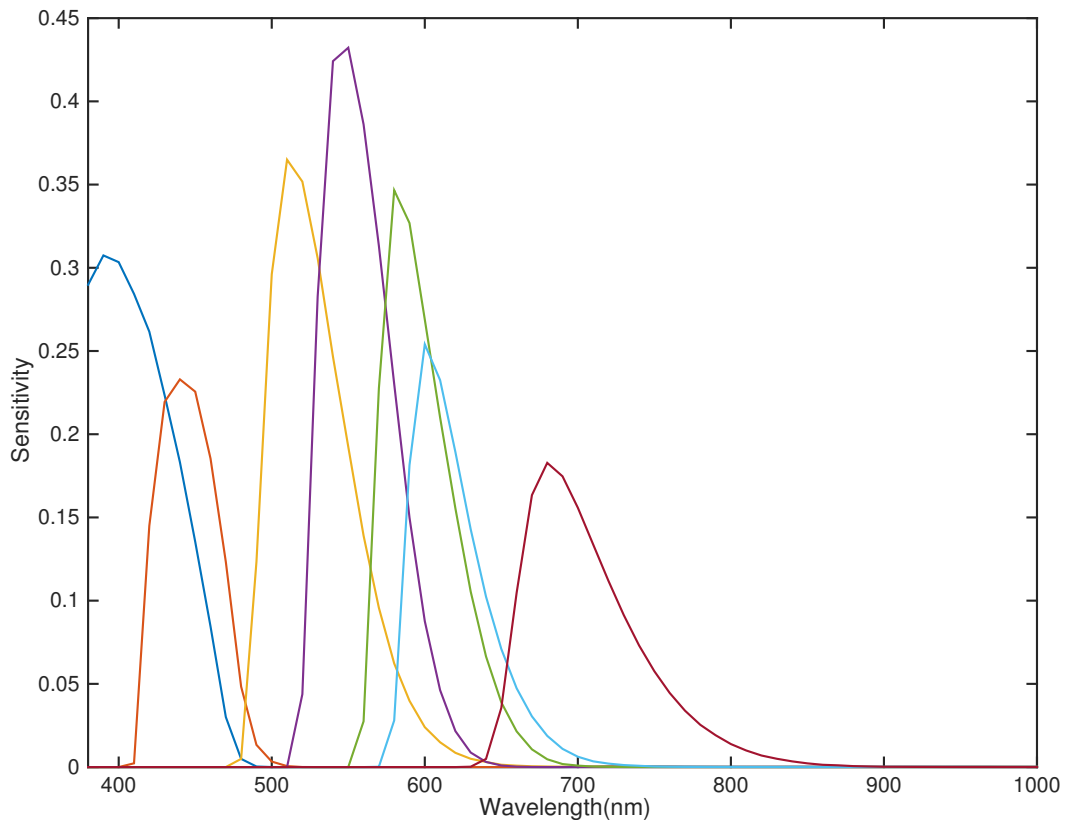


(b) Spectral sensitivity of the whole system including the FLI sensor and filters.

Fig. 4.3. – Filters selected from Schott database. The seventh sandwich filter incorporated KG5.

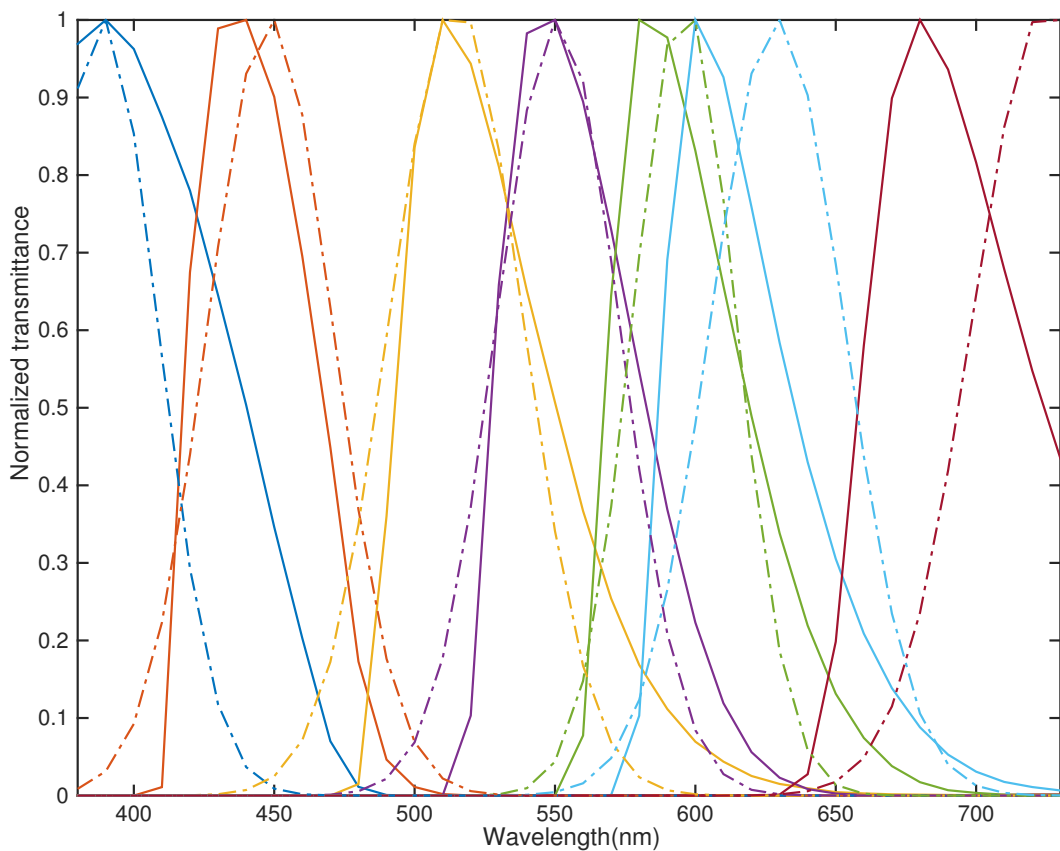


(a) Normalized spectral transmittance. Dash lines: theoretical Gaussian filters. Solid lines: selected sandwich filters.

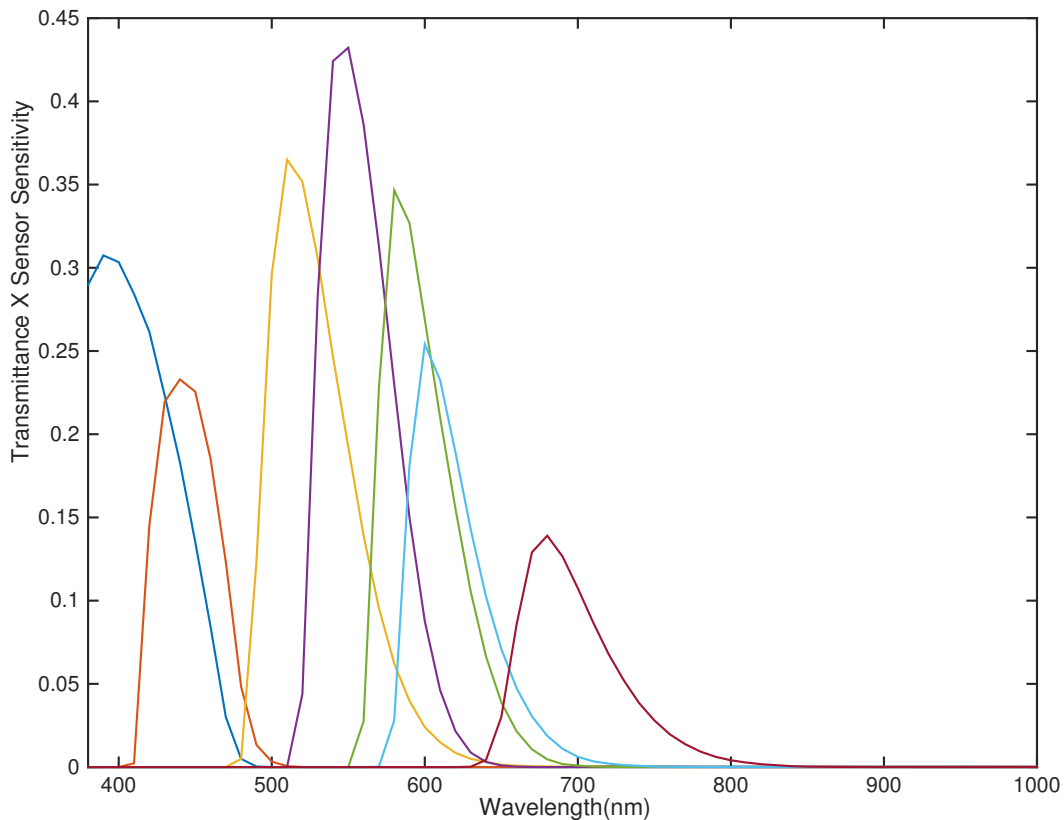


(b) Spectral sensitivity of the whole system including the FLI sensor and filters.

Fig. 4.4. – Filters selected from Andover database.



(a) Normalized spectral transmittance. Dash lines: theoretical Gaussian filters. Solid lines: selected sandwich filters.



(b) Spectral sensitivity of the whole system including the FLI sensor and filters.

Fig. 4.5. – Filters selected from Andover database. The seventh sandwich filter incorporated KG5.

The lists of specific filter names selected for other combinations of filters mentioned above can be found in Appendix A.

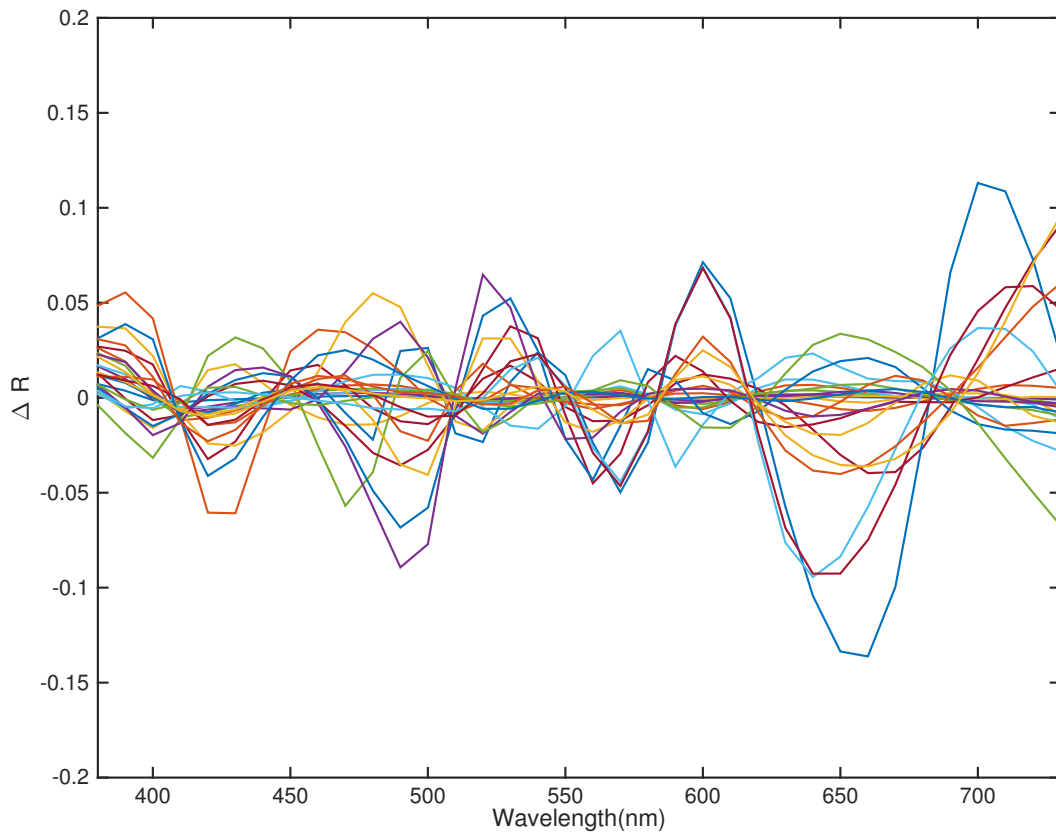
The spectral and color reproduction results of the sandwich filters in terms of RMSE, ΔE_{00} , noise and Q are shown in Table. 4.1. RMS, ΔE_{00} and noise of the selected Schott sandwich filters (except for 5mm available) are smaller than or close to the interference filters. The spectral property of the interference filters changes with incident light angle. The sandwich filters do not have this problem. Therefore, the sandwich filter should generate better image quality, by eliminating the need to introduce a wavelength dependent spatial correction.

Tab. 4.1. – The $\Delta E_{00,\sigma}$ and $RMSE$ of the APT using each listed filter set.

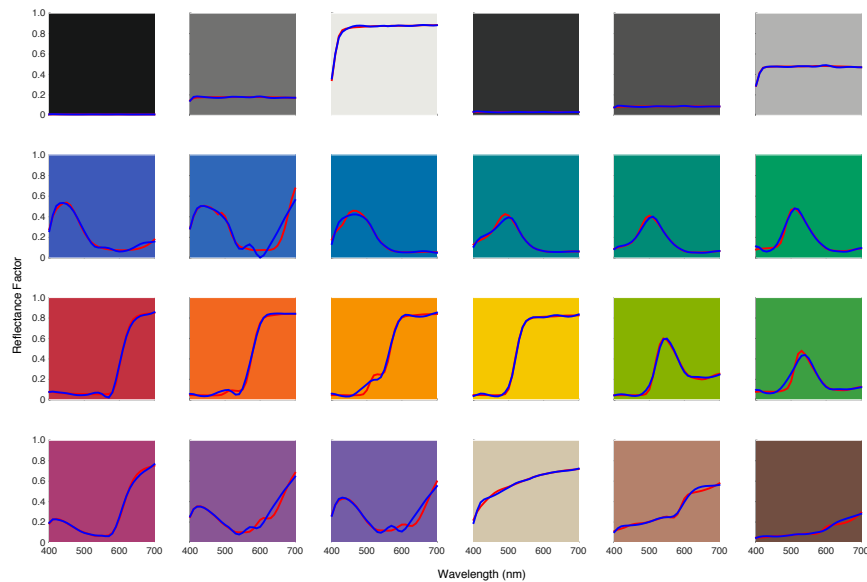
	$RMSE$	ΔE_{00}	$noise$	Q
Interference filter calculation data	0.014	0.48	1.54	1.180
Theoretical Gaussian filters	0.014	0.11	1.05	0.873
Schott A	0.015	0.31	1.52	1.151
Schott B	0.016	0.45	1.43	1.187
Schott C	0.015	0.32	1.52	1.154
5mm Schott	0.018	0.42	1.46	1.250
Andover A	0.018	0.28	1.08	1.056
Andover B	0.019	0.28	1.08	1.086
Theoretical Gaussian filters with UVIR	0.014	0.11	1.05	0.873
Schott D	0.016	0.46	1.12	1.048
Schott E	0.021	0.44	1.11	1.206
Andover C	0.024	0.26	1.07	1.226

Tab. 4.2. – The final selected filters, available from the Andover Corporation.

# sandwich filter	Filter 1	Filter 2
1#	BG25	BG25
2#	BG12	GG420
3#	BG23	GG495
4#	OG530	S8612
5#	BG40	OG570
6#	BG38	OG590
7#	KG5	RG665

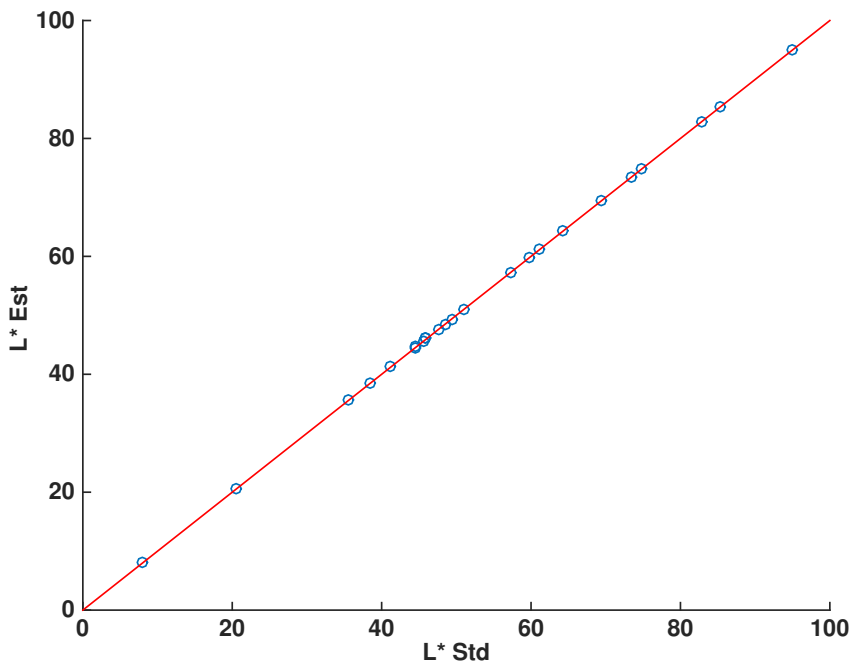


(a) Spectral reflectance difference between estimated and reference data for the APT.

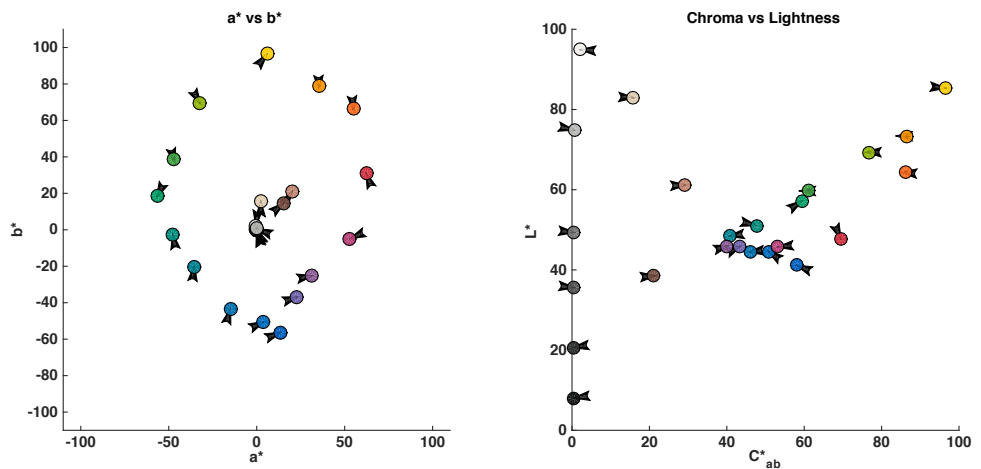


(b) Spectral reflectance difference between estimated and reference data for each patch of the APT.

Fig. 4.6. – Estimated and reference spectral reproduction.



(a) Lightness comparison between estimated and reference data for the APT. Red line: measured data. Blue line: predicted data.



(b) $a^* - b^*$ and $L^* - C_{ab}^*$ difference between estimated and reference data for the APT.

Fig. 4.7. – Estimated and reference colorimetric reproduction for the APT using the Andover B filter set.

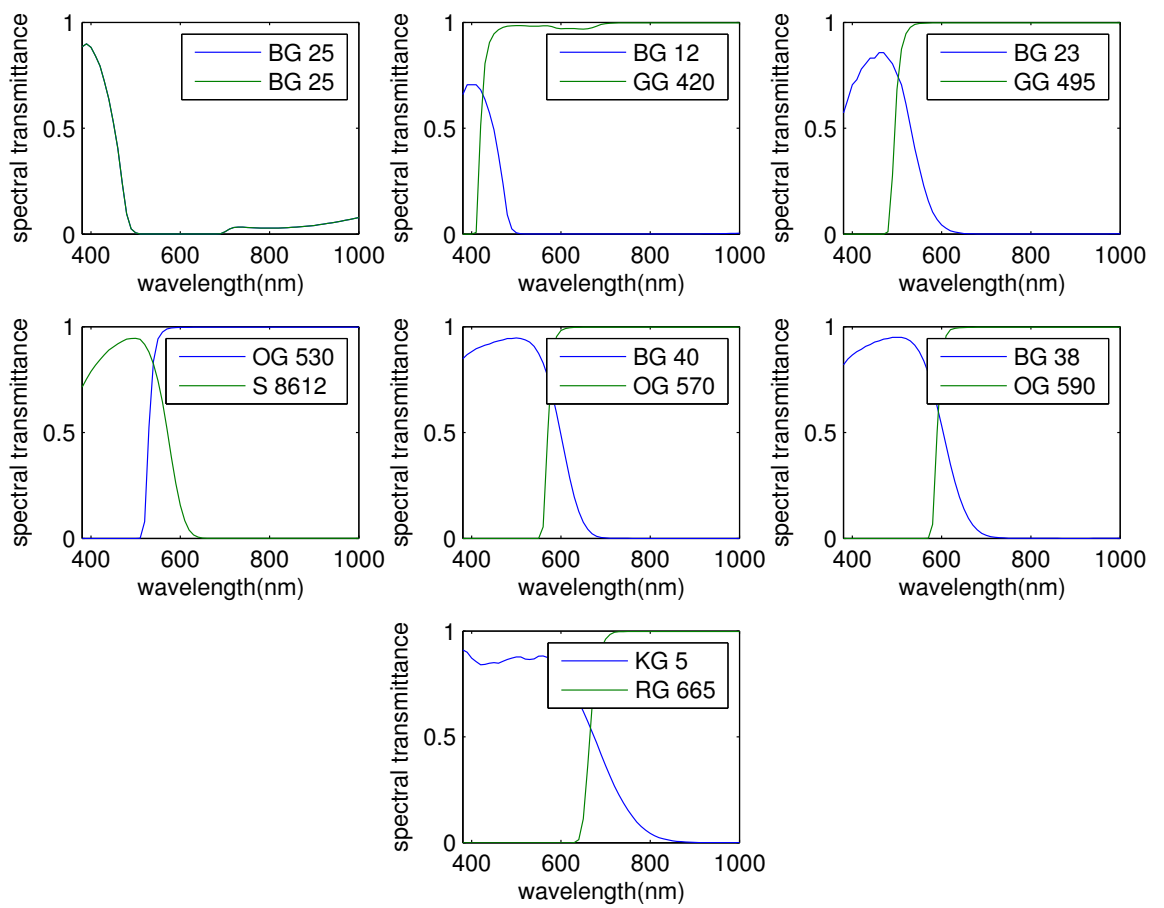


Fig. 4.8. – Spectral transmittance of the final selected filters

4.3 Subsets Selection Method

A flowchart of the subsets selection method is shown in Fig.4.9. Instead of trying to calculate corresponding metric values for all possible combinations ($4.3 * 10^{10}$) of filters, a more efficient way is to divide the spectrum of interest (400nm-750nm) evenly and select the combinations of filters whose peak wavelength were located in the range of spectrum subsets manually ($1.8 * 10^6$).

Seven-layer for-loops were built to calculate metric values for all possible combinations of the pre-selected filters. RMS, ΔE_{00} and noise were calculated using the technique and the equations in 3.2.2. The cost function Q was defined as:

$$Q = 40\overline{RMS} + 3\overline{\Delta E_{00}} + 1\overline{\sigma} \quad (4.6)$$

The scale factors were decided based on preliminary results with the aim of incorporating filter combinations having low noise for the next selection step.

Filter combinations were sorted in ascending order for Q and the top 1000 were selected for further analysis. Histograms of ΔE_{00} , noise and RMS are shown in Fig. 4.10 for the top 1000 filter combinations.

At first, the same cost function Q as the previous section was used. The same procedure was conducted. The selected optimal set of filter had $\Delta E_{00} = 0.281$, RMS = 0.0158 and noise = 2.73. The noise was much higher than all the selected filter sets in the previous chapter. Therefore, weightings in the cost function was adjusted to Eq. 4.6.

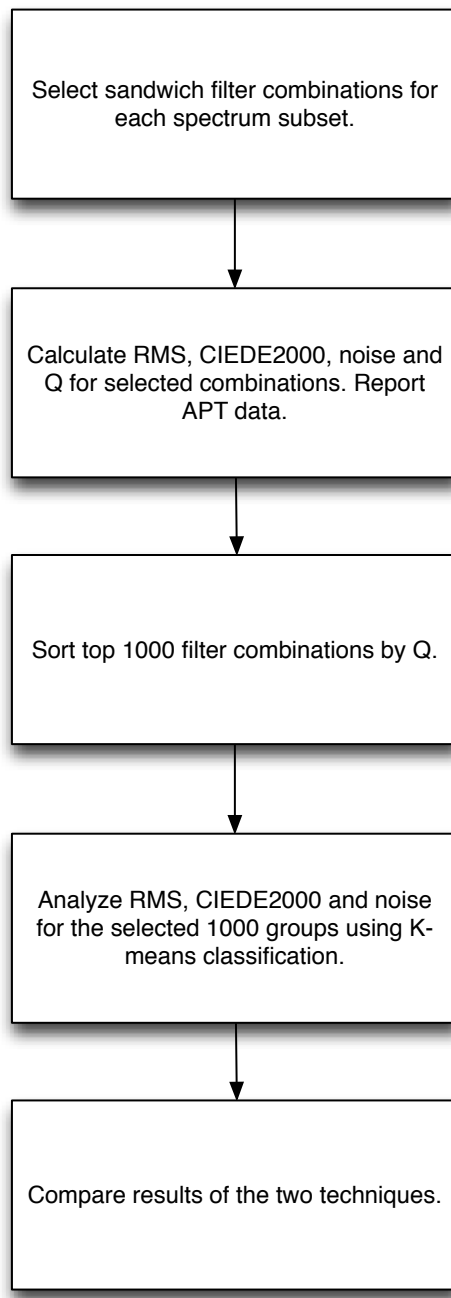
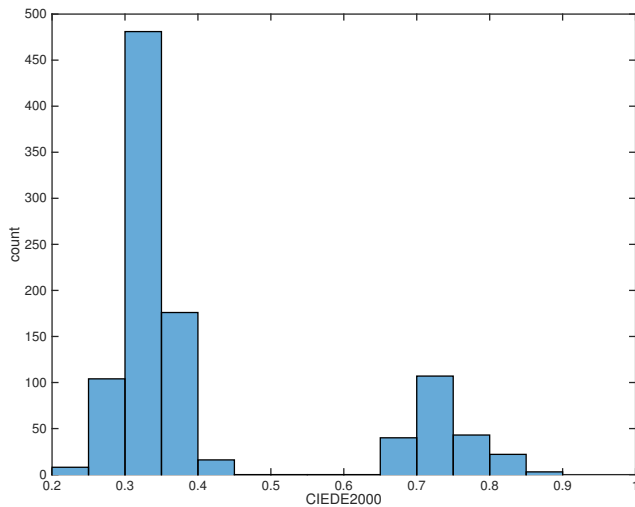
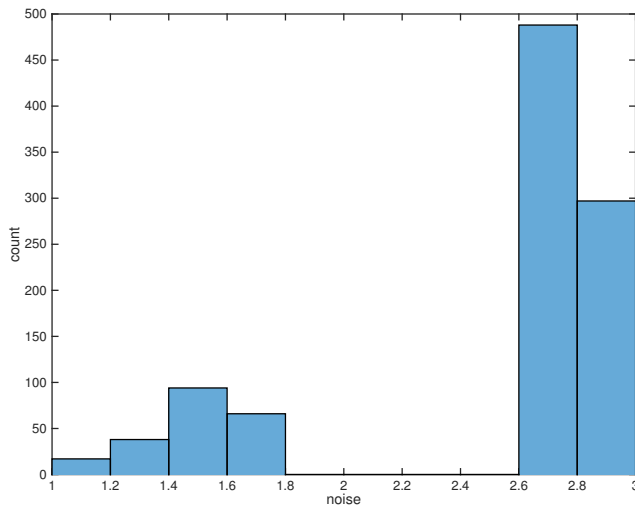


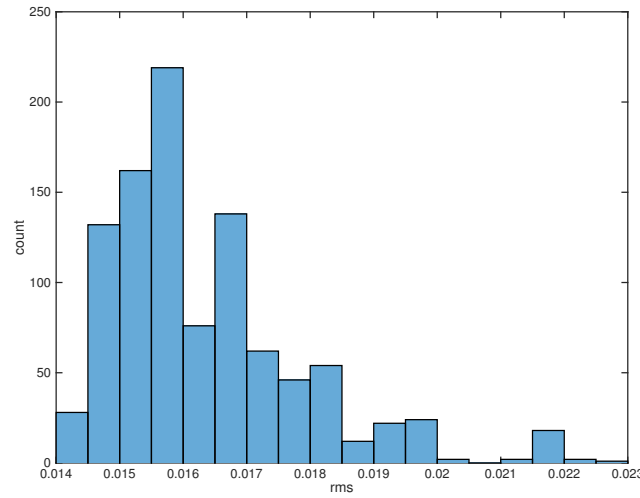
Fig. 4.9. – A flowchart of the subsets selection method.



(a) ΔE_{00} histogram.



(b) Propagated noise histogram.



(c) RMS histogram.

Fig. 4.10. – Histograms of ΔE_{00} , noise and RMS.

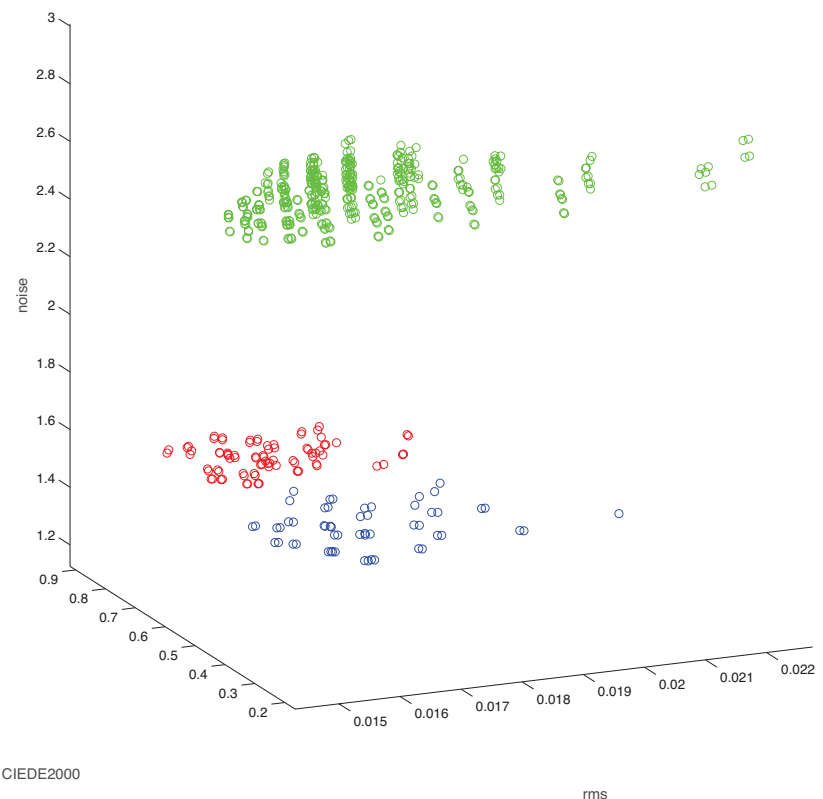


Fig. 4.11. – K-means classification results.

The K-means clustering can partition data and is a powerful tool to select useful subsets when dealing with large amounts of data. This technique was used to classify the top 1000 combinations. The results are shown in Fig. 4.11. The sandwich filters marked with blue circles have the lowest noise, and their ΔE_{00} are 0.7-0.9, which are high as is shown in the first plot in Fig. 4.10. There is a trade-off between noise and ΔE_{00} , which is in line with the last chapter. Compared to the results in Section 4.2 (noise 1.08, ΔE_{00} 0.28, RMS 0.019), for the top 1000 combinations whose noise are less than 1.6, ΔE_{00} are larger than 0.7. Therefore, the filters listed in Table 4.2 were purchased to build the multispectral camera.

4.4 Conclusions

Two methods were used to select sandwich filters considering spectral and colorimetric reproduction accuracy, noise, and throughput for the sensitivity range of the sensor. Compared to the traditional subsets selection method, the fitting Gaussians method was much more efficient and generated better results, providing insights for filter selection in multi-spectral camera design.

Single Schott Filter Selection

The previous chapters demonstrated filter selection models and theories, and how sandwich filters were selected. This chapter will describe single Schott filters selection for the same monochrome camera. Single Schott filters have high optical throughput, giving high signal-to-noise ratio. Similar to sandwich filters, its transmittance does not shift with incident angle. Using off-the-shelf single Schott filters can avoid the gluing procedure. Also, it is cost-effective.

5.1 Filter Selection Method and Results

A flowchart of the single Schott filter selection is shown in Fig.5.1. A UV/IR cut filter (Fig. 5.2) was included in the filter selection process since preliminary selected filters have high near infrared optical throughput. Seven-layer for-loops were built to calculate metric values for all 1326 combinations of filters manufactured by Schott. RMS and noise were calculated using the technique and equations as is shown in the seven-channel bandpass-filter set modeling. The cost function Q was defined as:

$$Q = 400\overline{RMS} + \bar{\sigma} \quad (5.1)$$

The scale factors were decided based on preliminary results with the aim of incorporating filter combinations having low noise.

Filter combinations were sorted in an ascending order for Q and the top 300 were selected for further analysis. Histograms of ΔE_{00} , noise and RMS are shown in Fig. 5.3.

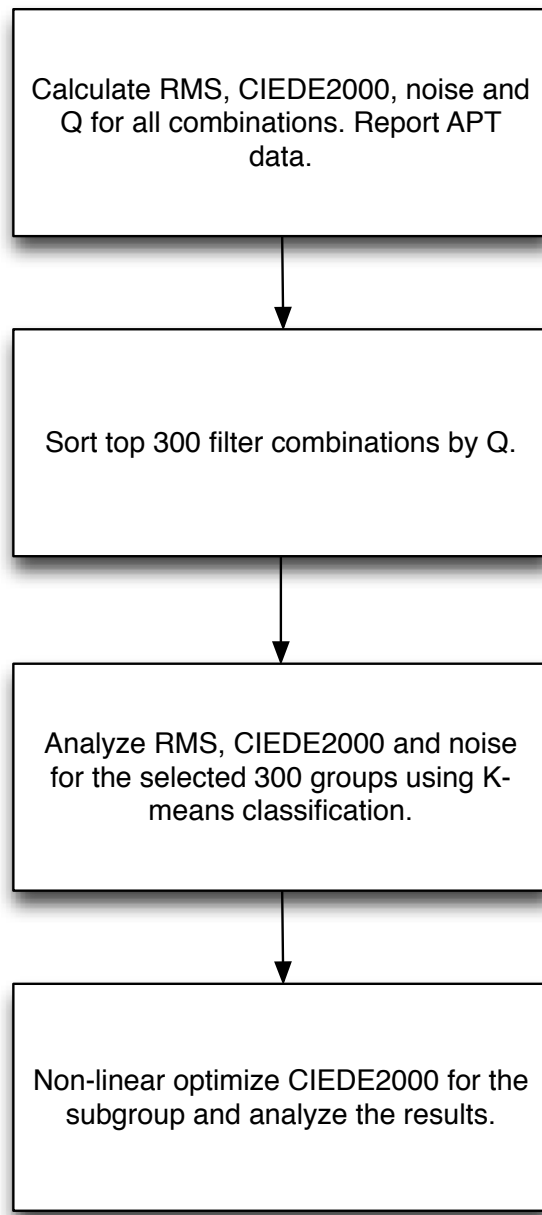


Fig. 5.1. – A flowchart of the single Schott filter selection.

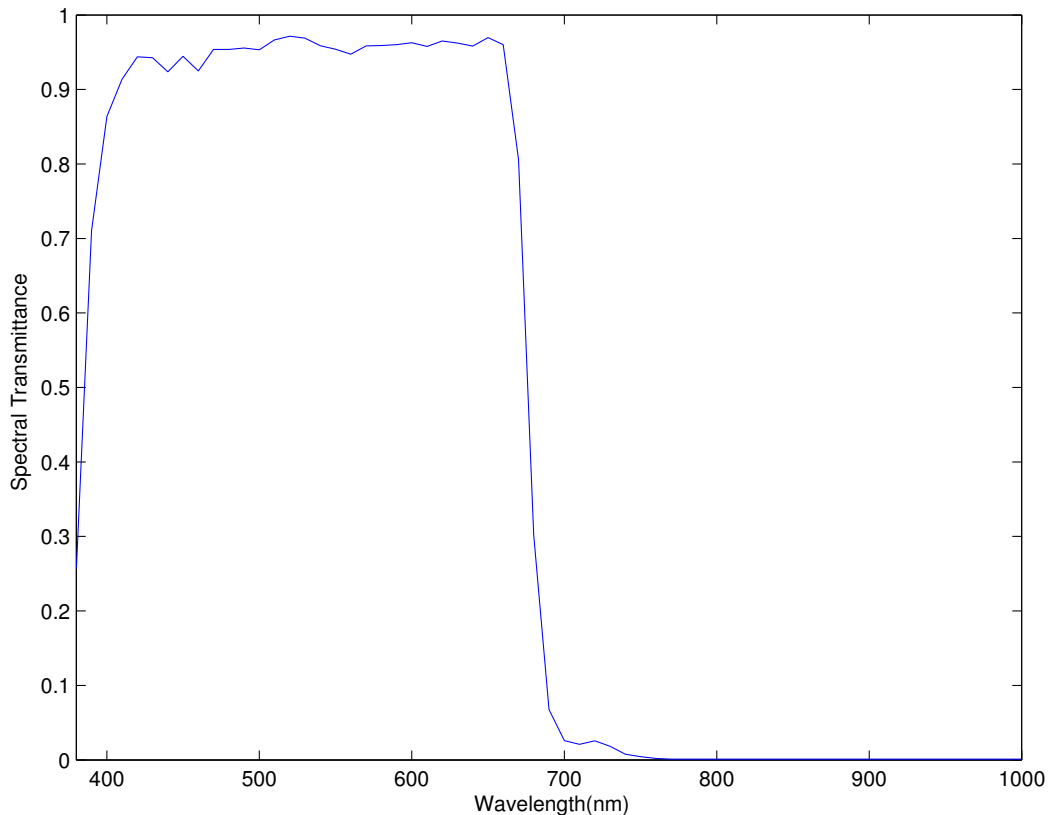


Fig. 5.2. – The spectral transmittance of the UV/IR cut visible bandpass filter.

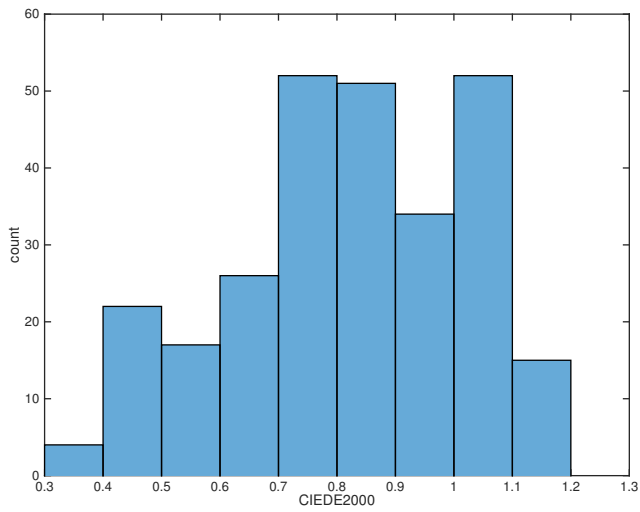
The K-means classification method was used to classify the top 300 combinations. The results are shown in Fig. 5.4. The green group (61 combinations) was selected since it had the lowest ΔE_{00} , noise and RMS.

Tab. 5.1. – The names of the selected filters in Fig.5.5.

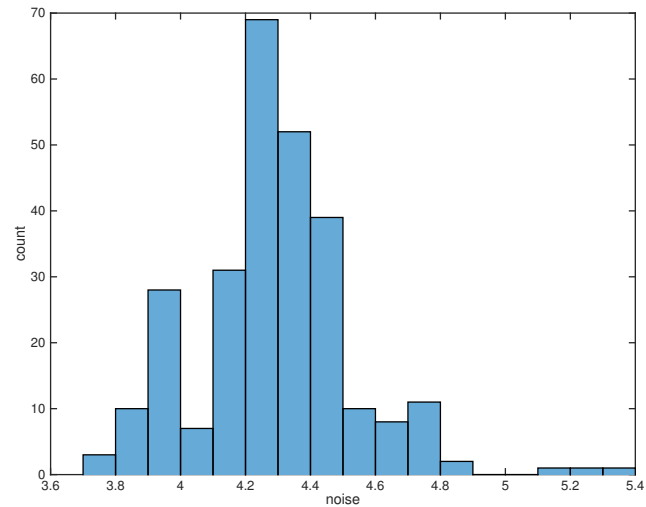
GG400	GG420	GG475	GG495	OG570	RG630	RG645
-------	-------	-------	-------	-------	-------	-------

Tab. 5.2. – Results of selected filters in Fig.5.5.

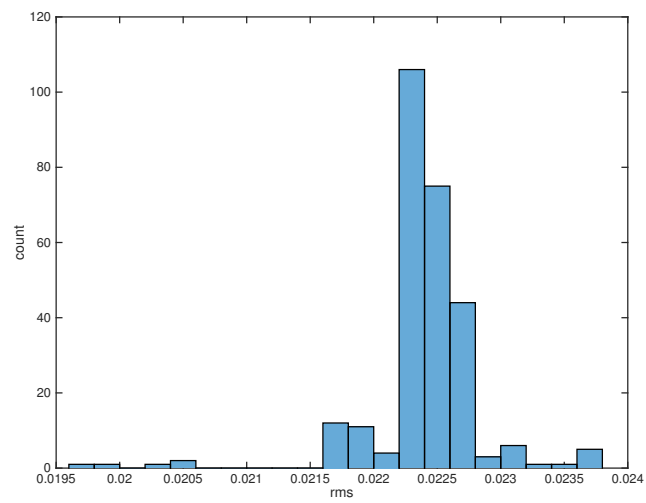
RMS	ΔE_{00}	σ
0.023	0.25	4.21



(a) ΔE_{00} histogram.



(b) Propagated noise histogram.



(c) RMS histogram.

Fig. 5.3. – Histograms of ΔE_{00} , noise and RMS for single Schott filter selection.

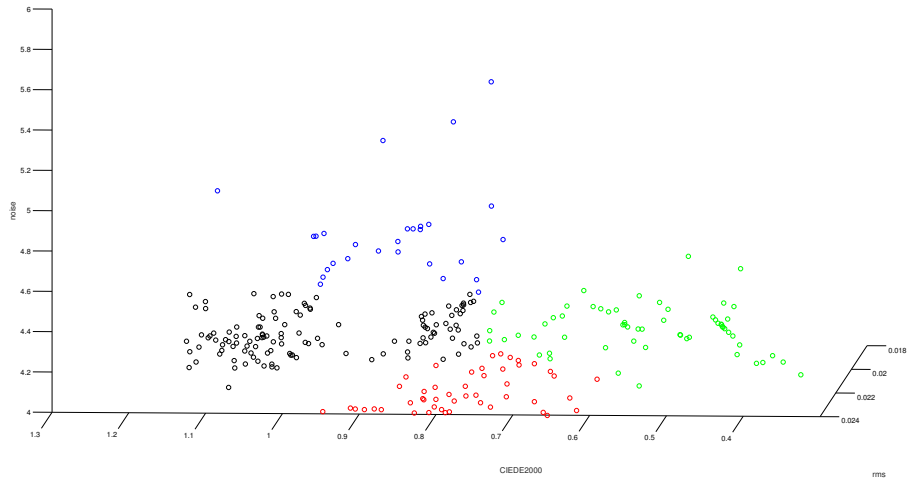
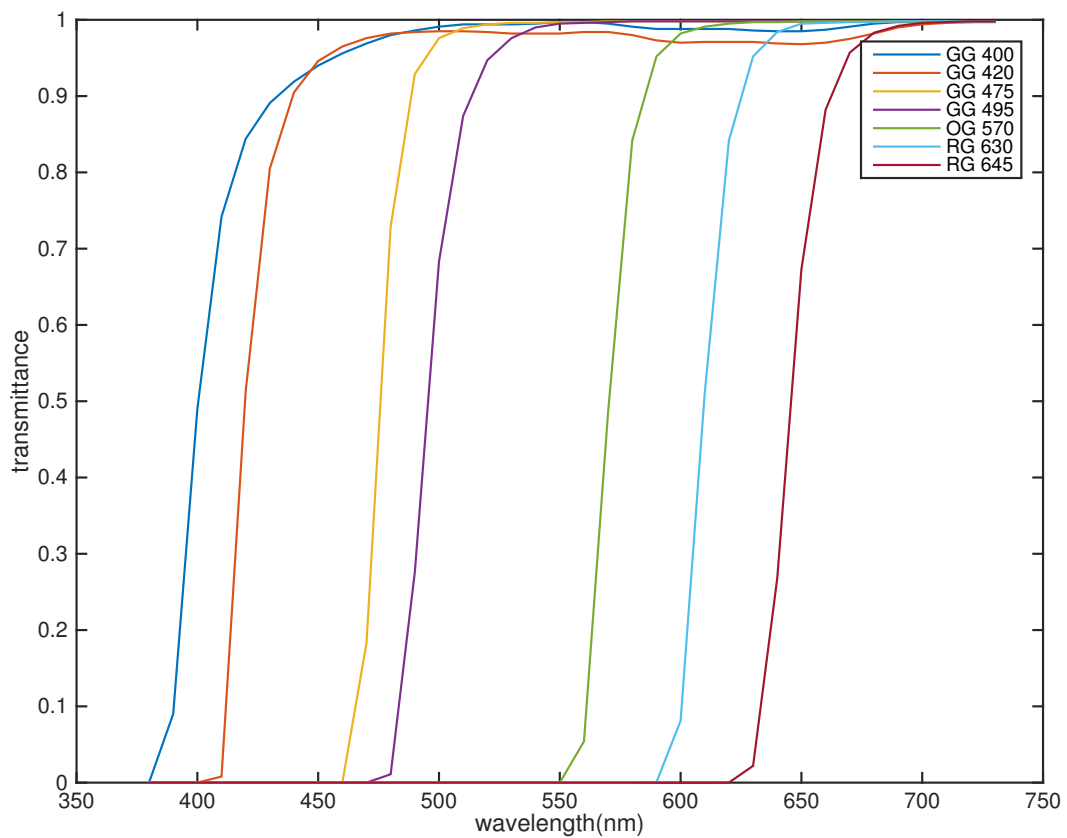


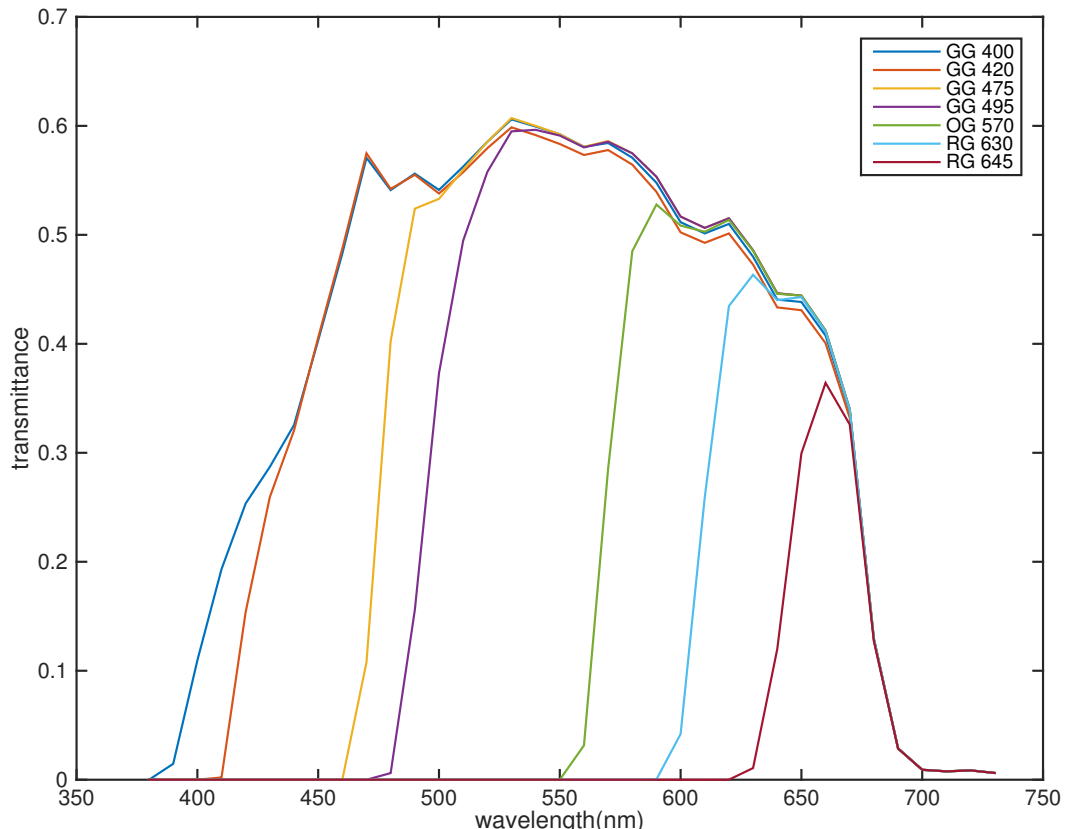
Fig. 5.4. – K-means classification results for single Schott filter selection.

Nonlinear optimization for ΔE_{00} was taken for the green group. The filter set whose ΔE_{00} was the smallest was selected. The selected filters are shown in Fig. 5.5 and Table 5.1. The spectral and colorimetric reproduction results are shown in Table 5.2.

The spectral reproduction results are shown in Fig. 5.6 (a) and (b). The long wavelength part has more errors because of the inclusion of the UV/IR cut filter. Tone reproduction results are shown in Fig. 5.6 (c). The errors were very small. Color reproduction results are shown in Fig. 5.6 (d). The errors were very small.

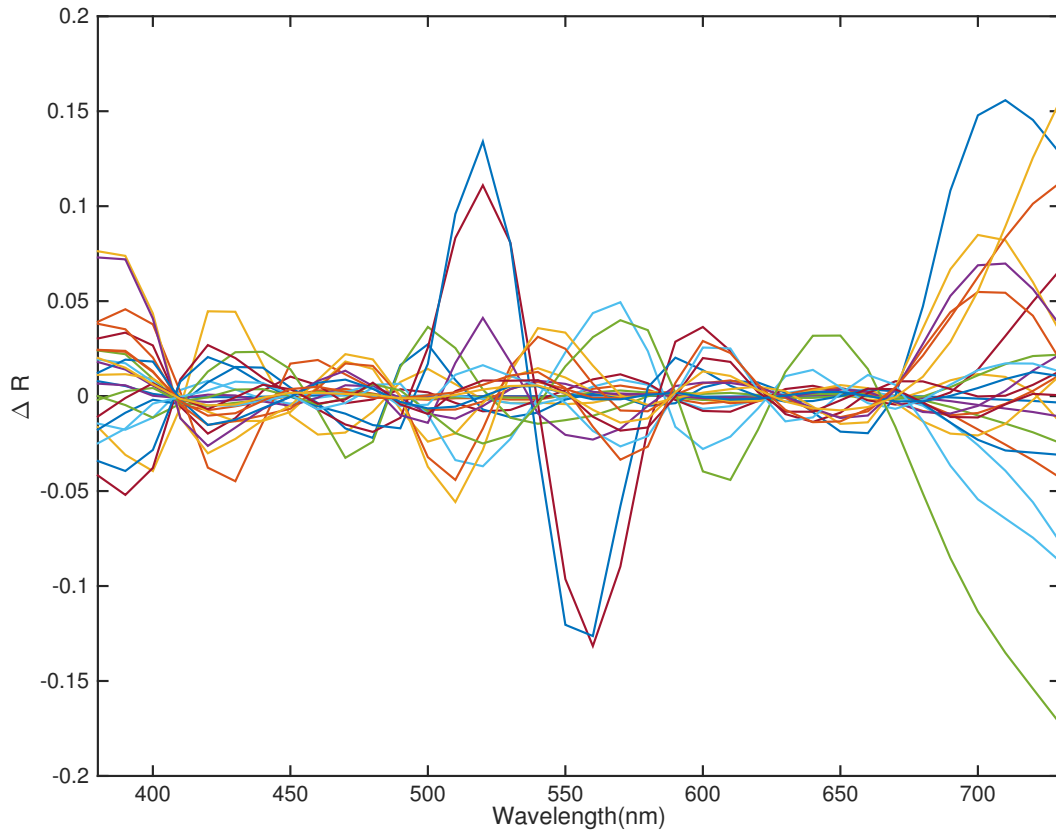


(a) Selected filter transmittance.

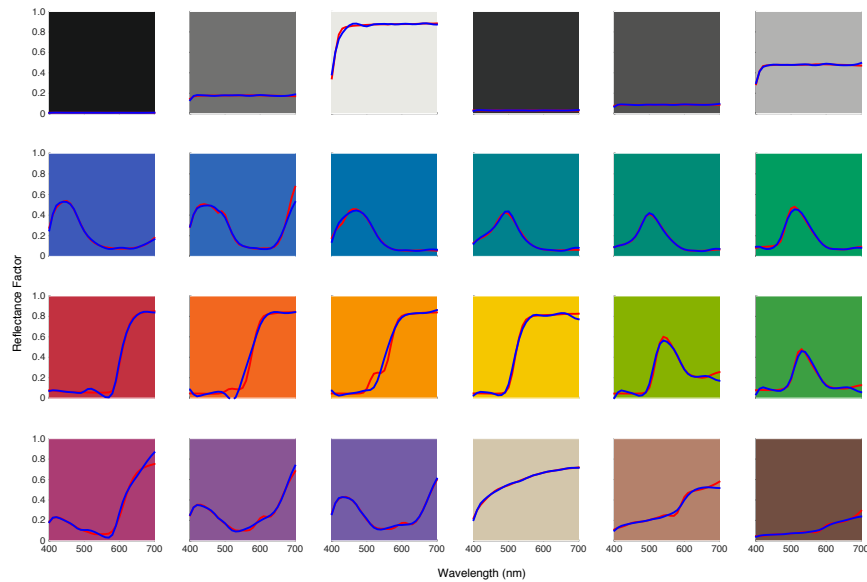


(b) System spectral sensitivity.

Fig. 5.5. – Selected filter transmittance and system spectral sensitivity for single Schott filter selection.

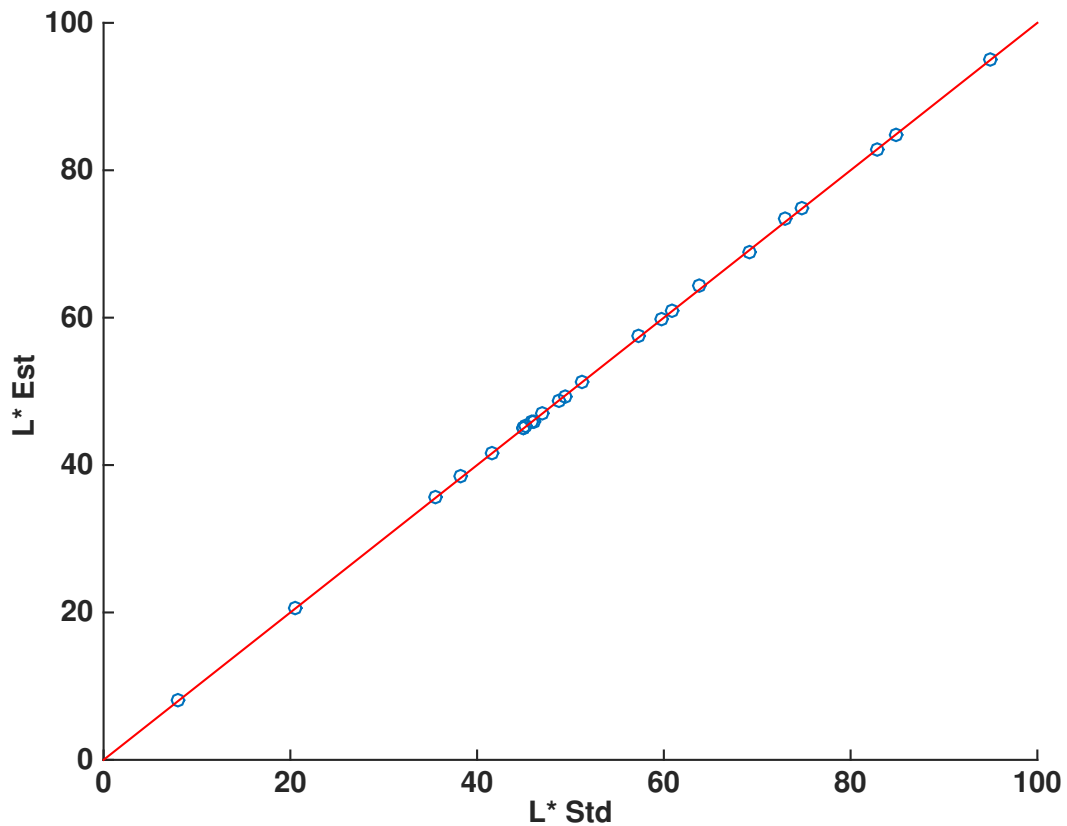


(a)The difference between estimated and reference spectral reflectance for the APT.

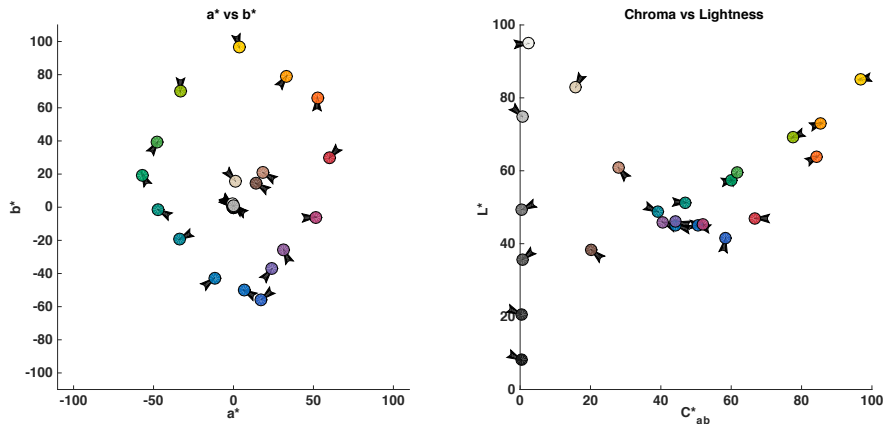


(b)Estimated and reference spectral reflectance for the APT.

Fig. 5.6. – Estimated and reference spectral and colorimetric reproduction for single Schott filter selection.



(c) Lightness difference between estimated and reference data for the APT.



(d) a^*b^* and $L^*C_{ab}^*$ difference between estimated and reference data for the APT.

Fig. 5.6. – Estimated and reference spectral and colorimetric reproduction for single Schott filter selection. (cont.)

5.2 Conclusions

The filter theories and models in Chapter 3 were used to select single Schott filters. The UV/IR cut filter was included because of sensor's infrared sensitivity and long pass filters transmitting infrared. The spectral and colorimetric reproduction of the selected filter set were accurate. However, although the signal-to-noise ratio of Schott long-pass filters is high, the propagated noise was still high because of the large overlap between the filters, resulting in color transformation noise. The filter selection method and results can provide insights as to the influence of design choices.

Experimental Verification

This chapter describes the spectral imaging process using sets of absorption and interference filters. The experimental setup, imaging, image processing and spectral reconstruction will first be described. Then the spectral and colorimetric accuracy and noise evaluation procedures will be introduced. Results of using the two imaging systems for four targets as both calibration and verification targets will be shown and discussed.

6.1 Apparatus

An air-cooled Finger Lakes Instrumentation (FLI) MicroLine ML50100 camera (using the Truesense microlens KAF-50100 sensor) was used. The quantum efficiency is shown in Fig. 6.1. The sensor can be cooled to 45°C below ambient to provide low-noise imaging. It has an 8176×6132 area array with $6\mu\text{m}$ pixels (http://www.icamera.com/spec_sheets/ML50100.pdf). For these experiments, the sensor was cooled to -20°C.

The lens was a Rodenstock APO-Rodagon-N 110mm f/4 with a modular (helical) focus. This enlarger lens was designed for film imaging and was one



Fig. 6.1. – The nominal quantum efficiency of the KAF-50100 sensor. (http://www.icamera.com/spec_sheets/ML50100.pdf)

of the lenses available in MCSL. The modulation transfer function (MTF) is shown in Fig. 6.2.

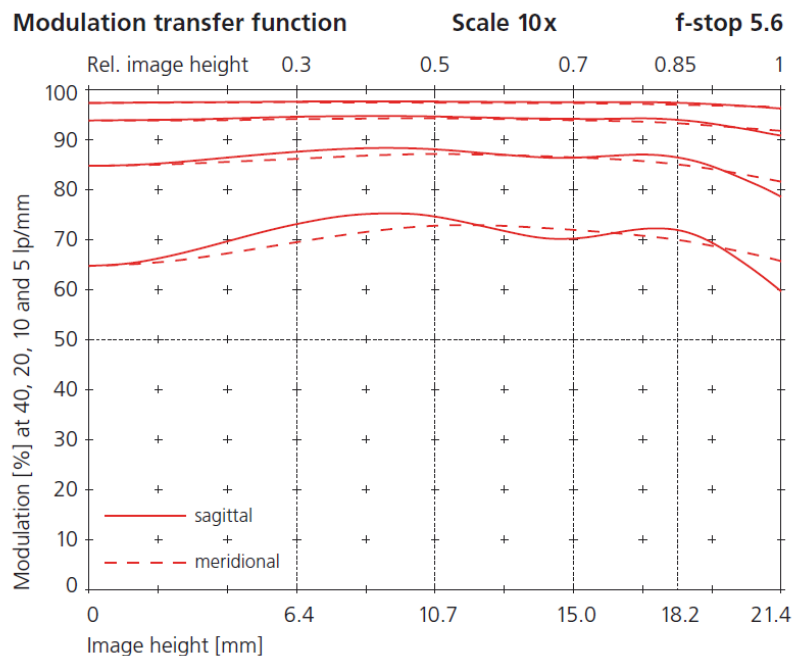


Fig. 6.2. – The modulation transfer function (MTF) of the Rodenstock lens.
[\(http://www.rodenstock-photo.com/Archiv/e_Rodenstock_Printing_CCD_43-62_8230.pdf\)](http://www.rodenstock-photo.com/Archiv/e_Rodenstock_Printing_CCD_43-62_8230.pdf)

Two sets of filters were used for the test: the set of interference filters first used by Burns [Burns, 1997] (Fig. 6.3) and the set of sandwich absorption filters ("Andover B") selected in Chapter 4. The interference filters have a bandwidth of 80nm with wavelength centers at 400nm, 450nm, 500nm, 550nm, 610nm, 640nm, 700nm. When this section was written, the filters had not been glued and no measured data was available yet.

Two different filter wheels were used. The first, a FLI CFW 2-7, held the 50mm diameter interference filters. This wheel was positioned in front of the lens. The second, a FLI CFW10-7, was part of the multispectral camera system under development at the time of this research. It holds seven 65mm square filters and was placed in front of the sensor. Attached to the wheel was an

FLI Atlas Focuser that was computer controlled, used for fine focus. The lens was attached to the focuser with a custom adapter manufactured by Precise Parts. The camera, strobes and filter wheel were remotely controlled by a Windows 98 OS desktop computer using an FLI utility (downloaded from www.flicamera.com/software/index.html). The imaging system configuration is shown in Fig. 6.4. A Manfrotto 405 geared head attached the camera to the stand.

A set of two Broncolor Pulso G Lamp 1600J strobes were used. P70 reflectors were attached to the front of the strobes.

Four targets were evaluated (Fig. 6.5): CCSG, APT, Target Justin, and Target Timo. They were used as calibration and validation targets for the spectral and colorimetric reproduction analysis. The latter two targets were developed by Timo Eckhard and Justin Ashbaugh. Both of the two targets were sets of patches painted using Golden Matte Fluid Acrylics artist paints. The goal of Target Timo was to sample CIELAB while the goal of Target Justin was

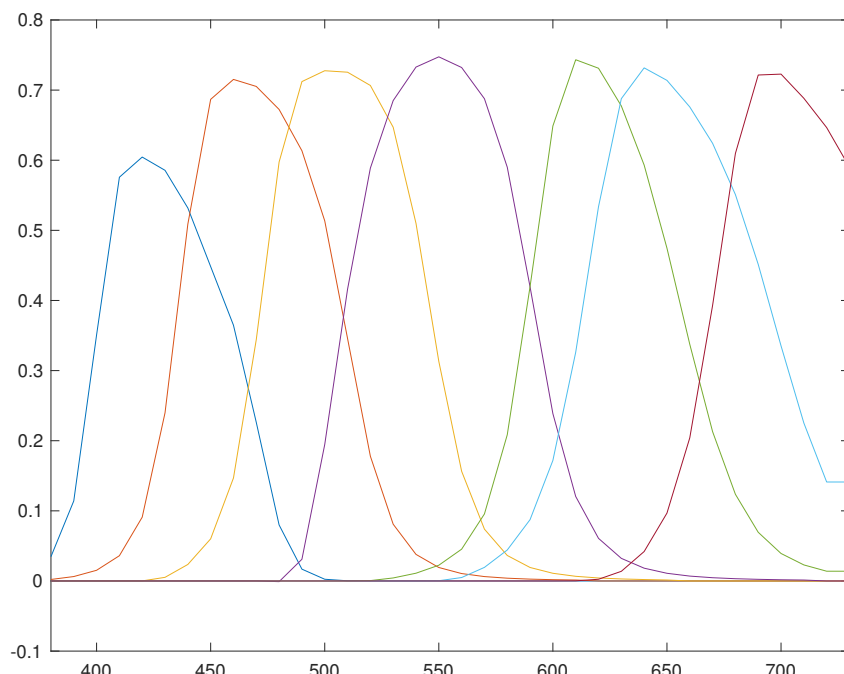


Fig. 6.3. – The spectral transmittances of the interference filter set.

to have several samples for each of the paints in MCSL's collection of matte acrylics.



(a) Front.



(b) Back.

Fig. 6.4. – Camera setup.



Fig. 6.5. – Four targets. Top left: APT. Top right: CCSG. Bottom left: Target Justin. Bottom right: Target Timo.

6.2 Experimental

6.2.1 Scene Set Up

45/0 measurement geometry was applied, i.e., the targets were placed perpendicular to the camera's optical axis, and the strobes were placed at approximately 45 degrees to the camera's optical axis. Both the camera and the strobes were aimed at the center of the image, approximating the spectrophotometer measurement geometry. The surround area was either matte black walls or covered in a black drop cloth to reduce optical flare. The scene geometry is shown in Fig.6.6.

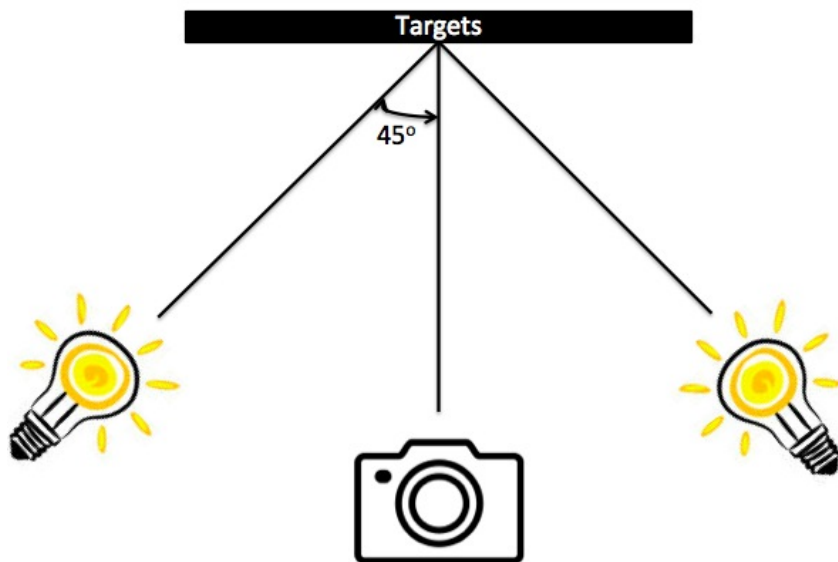


Fig. 6.6. – Scene geometry.

6.2.2 Imaging

Multispectral images were taken with each filter by rotating the filter wheel. All images were taken with the aperture set at f/5.6, the aperture with the highest

reported MTF. The strobe energy was adjusted for each filter to achieve 16 bit signals between 52,000 and 58,000 for one of the calibration target's white patch.

An image of a uniform matte white board (usually 0.5" foamcore) was taken for every channel and used as a flatfield to correct for the spatial non-uniformity of the light source and pixel-to-pixel gain variation of the sensor. A low pass spatial filter was applied to the white board images to remove any texture in the board. The spectral reflectance of the white board was lower than that of the target white in most of the wavelength range (Fig.6.7). Therefore, the alignment of the spectral reflectance of the white board with that of the white patch was necessary to avoid clipping. However, the wavelength-by-wavelength correction was not practical in this wide-band capture system. A compromise way was to align their average pixel values rather than their spectral reflectance. A flat-fielding factor F_n was calculated using Eq. 6.1:

$$F_n = \frac{\text{Average}(D_{whiteboard,n}) - D_{offset,n}}{\text{Average}(D_{whitepatch,n}) - D_{offset,n}} \times 0.88 \quad (6.1)$$

where $D_{whiteboard,n}$ is the pixel value of the white board, $D_{whitepatch,n}$ is the pixel value of the target white patch, $D_{offset,n}$ is the pixel value of an offset, n is the n th channel. The scalar 0.88 was an arbitrary chosen number to leave some "head room" between a diffuse white and any specular highlights. The spatially corrected pixel values of the i th patch in the n th channel $D_{i,n,corr}$ was calculated using Eq. 6.2:

$$D_{i,n,corr} = \left(\frac{D_{i,n,uncorr} - D_{offset,n}}{D_{whiteboard,n} - D_{offset,n}} \right) \cdot F_n \quad (6.2)$$

where $D_{i,n,uncorr}$ is the uncorrected pixel values of the i th patch in the n th channel.

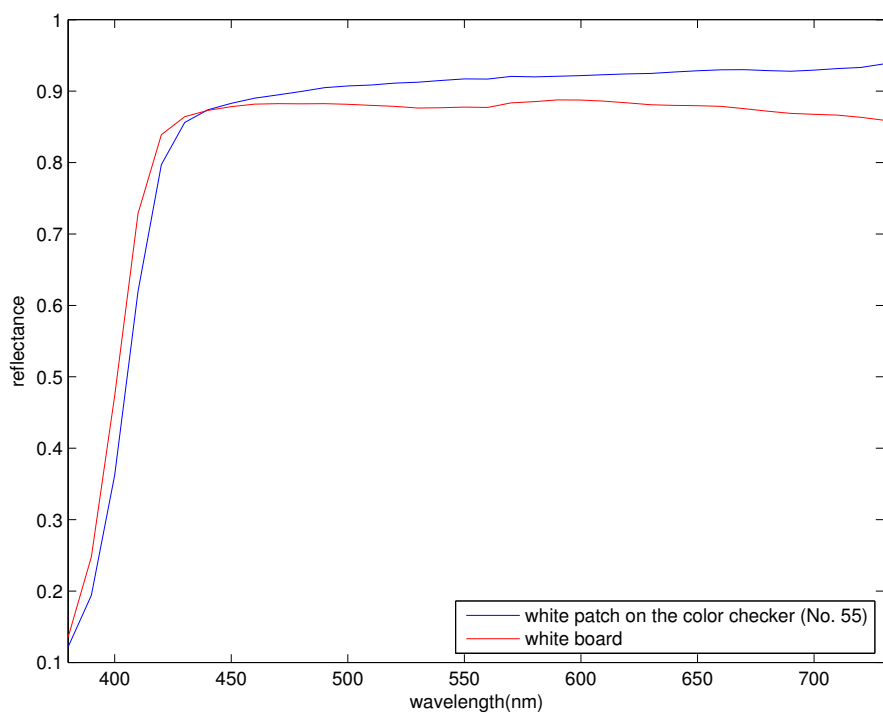


Fig. 6.7. – Spectral reflectance of the ColorChecker SG white patch (blue line) and the white board (red line).

6.2.3 Image Processing and Spectral Reconstruction

A summary of the experimental workflow is shown in Fig. 6.8.

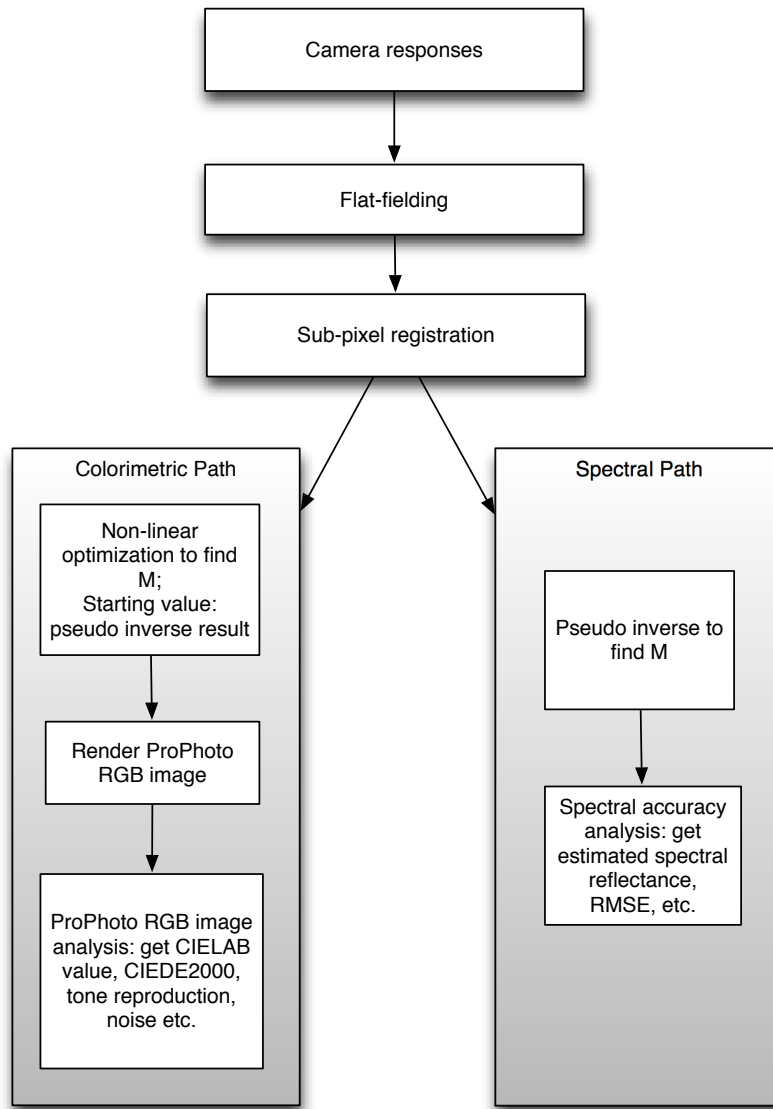


Fig. 6.8. – Experimental workflow.

A sub-pixel registration method reported in [Guizar-Sicairos et al., 2008] was used to register all the flat-fielded spectral images. This method used non-linear optimization and a two-step matrix-multiply discrete Fourier transform to register images. The initial upsampled cross correlation factor k was set to 2. The first step of the DFT algorithm upsampled a 1.5x1.5 pixel region with initial cross correlation factor $k_1 \simeq k^{(1/2)}$ and non-linear optimization was used to find the cross-correlation peak. For the second step, a $3/k_1 \times 3/k_1$ region in the original grid was upsampled and further refined for the peak location.

As is shown in Fig. 6.8, colorimetric and spectral paths were separated for more accurate colorimetric and spectral reproduction. Minimizing spectral RMS error does not result in minimal colorimetric error [Zhao et al., 2005; Zhao and Berns, 2007]. The colorimetric path is shown in Eq. 6.3. The offsets compensate for the dark current and the flare in the optical system that comes from the diffuse light because of the geometry differences between the reference spectrophotometer and lighting. The offsets are included into the color transformation matrix (\mathbf{M}) as a column for further optimization.

The colorimetric path has a two-step optimization. For the first step, \mathbf{M} (including the offset column) was nonlinearly optimized (fminunc in MATLAB) to minimize the average ΔE_{00} between the predicted and measured data for the calibration target, with the pseudo-inverse of Eq. 6.3 as starting value \mathbf{M}_0 . The average patch value instead of the per-pixel values was used because it can reduce the effect of misregistration, it generated less noise, and it was more efficient computationally. The starting values of the offsets were all set to an arbitrary chosen number 0.001 for the optimization. All of the coefficients in \mathbf{M}_0 (including the offset column) were updated simultaneously in the non-linear optimization. For the second step, the cost function was noise+ ΔE_{00} . Noise was calculated using Eq. 3.11.

$$XYZ_i = \mathbf{M} \cdot \text{Average}(D_{i,n,corr}) \quad (6.3)$$

where XYZ_i are the estimated tristimulus value of the i th patch. $Average(D_{i,n,corr})$ are the average camera signals for the i th channel after flat-fielding and offset correction (Eq. 6.2).

The color transformation matrix \mathbf{M} of the colorimetric path was used to render 16-bit ProPhoto RGB images. ProPhoto was selected to avoid encoding errors of high-chroma colors. First, the flat-fielded image pixel values $D_{i,n,corr}$ were calculated in Eq. 6.2. The conversion from $D_{i,n,corr}$ to tristimulus values XYZ is shown in Eq. 6.4. The conversion from tristimulus values to ProPhoto linear RGB RGB_{linear} is shown in Eq. 6.5 [Sharma and Bala, 2002].

$$XYZ = \mathbf{M} \cdot D_{i,n,corr} \quad (6.4)$$

$$RGB_{linear} = \mathbf{M}_{\text{ProPhotoRGB}} \cdot XYZ \quad (6.5)$$

where

$$\mathbf{M}_{\text{ProPhotoRGB}} = \begin{bmatrix} 1.3459 & -0.2556 & -0.0511 \\ -0.5446 & 1.5082 & 0.0205 \\ 0 & 0 & 1.2118 \end{bmatrix} \quad (6.6)$$

Therefore the conversion from $D_{i,n,corr}$ to ProPhoto linear RGB is calculated by Eq. 6.7

$$RGB_{linear} = \mathbf{M}' \cdot D_{i,n,corr} \quad (6.7)$$

where

$$\mathbf{M}' = \mathbf{M}_{\text{ProPhotoRGB}} \cdot \mathbf{M} \quad (6.8)$$

The pre-multiplication to calculate \mathbf{M}' using Eq. 6.8 reduced the number of per-pixel calculations.

The ProPhoto RGB images were saved using the gamma corrected RGB_{linear} value, which were calculated in Eq. 6.9.

$$RGB_{ProPhoto} = \begin{cases} 0 & RGB_{linear} < 0.0 \\ 16RGB_{linear}I_{max} & 0.0 < RGB_{linear} < E_t \\ (RGB_{linear})^{\frac{1}{1.8}}I_{max} & E_t \leq RGB_{linear} \leq 1.0 \\ I_{max} & RGB_{linear} \geq 1.0 \end{cases} \quad (6.9)$$

where

I_{max} is the maximum integer value used in the encoding function (65535 for 16-bit configuration)

and

$$E_t = 16^{1.8/(1-1.8)} = 0.001953.$$

For the spectral path, the color transformation matrix was obtained by calculating the pseudo-inverse result for average value in a manually selected mask for each patch (Eq. 6.10) of the calibration targets. The the color transformation matrix of the spectral path was used to reconstruct the spectral reflectances (Eq. 6.11).

$$\mathbf{M} = R_{\lambda,i,n} \cdot Average(D_{i,n,corr})^\dagger \quad (6.10)$$

where $R_{\lambda,i,n}$ is the spectral reflectance of the i th patch for each channel that were measured by an X-rite i1-Pro spectrophotometer .

$$R'_{\lambda,i,n} = \mathbf{M} \cdot D_{i,n,corr} \quad (6.11)$$

where $R'_{\lambda,i,n}$ is the reconstructed spectral reflectance of the i th patch for each channel.

6.2.4 Spectral and Colorimetric Accuracy Evaluation

Spectral Accuracy Evaluation

The spectral reflectance for the i th patch ($\overline{R}_{\lambda,i}$) was estimated from the product of M in Eq. 6.10 and the multi-channel image of each channel. The difference between $\overline{R}_{\lambda,i}$ and the measured spectral reflectance for each patch ($\Delta R_{\lambda,i}$) was calculated. The average root-mean-square error for all the color targets was used to evaluate the spectral accuracy of each imaging system.

Colorimetric Accuracy Evaluation

User-defined masks were applied on each target of the ProPhoto RGB image. Each patch mask had between 30,000-120,000 pixels since the targets had different sizes in the image. The RGB value for each pixel within the masks were obtained and converted to $L^*a^*b^*$ space. First, the inverse of Eq. 6.9 was used to calculate XYZ. Second, the XYZ were converted to $L^*a^*b^*$. The average of $L^*a^*b^*$ value were used to calculate the average ΔE_{00} for each patch. The ΔE_{00} between the mean $L^*a^*b^*$ of each patch and the sum of the mean and the standard deviation of each patch was used to define the colorimetric noise.

Both the spectral and colorimetric accuracy evaluation was performed for all the targets in the ProPhoto RGB image: Target Timo, Target Justin, CCSG, and Target APT. A T-test was used to determine whether the mean results from the interference filters and sandwich absorption filters were statistically significantly different from each other.

6.3 Spectral and Colorimetric Reproduction Results and Discussion

6.3.1 Evaluation of Filter Sets

Spectral and Colorimetric Accuracy Evaluation Results

The data from all of the four targets were used in different combinations of calibration and verification datasets. The ΔE_{00} , RMSE and noise results are listed in Tables 6.1- 6.4. For each of the metrics, the statistical results across three verification target results (excluding the results from the calibration target) and a combined result for the two sets of filters are shown in Table 6.5. The same metric Q in Section 3.2.2 for seven-theoretical-filter optimization was used as the combined metric to summarize the spectral, colorimetric and noise performance of the two sets of filters (Eq. 3.10).

Tab. 6.1. – Results of the spectral and colorimetric reproduction and noise for the sandwich absorption and interference filters. Calibration target: Timo. Verification targets: APT, Justin, and CCSG.

Sandwich filters						
Targets		Timo	APT	Justin	CCSG	Verification avg
ΔE_{00}	Avg	1.11	1.19	1.17	1.75	1.37
	Min	0.03	0.31	0.24	0.24	0.26
	Max	4.39	6.25	4.57	6.69	5.84
	90th%	2.37	1.82	1.99	4.29	2.7
RMSE	Avg	0.014	0.027	0.013	0.015	0.018
	Min	0.004	0.014	0.003	0.007	0.008
	Max	0.035	0.055	0.029	0.031	0.038
	90th%	0.021	0.043	0.022	0.021	0.028
Noise	Avg	0.92	1.02	1.06	1.24	1.11
	Min	0.33	0.39	0.33	0.36	0.36
	Max	4.12	3.51	5.73	4.29	4.51
	90th%	1.62	1.86	1.92	2.93	2.24
Interference filters						
Targets		Timo	APT	Justin	CCSG	Verification Avg
ΔE_{00}	Avg	1.12	1.89	1.34	1.98	1.74
	Min	0.04	0.68	0.22	0.4	0.43
	Max	4.69	5.49	4.83	6.36	5.56
	90th%	2.12	3.00	2.20	4.71	3.30
RMSE	Avg	0.021	0.033	0.017	0.008	0.019
	Min	0.004	0.008	0.003	0.002	0.004
	Max	0.059	0.088	0.048	0.022	0.053
	90th%	0.038	0.054	0.034	0.013	0.033
Noise	Avg	1.36	1.49	1.44	2.00	1.64
	Min	0.37	0.43	0.34	0.45	0.40
	Max	10.33	7.59	10.74	9.68	9.33
	90th%	2.43	2.83	2.51	5.83	3.72
Patch Number		110	24	100	140	264

Tab. 6.2. – Results of the spectral and colorimetric reproduction and noise for the sandwich absorption and interference filters. Calibration target: APT. Verification targets: Timo, Justin, and CCSG.

Sandwich filters						
Targets		Timo	APT	Justin	CCSG	Verification avg
ΔE_{00}	Avg	1.44	0.69	1.01	1.56	1.34
	Min	0.11	0.08	0.15	0.28	0.18
	Max	8.58	1.88	6.38	5.75	6.9
	90th%	2.8	1.46	1.7	2.95	2.48
RMSE	Avg	0.016	0.023	0.014	0.013	0.014
	Min	0.006	0.008	0.004	0.006	0.005
	Max	0.038	0.046	0.031	0.028	0.032
	90th%	0.024	0.037	0.023	0.019	0.022
Noise	Avg	0.95	1.11	1.07	1.37	1.13
	Min	0.36	0.4	0.36	0.39	0.37
	Max	3.74	4.16	5.24	5.47	4.82
	90th%	1.7	2.11	1.9	3.38	2.33
Interference filters						
Targets		Timo	APT	Justin	CCSG	Verification Avg
ΔE_{00}	Avg	2.09	0.87	1.11	1.81	1.67
	Min	0.36	0.08	0.14	0.25	0.25
	Max	8.21	3.6	3.33	5.64	5.72
	90th%	3.26	1.5	2.28	4.17	3.23
RMSE	Avg	0.016	0.022	0.013	0.012	0.014
	Min	0.006	0.008	0.004	0.004	0.005
	Max	0.038	0.042	0.029	0.030	0.032
	90th%	0.026	0.031	0.021	0.017	0.021
Noise	Avg	1.24	1.48	1.33	1.76	1.44
	Min	0.38	0.48	0.36	0.42	0.39
	Max	7.34	6.76	8.56	7.54	7.81
	90th%	2.28	2.81	2.39	4.86	3.18
Patch Number		110	24	100	140	350

Tab. 6.3. – Results of the spectral and colorimetric reproduction and noise for the sandwich absorption and interference filters. Calibration target: Justin. Verification targets: Timo, APT, and CCSG.

Sandwich filters						
Targets		Timo	APT	Justin	CCSG	Verification avg
ΔE_{00}	Avg	1.52	1.03	0.86	1.35	1.3
	Min	0.21	0.2	0.06	0.22	0.21
	Max	6.26	3.19	5.88	5.74	5.06
	90th%	2.95	2.69	1.68	2.45	2.7
RMSE	Avg	0.016	0.029	0.012	0.015	0.02
	Min	0.003	0.011	0.003	0.006	0.007
	Max	0.031	0.05	0.027	0.033	0.038
	90th%	0.024	0.048	0.02	0.021	0.031
Noise	Avg	0.92	1.06	1.02	1.28	1.09
	Min	0.34	0.44	0.37	0.38	0.38
	Max	3.62	3.67	5.41	4.4	3.9
	90th%	1.58	1.93	1.8	3.67	2.39
Interference filters						
Targets		Timo	APT	Justin	CCSG	Verification Avg
ΔE_{00}	Avg	1.86	1.14	0.84	1.4	1.47
	Min	0.33	0.22	0.14	0.21	0.25
	Max	9.82	4.03	3.25	4.8	6.22
	90th%	3.34	1.88	1.68	2.94	2.72
RMSE	Avg	0.017	0.028	0.01	0.012	0.019
	Min	0.004	0.011	0.003	0.005	0.007
	Max	0.039	0.061	0.029	0.03	0.043
	90th%	0.03	0.054	0.016	0.019	0.034
Noise	Avg	1.22	1.5	1.34	1.75	1.49
	Min	0.38	0.41	0.34	0.41	0.4
	Max	6.26	6.76	8.6	7.16	6.72
	90th%	2.3	2.8	2.43	5.43	3.51
Patch Number		110	24	100	140	274

Tab. 6.4. – Results of the spectral and colorimetric reproduction and noise for the sandwich absorption and interference filters. Calibration target: CCSG. Verification targets: Timo, APT, and Justin.

Sandwich filters						
Targets		Timo	APT	Justin	CCSG	Verification avg
ΔE_{00}	Avg	1.44	0.98	1	1.17	1.14
	Min	0.24	0.48	0.14	0.06	0.29
	Max	6.16	3.37	6.55	6.11	5.36
	90th%	2.98	1.65	1.91	2.24	2.18
RMSE	Avg	0.022	0.038	0.02	0.009	0.026
	Min	0.003	0.007	0.004	0.002	0.005
	Max	0.053	0.079	0.046	0.035	0.059
	90th%	0.037	0.061	0.035	0.014	0.045
Noise	Avg	0.93	1.08	1.03	1.3	1.01
	Min	0.34	0.43	0.36	0.37	0.37
	Max	3.69	3.87	5.37	4.48	4.31
	90th%	1.55	2.02	1.83	3.84	1.8
Interference filters						
Targets		Timo	APT	Justin	CCSG	Verification Avg
ΔE_{00}	Avg	1.83	1.31	1.02	1.19	1.39
	Min	0.47	0.33	0.22	0.08	0.34
	Max	7.98	4.62	2.94	5.3	5.18
	90th%	3.24	2.4	2.02	2.51	2.56
RMSE	Avg	0.022	0.033	0.018	0.008	0.020
	Min	0.004	0.008	0.003	0.002	0.000
	Max	0.059	0.087	0.049	0.022	0.060
	90th%	0.038	0.054	0.034	0.013	0.040
Noise	Avg	1.29	1.56	1.38	1.84	1.41
	Min	0.39	0.43	0.34	0.43	0.39
	Max	7.62	7.02	9	7.57	7.88
	90th%	2.48	3.01	2.48	5.75	2.65
Patch Number		110	24	100	140	234

Tab. 6.5. – The average verification average results of the spectral and colorimetric reproduction and noise for the sandwich absorption and interference filters for different calibration targets. The combined metric $Q = 0.3 \times 100 \times RMSE + 0.3 \times \Delta E_{00} + 0.4 \times noise$.

Filter Set	Calibration Target	Timo	APT	Justin	CCSG	Avg
Sand.	ΔE_{00}	1.48	1.27	1.39	1.21	1.34
	RMSE	0.015	0.014	0.017	0.022	0.017
	Noise	1.15	1.23	1.11	0.98	1.12
	Q	1.36	1.30	1.36	1.43	1.36
Interf.	ΔE_{00}	1.73	1.46	1.56	1.43	1.55
	RMSE	0.014	0.013	0.016	0.021	0.016
	Noise	1.74	1.47	1.51	1.35	1.52
	Q	1.63	1.43	1.54	1.60	1.55

T-Test Results

To compare the performance of sandwich absorption filters and interference filters, a T-Test was used to evaluate the statistical significance of the conclusions[Student, 1908]. The metric of ΔE_{00} , spectral *RMSE*, and noise (mean color difference from the mean) as well as the combined metric Q (computed from Eq. 3.10) are tested.

A paired two-sample, one-tailed T-Test was performed. The statistic is

$$t = \frac{\overline{x - y}}{\sigma(x - y)/\sqrt{n}} \quad (6.12)$$

where x and y are pairs of data from two groups $\{x\}$ and $\{y\}$, and the mean value is calculated after the difference between each pair of samples is calculated; σ is the standard deviation of the paired sample difference, and n is the number of samples. This equation gives t , using which the p -value of the test can be obtained by looking up the Student's t Cumulative Distribution function at the degree of freedom $n - 1$, where n is the sample size.

The obtained p -value tests the null hypothesis of whether the pairs of samples x and y are from the same group. Given a significance level α ($\alpha = 0.05$ is commonly used), if $p \leq \alpha$, the null hypothesis is rejected, with the alternative hypothesis that the mean values of $\{x\}$ is larger than $\{y\}$.

The T-Test results are shown in Table 6.6. The numbers in the table are the mean of the difference between all the pairs of individually measured verification data. Each individually measured data point came from one patch of a verification target, while the data from the calibration targets used in each case was excluded. One pair of data points were from sandwich absorption filters and interference filters, respectively. The difference of each pair of data was calculated by using the data from the absorption filters minus the data from the interference filters; therefore the negative values in the table indicates

that the absorption filter has a lower mean values (lower ΔE_{00} , RMSE, noise, or Q). The corresponding T-Test p-values are shown in Table 6.7.

Whether the difference has statistical significance was tested by T-Test as follows: (1) First, the alternative hypothesis that the absorption filters had better performance (lower colorimetric error, RMSE, and noise) was being tested—the difference of a pair of data was obtained by the data from the interference filters minus that from the absorption filters—using Eq. 6.12. The significance level $\alpha = 0.05$ was used. Therefore if the obtained p -value was equal to or lower than α , the results from absorption filters had a significantly lower error than that from the interference filters. This significance is labeled by red color in the table. (2) Secondly, the alternative hypothesis that the interference filters had better performance (lower error) was being tested, and the significant results are labeled by green color in the table. The values that are neither red nor green have no statistical significance ($p > \alpha$) and no conclusion of whether one set of filters is better than the other should be drawn. It is very important to note that there is only one table of pairwise comparison mean difference table, since the values in the table are the differences of corresponding metric of the data groups between two filter sets. However, each cell's corresponding T-Test has two of them (Two one-sided T-Test discussed above). Since it is impossible to accept both of these two T-Test's alternative hypothesis, the labeling of red or green cells are combined into one table.

It is also worth noting that a T-Test between group A and B do **not** give the possibility of a single observation (one pair of samples) that shows the fact that the observation from sample group A is lower than the sample from group B. Instead, the T-Test gives the confidence level given two group of paired samples, whether they are indeed from two different groups, and whether the group mean of A is lower than group mean of B. For example, the p -value of Q for all verification data is 0.0000 (Table. 6.7), which shows the fact that based on the observation of paired sample of Q values from absorption filters

and interference filters, the mean Q value of absorption filters is indeed lower than that of the interference filters. To visualize the distribution of the pairwise difference of Q between two filter sets, a histogram and its fitting to normal distribution is shown in Fig. 6.9. It is shown that the mean value of the fitted normal distribution is smaller than zero, however the significance of this hypothesis must be tested by T-Test, which is not shown in this figure. On the other hand, this figure only visualizes the possibility of a single observation (the difference between a pair of samples from group A and B) is negative.

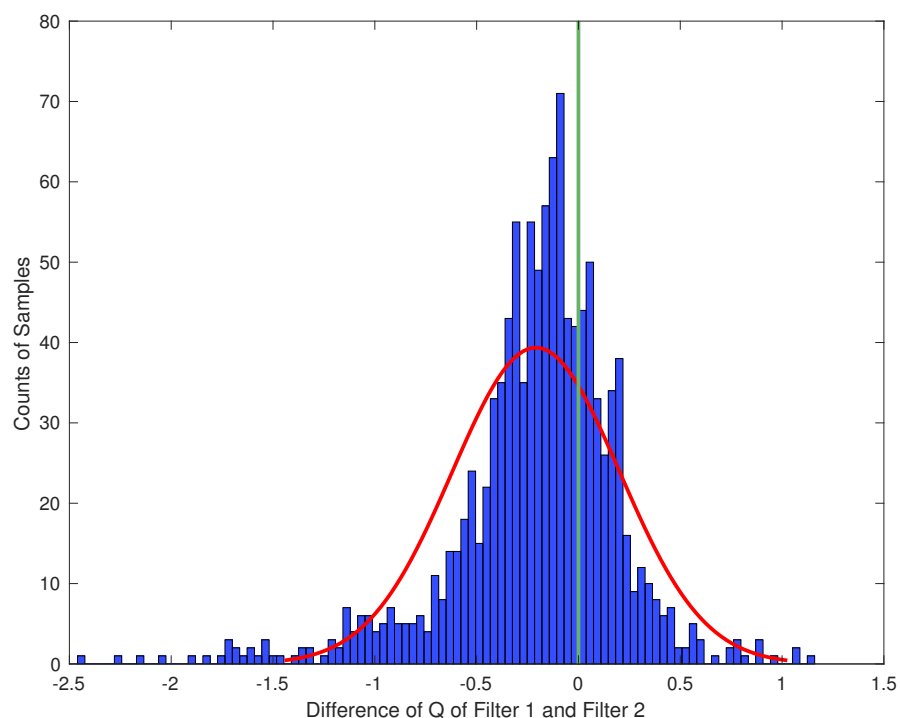


Fig. 6.9. – The distribution of the pairwise difference of Q metric between the absorption filters and interference filters among all verification patches (1122), and its fitting of a normal distribution.

Tab. 6.6. – The difference between the average verification data of the sandwich filters and interference filters. T-Test was applied on all verification data. Numbers in red color: the results of the absorption filters are significantly lower than that from the interference filters. Numbers in green color: the results of the interference filters are significantly lower than that from the absorption filters.

Calibration Target	Timo	APT	Justin	CCSG	All Verification
ΔE_{00}	-0.249	-0.331	-0.173	-0.225	-0.251
RMSE	0.0015	0.0005	0.0010	0.0014	0.0011
Noise	-0.589	-0.322	-0.399	-0.369	-0.413
Q	-0.266	-0.212	-0.180	-0.174	-0.209

Tab. 6.7. – T-Test p-Values. Numbers in red color: the results of the absorption filters are significantly lower than that from the interference filters. Numbers in green color: the results of the interference filters are significantly lower than that from the absorption filters.

Calibration Target	Timo	APT	Justin	CCSG	All Verification
ΔE_{00}	0.0000	0.0000	0.0004	0.0000	0.0000
RMSE	0.0173	0.0009	0.0016	0.0019	0.0000
Noise	0.0000	0.0000	0.0000	0.0000	0.0000
Q	0.0000	0.0000	0.0000	0.0000	0.0000

Discussion

The percentage mean differences of the results from sandwich absorption filters compared to that of the interference filters (calculated by the mean difference of the two filters divided by the results of the interference filters) are shown in Table. 6.8. The negative values in the table indicates the percentage of the improvements on the noise metrics brought by switching from interference filters to sandwich absorption filters.

Overall, the sandwich absorption filters generated smaller ΔE_{00} and lower noise compared to the interference filters. The improvements of sandwich absorption filter in terms of ΔE_{00} is 0.251 or 15.5%, and it is a stable improvement since it is verified by T-Test on 1122 verification data points. The noise (mean color difference (ΔE_{00}) from the mean) improvement is 0.413, which is

Tab. 6.8. – Percentage mean difference of the results of sandwich absorption filters compared to the interference filters

Calibration Target	Timo	APT	Justin	CCSG	All Verification
ΔE_{00}	-14.4%	-19.5%	-11.0%	-15.7%	-15.5%
RMSE	10.7%	4.1%	6.7%	6.6%	6.8%
Noise	-33.8%	-21.82%	-26.3%	-27.3%	-27.2%
Q	16.3%	-14.1%	-11.7%	-10.9%	-13.4%

very significant considering that the improvement compared to interference filters is 27.2%.

The sandwich absorption filters generates higher RMSE compared to the interference filters. However, the 90th percentile RMSE of the two sets of filters are identical, and the actual mean difference of RMSE between two filters is relatively small (e.g., 0.0011 for all verification data, and only 6.8% worse than interference filters), indicating that the sandwich absorption filters are reliable to be used for spectral estimation, and they have quite similar worst case performance.

The results of combined metric Q of the sandwich absorption filters are smaller than that of the interference filters by 13.4%, indicating that the sandwich absorption filters have better overall performance than the interference filters. All above conclusions are verified using T-Tests. The results of the order of the two sets of filters agree with the conclusion in Chapter 4. For sandwich filters, errors between the predicted and experimental data came from real experiments and the gluing procedure.

6.3.2 Evaluation of Calibration Targets

T-Test Results

To evaluate the colorimetric and spectral performance when using each of the four targets as the calibration target, another series of paired two-sample, one-tailed T-Tests were performed. For each T-Test, all individually measured data points (including data from both the one calibration and three verification targets) were compared in pairs between using “Timo”, “APT”, “Justin”, and “CCSG” as the calibration targets, therefore each case involves six pairs of comparisons and is summarized in one table.

For each pair of comparisons, two separate one-tailed T-Tests are performed. For example, to compare the results from using “Timo” and “APT” as calibration target, first the T-Test with the alternative hypothesis that “Timo” has lower results compared to “APT” is performed, and if the alternative hypothesis is accepted ($p\text{-value} < 0.05$), then the number in the corresponding cell (the difference between mean values of “Timo” and “APT” calibrated results) is labeled using red color (in this case, the reported number is negative in the table). Then similarly, the T-Test with the alternative hypothesis that “APT” has higher results compared to “APT” is performed, and if the alternative hypothesis is accepted ($p\text{-value} < 0.05$), then the numbers in the corresponding cell is labeled using green color. Note that although for brevity, only six numbers in each table are reported to show the difference using four calibration targets in pairs, there are actually 12 T-Tests performed for each table. The numbers that has neither green nor red color show that the difference has no significance and the results from the two groups using the corresponding calibration targets are statistically in the same group.

For example, Table 6.9 shows the T-Test results for the sandwich absorption filters. The mean difference values in the table is the difference between the target in the column header and the target in the row header. The significance

is shown in red or green text, indicating the significance of negative or positive difference, respectively. If the value in the column of “CCSG” and row of “Timo” is negative and in red text, “CCSG” as the calibration target has a lower error than using “Timo” as the calibration target.

The six cases when using each of the two filter sets, and three evaluation metrics, are listed in Table 6.9-6.14.

Tab. 6.9. – Calibration target ΔE_{00} t-test comparison for absorption filters.

The reported data are the difference between the column targets and the row targets (column-row). For negative mean values, the T-test examines whether the results from the column targets are significantly lower than that from the row targets, and the values with significance ($p\text{-value} < 0.05$) are labeled in red color; for positive mean values, the T-test examines whether the results from the row targets are significantly lower than that from the column targets, and the values with significance ($p\text{-value} < 0.05$) are labeled in green color.

	Timo	APT	Justin	CCSG
Timo	–	-0.05	-0.12	-0.18
APT	–	–	-0.07	-0.13
Justin	–	–	–	-0.06
CCSG	–	–	–	–

Tab. 6.10. – Calibration target RMSE t-test comparison for absorption filters. The reported data are the difference between the column targets and the row targets (column-row). For negative mean values, the T-test examines whether the results from the column targets are significantly lower than that from the row targets, and the values with significance (p -value < 0.05) are labeled in red color; for positive mean values, the T-test examines whether the results from the row targets are significantly lower than that from the column targets, and the values with significance (p -value < 0.05) are labeled in green color.

	Timo	APT	Justin	CCSG
Timo	–	0.0003	0.0004	0.0023
APT	–	–	0.0007	0.0026
Justin	–	–	–	0.0020
CCSG	–	–	–	–

Tab. 6.11. – Calibration target noise T-Test comparison for absorption filters. The reported data are the difference between the column targets and the row targets (column-row). For negative mean values, the T-Test examines whether the results from the column targets are significantly lower than that from the row targets, and the values with significance (p -value < 0.05) are labeled in red color; for positive mean values, the T-Test examines whether the results from the row targets are significantly lower than that from the column targets, and the values with significance (p -value < 0.05) are labeled in green color.

	Timo	APT	Justin	CCSG
Timo	–	0.06	0.00	0.02
APT	–	–	-0.06	-0.05
Justin	–	–	–	0.01
CCSG	–	–	–	–

Tab. 6.12. – Calibration target ΔE_{00} T-Test comparison for interference filters. The reported data are the difference between the column targets and the row targets (column-row). For negative mean values, the T-Test examines whether the results from the column targets are significantly lower than that from the row targets, and the values with significance (p -value < 0.05) are labeled in red color; for positive mean values, the T-Test examines whether the results from the row targets are significantly lower than that from the column targets, and the values with significance (p -value < 0.05) are labeled in green color.

	Timo	APT	Justin	CCSG
Timo	–	0.10	-0.18	-0.21
APT	–	–	-0.28	-0.30
Justin	–	–	–	-0.03
CCSG	–	–	–	–

Tab. 6.13. – Calibration target RMSE T-Test comparison for interference filters. The reported data are the difference between the column targets and the row targets (column-row). For negative mean values, the T-Test examines whether the results from the column targets are significantly lower than that from the row targets, and the values with significance (p -value < 0.05) are labeled in red color; for positive mean values, the T-Test examines whether the results from the row targets are significantly lower than that from the column targets, and the values with significance (p -value < 0.05) are labeled in green color.

	Timo	APT	Justin	CCSG
Timo	–	-0.0020	-0.0019	0.0000
APT	–	–	0.0002	0.0020
Justin	–	–	–	0.0019
CCSG	–	–	–	–

Tab. 6.14. – Calibration target noise T-Test comparison for interference filters.

The reported data are the difference between the column targets and the row targets (column-row). For negative mean values, the T-Test examines whether the results from the column targets are significantly lower than that from the row targets, and the values with significance (p -value < 0.05) are labeled in red color; for positive mean values, the T-Test examines whether the results from the row targets are significantly lower than that from the column targets, and the values with significance (p -value < 0.05) are labeled in green color.

	Timo	APT	Justin	CCSG
Timo	–	-0.16	-0.16	-0.09
APT	–	–	-0.01	0.06
Justin	–	–	–	0.07
CCSG	–	–	–	–

Discussion

Comparing the verification results of ΔE_{00} when using each of the four targets as the calibration target, for both absorption and interference filters, CCSG has the lowest ΔE_{00} ; target Justin generates the second lowest ΔE_{00} ; target APT's ΔE_{00} is higher than that of target Justin; target Timo has the highest ΔE_{00} (Table 6.5).

When using target APT as the calibration target, average ΔE_{00} is higher because of the under-sampled low chroma / lightness (dark) colors in target Timo and APT targets, while there are many more dark color patches in Justin and CCSG targets. The ΔE_{00} error for dark colors in these cases are mainly in the direction of lightness (Fig. 6.10). Using target Timo is the same case (Appendix B Fig. B.1).

When using Justin as calibration, ΔE_{00} is higher for high chroma color patches in all other three verification targets. This is especially significant in Timo target since it contains more high-chroma patches. (Appendix B Fig. B.1)

When using CCSG as calibration target, ΔE_{00} are generally lower because using other targets to calibrate, the dark colors have higher ΔE_{00} , and CCSG has many more dark colors, which will increase the mean verification ΔE_{00} largely. Also, the CCSG has many patches and is generally well sampled in CIELAB space. (Appendix B Fig. B.1)

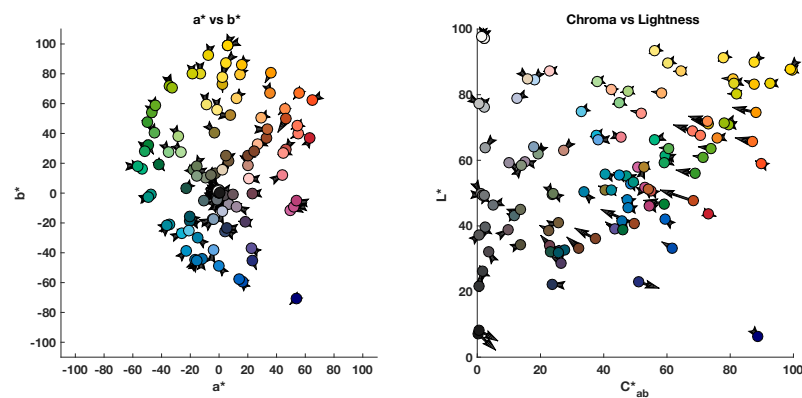
A normal-map image of the particular CCSG used in this research (Fig. 6.11) was taken by Roy S. Berns at a later time. It shows that some of the CCSG patches were curved (which are labeled with red circles), which was the main source of the verification errors when other targets were used for calibration.

When using Timo as the verification target, Samples 6J-K, 8G-K, 10-I, 10-K (row-column) generally have higher ΔE_{00} in all cases. This is probably due to

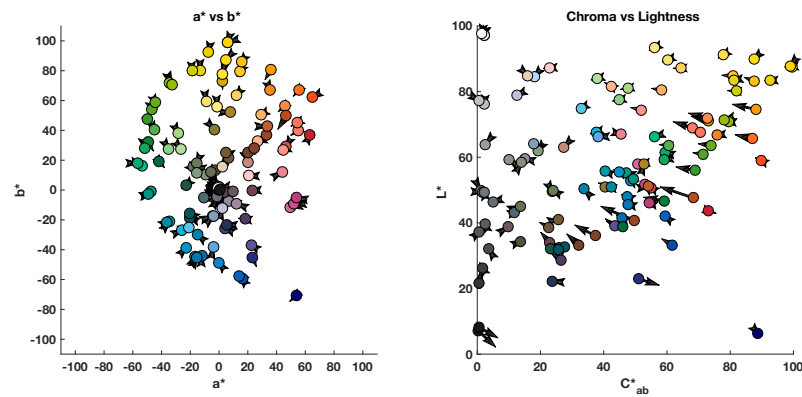
the absence of these color patches or similar patches in other targets to be used as calibration targets (Fig. 6.12).

Comparing the verification results of RMSE when using each of the four targets as the calibration targets, for both absorption and interference filters, CCSG has the highest RMSE; target Justin generates the second highest RMSE; target Timo's RMSE is higher than that of target APT; target APT has the lowest RMSE (Table 6.5).

For the middle wavelength range (500nm-620nm), the differences between the estimated and measured spectral reflectances of the absorption filters are lower than that of the interference filters. For the long ($>620\text{nm}$) and short



(a) Sandwich filters.



(b) Interference filters.

Fig. 6.10. – Colorimetric reproduction comparison for APT used as calibration target and the target Timo used as the verification target for the sandwich absorption filters and the interference filters.

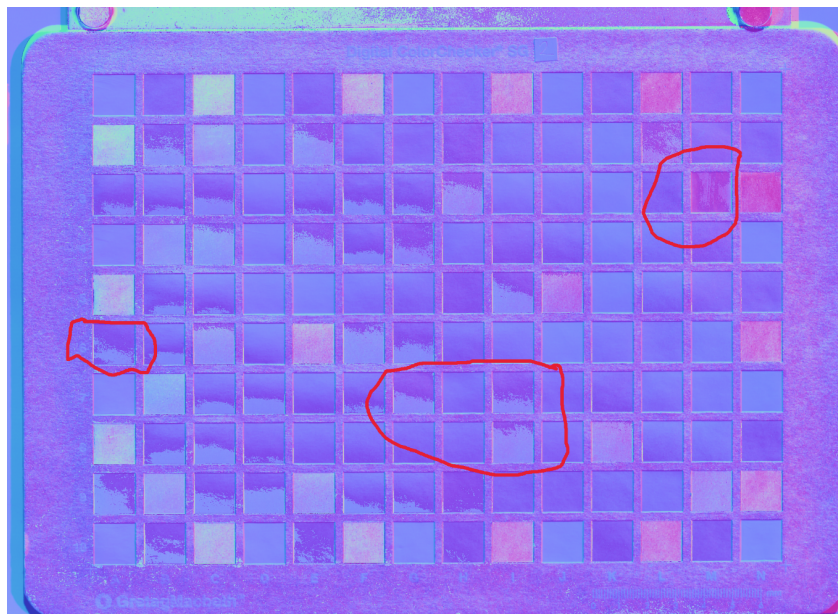


Fig. 6.11. – CCSG normal map. Curved patches are labeled with red circles.

(<500nm) wavelength ranges, the absorption filters generated more errors than the interference filters, especially near 650nm (Fig. 6.13).

When only CCSG was used as verification, the RMSE were higher for absorption filters in all four cases when using different targets as calibration targets (Tables 6.1, 6.2, 6.3, 6.4). For the other verification targets, the absorption filters outperformed or had no significant difference. Considering the fact that the CCSG patches are curved, the results from the other three targets might be more reliable than the CCSG results. Therefore, it's hard to tell which set of filters have better spectral performance based on the current data. A well-maintained CCSG target is needed to explore further.

According to the results above, there is a tradeoff between ΔE_{00} and RMSE. If the goal is to get both good ΔE_{00} and RMSE, APT is recommended since it has the smallest RMSE and the third smallest ΔE_{00} .

When the APT target is used for calibration, according to Table 6.2, the RMSE of the absorption and interference filters are almost identical. ΔE_{00} and noise of the absorption filters are much smaller than those of the interference filters. Comparing the verification results of ΔE_{00} , target Justin has the lowest ΔE_{00} ;

target Timo generates the second lowest ΔE_{00} ; target CCSG has the highest ΔE_{00} . Comparing the verification results of RMSE, target CCSG has the lowest RMSE; target Justin generates the second lowest RMSE; target Timo has the highest RMSE.

The colorimetric and spectral reproduction results (not including the CIELAB plots, which were already reported) of the two sets of filters for APT being used as the calibration targets and all four targets being used as the verification targets are reported in Appendix B (Fig. B.2- B.6).

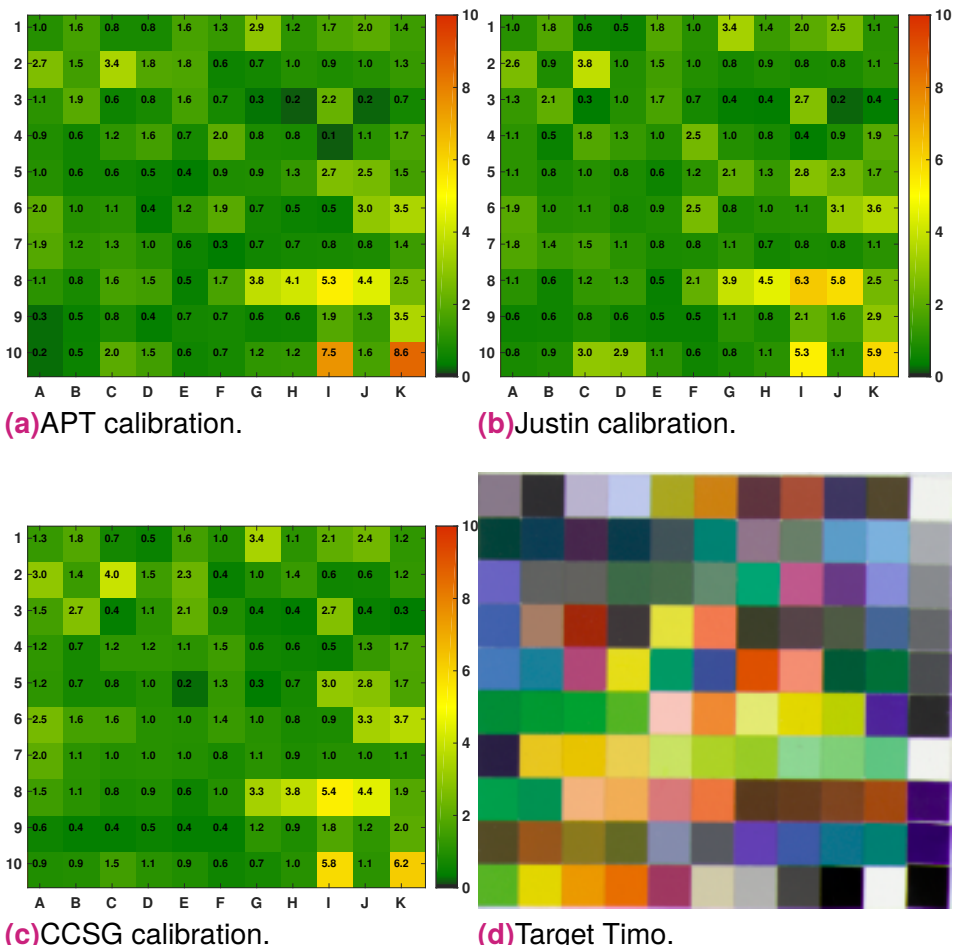
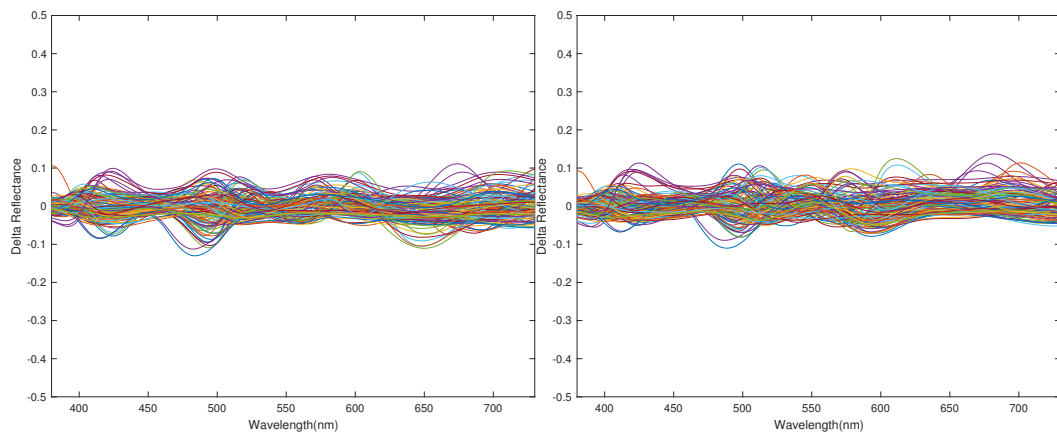


Fig. 6.12. – Colorimetric reproduction comparison for the target Timo used as the verification target for the sandwich absorption filters.



(a) Sandwich filters.

(b) Interference filters.

Fig. 6.13. – The discrepancy between the measured and reconstructed spectral reflectances for the two sets of filters for Target Timo. APT was used as the calibration target. The Target Timo was used as the verification target.

6.4 Conclusions

The spectral and colorimetric performance of the interference filters and the sandwich absorption filters were compared. Multi-channel images were taken and processed in two paths: colorimetric and spectral. For the colorimetric path, both ΔE_{00} and noise were considered in the color transformation matrix optimization. Four targets, Timo, APT, Justin and CCSG, were used for calibration. The spectral and colorimetric performance of the two sets of filters and four calibration targets were evaluated independently.

For the comparison of filter sets, the sandwich absorption filters had smaller ΔE_{00} and lower noise compared to the interference filters. A well-maintained CCSG target is needed for the spectral performance evaluation in the future.

Comparing the four targets as the calibration target, for verification average of ΔE_{00} , for both absorption and interference filters, CCSG had the lowest ΔE_{00} ; target Justin generated the second lowest ΔE_{00} ; target APT's ΔE_{00} was higher than that of target Justin; target Timo had the highest ΔE_{00} . For verification average of RMSE, for both absorption and interference filters, CCSG had the highest RMSE; target Justin generated the second highest RMSE; target Timo's RMSE was higher than that of target APT; target APT had the lowest RMSE. Considering both ΔE_{00} and RMSE results, APT target is recommended since it has the smallest RMSE and the third smallest ΔE_{00} .

Conclusions and Future Work

7.1 Conclusions

In this thesis, a novel filter selection technique was introduced and evaluated. According to the simulation results, the technique led to a noticeable improvement for efficiency, image quality and colorimetric accuracy compared to traditional filter selection methods. Filters were purchased based on the filter selection results. A wide band multispectral camera was constructed. According to the experimental results, the novel imaging system achieved high spectral and color accuracy as well as low color noise. Four calibration targets were evaluated as well. Each step was studied and verified in detail. The novel filter selection technique, the imaging system and the evaluation results of the calibration targets will be an important addition to spectral capabilities at MCSL.

The color transformation noise propagation model was examined at first. The color reproduction and noise due to color transformation were assessed by introducing a Gaussian modeling method for RGB- and CMY- type filter sets. Optimization was performed to determine the spectral sensitivity of the filter sets that yielded the smallest ΔE_{00} , the lowest colorimetric noise, or a compromise of the two goals. It was shown that for longer peak wavelengths, there was a trade-off between color accuracy and noise. A trend of how color difference and noise changes among all combinations of peak wavelengths and bandwidths was explored. This aspect of the research played a critical role in our effort to understanding what the trade-offs and restrictions of a filter selection technique would have.

Based on these results, a novel optimization based method to select filters for a multispectral camera system was introduced. A seven-channel bandpass filter set was modeled by a theoretical Gaussian filter set, and the performance of the theoretical filter set was modeled by a cost function. Then, the performance of the theoretical filter set was automatically optimized by adjusting bandwidths and central wavelengths of the filter set to minimize the cost function, with the goal to yield high spectral and colorimetric reproduction accuracy as well as low colorimetric noise. This step also gives users the flexibility to adjust the cost function for different applications.

The optimized theoretical Gaussian filters were used for filter selection. Sandwich absorption filters having the most similar spectral transmittance as the theoretical Gaussian filters were selected. Absorption filters were chosen over interference filters since the spectral sensitivity of interference filters varies across the image plane, leading to wavelength-dependent spatial non-uniformities. Another filter selection method was to select the sandwich filters whose peak wavelengths were equally spaced across the spectrum of interest. Instead of trying to calculate corresponding metric values for all possible combinations (4.3×10^{10}) of filters, which was not practical when non-linear optimization was applied, this method reduced the computing time by reducing the candidate filter combinations to 1.8×10^6 . This was a constrained “brute-force” approach. Selecting filters best matching the theoretical Gaussian filters resulted in noticeable improvement in noise and colorimetric performance. Constraining candidates to specific wavelength regions did not result in optimal performance. This novel technique provides better insight for filter selection in multi-spectral camera design.

Single absorption filters were selected using the same theory and models. The spectral and colorimetric reproduction of the selected single filter set was accurate. However, although the signal-to-noise ratio of absorption long-pass filters was high, the propagated noise was high because of the large spectral overlap between the filters, as predicted by the noise propagation model used

in this research. This work could be considered as evidence that the noise propagation model matches the experimental data.

The sandwich absorption filter set and a set of legacy interference filters were used to build a multispectral camera. Spectral images were taken and processed in two paths: colorimetric and spectral. For the colorimetric path, both ΔE_{00} and noise were considered in the color transformation matrix optimization. Four targets: Timo, APT, Justin and CCSG were used for calibration. The spectral and colorimetric performance of the two sets of filters and four calibration targets were verified independently.

For filter comparison, the sandwich absorption filters revealed significantly superior colorimetric and noise performance compared with the interference filters. Also, it showed reasonable spectral accuracy, although significantly poorer than the interference filters. Because of the limitations of field of view for interference filters and the requirement of high color accuracy in museum imaging, the absorption filters are recommended for use in a seven-channel multispectral camera.

Four targets were compared as calibration targets. For verification average of ΔE_{00} , for both absorption and interference filters, CCSG had the lowest ΔE_{00} ; target Justin generated the second lowest ΔE_{00} ; target APT's ΔE_{00} was higher than that of target Justin; target Timo had the highest ΔE_{00} . For verification average of RMSE, for both absorption and interference filters, CCSG had the highest RMSE; target Justin generated the second highest RMSE; target Timo's RMSE was higher than that of target APT; target APT had the lowest RMSE. Considering both ΔE_{00} and RMSE results, APT target is recommended since it has the smallest RMSE and the third smallest ΔE_{00} . The target evaluation work will provide insights for calibration target selection for a multispectral imaging workflow.

7.2 Future Work

The proposed filter selection technique and imaging system provided a novel alternative workflow for museum archiving. Future research for the following areas is suggested:

- The spectral reproduction could be explored for more improvement, especially in UV and NIR. The sandwich absorption filters in these two regions could be refined further.
- More combinations of weights on ΔE_{00} , RMSE and noise for the cost function of the theoretical Gaussian filters can be explored to generate other candidate filter sets for different applications, with experimental verification.
- The colorimetric path could be further explored omitting the shortest and longest wavelength sensitivity channels, since it was proved by the Dual-RGB camera design that five channels are enough to generate high colorimetric accuracy. A reduction in the number of filters may lead to improved color noise and registration. Depending on the particular lens, sharpness may be improved.
- The design of calibration targets can be explored based on the pros and cons analysis of the current targets.
- The image processing procedure can be explored by carefully examining the pixel mis-registration and distortion resulting from the different chromatic aberration behavior of the filters, and selecting spatial transformation algorithms.

References

[Abed, 2014]

Abed, Farhad Moghreh (2014). "Pigment Identification of Paintings Based on Kubelka–Munk Theory and Spectral Images". PhD thesis. Rochester Institute of Technology (Cited on pages 2, 9, 12, 15, 16).

[Antonioli et al., 2004]

Antonioli, Gianni et al. (2004). "Spectrophotometric scanner for imaging of paintings and other works of art". In: *Conference on Colour in Graphics, Imaging, and Vision*. Vol. 2004. 1. Society for Imaging Science and Technology, pp. 219–224 (Cited on page 6).

[Barnard and Funt, 2002]

Barnard, Kobus and Brian Funt (2002). "Camera characterization for color research". In: *COLOR research and application* 27.3, pp. 153–164 (Cited on page 18).

[Berns, Taplin, and Nezamabadi, 2004]

Berns, Roy, Lawrence Taplin, and Mahdi Nezamabadi (2004). *Modifications of a sinarback 54 digital camera for spectral and high-accuracy colorimetric imaging: Simulations and experiments*. Tech. rep. Art-SI.org (Art Spectral Imaging), Rochester Institute of Technology (Cited on page 12).

[Berns et al., 2005]

Berns, Roy et al. (2005). "Spectral imaging using a commercial colour-filter array digital camera". In: *The Fourteenth Triennial Meeting of The Conservation Committee of the International Council of Museums (ICOM-CC)*, pp. 743–750 (Cited on page 12).

[Berns, 2005]

Berns, Roy S (2005). "Color-accurate image archives using spectral imaging". In: *Proceedings of the National Academy of Sciences: (Sackler NAS Colloquium) Scientific Examination of Art: Modern Techniques in Conservation and Analysis*. Vol. 12. National Academies Press, pp. 105–119 (Cited on page 4).

[Berns, Cox, and Abed, 2015]

Berns, Roy S., Brittany D. Cox, and Farhad Moghareh Abed (2015). "Wavelength-dependent spatial correction and spectral calibration of a liquid crystal tunable filter imaging system". In: *Applied Optics* 54.12, pp. 3687–3693 (Cited on pages 9, 18).

[Bianco et al., 2011]

Bianco, Simone et al. (2011). "Digital Imaging for Cultural Heritage Preservation". In: ed. by Filippo Stanco, Sebastiano Battiato, and Giovanni Gallo. Boca Raton: CRC Press–Taylor & Francis. Chap. Applications of spectral imaging and reproduction to cultural heritage, pp. 183–209 (Cited on pages 8, 10).

[Brauers, Schulte, and Aach, 2008]

Brauers, Johannes, Nils Schulte, and Til Aach (2008). "Multispectral filter-wheel cameras: Geometric distortion model and compensation algorithms". In: *Image Processing, IEEE Transactions on* 17.12, pp. 2368–2380 (Cited on page 8).

[Brusco et al., 2006]

Brusco, Nicola et al. (2006). "A system for 3D modeling frescoed historical buildings with multispectral texture information". In: *Machine Vision and Applications* 17.6, pp. 373–393 (Cited on page 6).

[Burns, 1997]

Burns, Peter D. (1997). "Analysis of image noise in multispectral color acquisition". PhD thesis. Rochester Institute of Technology (Cited on pages 2, 3, 16, 17, 69).

[Burns and Berns, 1997]

Burns, Peter D and Roy S Berns (1997). "Error propagation analysis in color measurement and imaging". In: *Color Research & Application* 22.4, pp. 280–289 (Cited on page 20).

[Cheung et al., 2004]

Cheung, Vien et al. (2004). "A comparative study of the characterisation of colour cameras by means of neural networks and polynomial transforms". In: *Coloration technology* 120.1, pp. 19–25 (Cited on page 18).

[Day, 2003]

Day, David C (2003). "Filter Selection for Spectral Estimation Using a Trichromatic Camera". MA thesis. Rochester Institute of Technology (Cited on page 9).

[Fischer and Kakoulli, 2006]

Fischer, Christian and Ioanna Kakoulli (2006). "Multispectral and hyperspectral imaging technologies in conservation: current research and potential applications". In: *Studies in Conservation* 51. Supplement-1, pp. 3–16 (Cited on pages 4, 8, 10).

[Fukuda et al., 2005]

Fukuda, Hiroyuki et al. (2005). "Development of a 16-band multispectral image archiving system". In: *Electronic Imaging 2005*. International Society for Optics and Photonics, pp. 136–145 (Cited on page 8).

[Gat, 2000]

Gat, Nahum (2000). "Imaging spectroscopy using tunable filters: a review". In: *AeroSense 2000*. International Society for Optics and Photonics, pp. 50–64 (Cited on page 8).

[Geladi, Grahn, and Burger, 2007]

Geladi, P., H. Grahn, and J. Burger (2007). "Multivariate images, hyperspectral imaging: background and equipment". In: *Techniques and Applications of Hyperspectral Image Analysis*, pp. 1–15 (Cited on page 5).

[Gow et al., 2007]

Gow, R.D. D. et al. (2007). "A Comprehensive Tool for Modeling CMOS Image-Sensor-Noise Performance". In: *IEEE Trans. Electron Devices* 54.6, pp. 1321–1329 (Cited on page 19).

[Green and MacDonald, 2011]

Green, Phil and Lindsay MacDonald (2011). *Colour engineering: achieving device independent colour*. Vol. 30. John Wiley & Sons (Cited on page 18).

[Guizar-Sicairos, Thurman, and Fienup, 2008]

Guizar-Sicairos, Manuel, Samuel T. Thurman, and James R. Fienup (2008). "Efficient subpixel image registration algorithms". In: *Optics letters* 33.2, pp. 156–158 (Cited on page 77).

[Haneishi et al., 2000]

Haneishi, Hideaki et al. (2000). "System design for accurately estimating the spectral reflectance of art paintings". In: *Applied Optics* 39.35, pp. 6621–6632 (Cited on page 14).

[Hardeberg, 2001]

Hardeberg, Jon Y (2001). *Acquisition and reproduction of color images: colorimetric and multispectral approaches*. Boca Raton: Dissertation.com–Universal-Publishers (Cited on pages 14, 16).

[Hegyi and Martini, 2015]

Hegyi, Alex and Joerg Martini (2015). "Hyperspectral imaging with a liquid crystal polarization interferometer". In: *Optics express* 23.22, pp. 28742–28754 (Cited on pages 6, 7).

[Hensley and Wyble, 2012]

Hensley, Brittany and David Wyble (2012). "Spectral imaging using a liquid crystal tunable filter". In: *Munsell Color Science Laboratory Technical Report* (Cited on pages 8, 9).

[Hong, Luo, and Rhodes, 2001]

Hong, Guowei, M. Ronnier Luo, and Peter A. Rhodes (2001). "A study of digital camera colorimetric characterisation based on polynomial modelling". In: (Cited on page 18).

[Imai, Taplin, and Day, 2002]

Imai, Francisco, Lawrence Taplin, and Ellen Day (2002). *Comparison of the accuracy of various transformations from multi-band images to reflectance spectra*. Tech. rep. Art-SI.org (Art Spectral Imaging), Rochester Institute of Technology (Cited on page 8).

[Imai, Rosen, and Berns, 2000]

Imai, Francisco H., Mitchell R. Rosen, and Roy S. Berns (2000). "Comparison of spectrally narrow-band capture versus wide-band with a priori sample analysis for spectral reflectance estimation". In: *Color and Imaging Conference*. Vol. 2000. 1. Society for Imaging Science and Technology, pp. 234–241 (Cited on page 9).

[Kaye, 1983]

Kaye, Wilbur I (1983). *Liquid crystal tuned birefringent filter*. US Patent 4,394,069 (Cited on page 8).

[Kuniba and Berns, 2008]

Kuniba, Hideyasu and Roy S. Berns (2008). "The trade-off between color reproduction accuracy and image sensor noise". In: *Color and Imaging Conference*. Vol. 2008. 1. Society for Imaging Science and Technology, pp. 232–237 (Cited on page 32).

[Kuniba and Berns, 2009]

Kuniba, Hideyasu and Roy S Berns (2009). "Spectral sensitivity optimization of color image sensors considering photon shot noise". In: *Journal of Electronic Imaging* 18.2, pp. 023002–023002 (Cited on pages 23, 24, 27, 30, 38).

[Liang, 2012]

Liang, Haida (2012). "Advances in multispectral and hyperspectral imaging for archaeology and art conservation". In: *Applied Physics A* 106.2, pp. 309–323 (Cited on pages 4, 18).

[Liang, Saunders, and Cupitt, 2005]

Liang, Haida, David Saunders, and John Cupitt (2005). "A new multispectral imaging system for examining paintings". In: *Journal of Imaging Science and Technology* 49.6, pp. 551–562 (Cited on page 18).

[MacDonald et al., 2013]

MacDonald, Lindsay et al. (2013). "Multispectral imaging of degraded parchment". In: *Computational Color Imaging*. Berlin Heidelberg: Springer, pp. 143–157 (Cited on page 8).

[MacDonald, 2006]

MacDonald, Lindsay W (2006). *Digital heritage: applying digital imaging to cultural heritage*. Butterworth-Heinemann–Elsevier (Cited on pages 4, 8, 10).

[Martinez et al., 2002]

Martinez, Kirk et al. (2002). "Ten years of art imaging research". In: *Proceedings of the IEEE* 90.1, pp. 28–41 (Cited on pages 10, 11).

[Novati, Pellegrini, and Schettini, 2005]

Novati, Gianluca, Paolo Pellegrini, and Raimondo Schettini (2005). "An affordable multispectral imaging system for the digital museum". In: *International Journal on Digital Libraries* 5.3, pp. 167–178 (Cited on pages 6, 8).

[Nyström, 2007]

Nyström, Daniel (2007). "Colorimetric and multispectral image acquisition using model-based and empirical device characterization". In: *Image Analysis*. Springer, pp. 798–807 (Cited on page 18).

[Ribes and Schmitt, 2008]

Ribes, Alejandro and Francis Schmitt (2008). "Linear inverse problems in imaging". In: *Signal Processing Magazine, IEEE* 25.4, pp. 84–99 (Cited on pages 14, 16).

[Ribés et al., 2005]

Ribés, Alejandro et al. (2005). "Calibration and spectral reconstruction for crisatel: an art painting multispectral acquisition system". In: *Journal of Imaging Science and Technology* 49.6, pp. 563–573 (Cited on page 18).

[Ribes et al., 2008]

Ribes, Alejandro et al. (2008). "Studying that smile". In: *Signal Processing Magazine, IEEE* 25.4, pp. 14–26 (Cited on page 14).

[Schmitt, Brettel, and Hardeberg, 1999]

Schmitt, Francis, Hans Brettel, and Jon Yngve Hardeberg (1999). "Multi-spectral imaging development at ENST". In: *International symposium on multispectral imaging and color reproduction for digital archives*, pp. 50–58 (Cited on pages 10, 14).

[Sharma and Bala, 2002]

Sharma, Gaurav and Raja Bala (2002). *Digital color imaging handbook*. CRC press (Cited on pages 17, 18, 78).

[Student, 1908]

Student (1908). "The probable error of a mean". In: *Biometrika*, pp. 1–25 (Cited on page 87).

[Sun, 2010]

Sun, Da-Wen (2010). *Hyperspectral imaging for food quality analysis and control*. London: Academic Press–Elsevier (Cited on page 6).

[Swinehart, 1962]

Swinehart, D. F. (1962). "The beer-lambert law". In: *Journal of chemical education* 39.7, p. 333 (Cited on page 40).

[Taplin and Berns, 2005]

Taplin, Lawrence and Roy Berns (2005). "Practical spectral capture systems for museum imaging". In: *Association Internationale de la Couleur (AIC)-International Color Association* (Cited on pages 10, 12).

[Tominaga, Tanaka, and Komada, 2004]

Tominaga, Shoji, Norihiro Tanaka, and Takayuki Komada (2004). "Imaging and rendering of oil paintings using a multi-band camera". In: *Image Analysis and Interpretation, 2004. 6th IEEE Southwest Symposium on*. IEEE, pp. 6–10 (Cited on page 8).

[Vora and Trussell, 1993]

Vora, Poorvi L. and H. Joel Trussell (1993). "Measure of goodness of a set of color-scanning filters". In: *JOSA A* 10.7, pp. 1499–1508 (Cited on page 36).

[Yamaguchi et al., 2001]

Yamaguchi, Masahiro et al. (2001). "Color image reproduction based on multispectral and multiprimary imaging: experimental evaluation". In: *Electronic Imaging 2002*. International Society for Optics and Photonics, pp. 15–26 (Cited on page 8).

[Zhao and Berns, 2007]

Zhao, Yonghui and Roy S Berns (2007). "Image-based spectral reflectance reconstruction using the matrix R method". In: *Color Research & Application* 32.5, pp. 343–351 (Cited on pages 12, 77).

[Zhao, Taplin, and Nezamabadi, 2005]

Zhao, Yonghui, Lawrence Taplin, and Mahdi Nezamabadi (2005). "Using the matrix R method for spectral image archives". In: *Association Internationale de la Couleur (AIC)-International Color Association* (Cited on pages 12, 77).

Appendix A: Specific filter sets selected in Chapter 4

Tab. A.1. – Schott B.

Filter 1	Filter 2
BG 60	UG 5
450nm intfc	
GG 475	S 8022
BG 61	OG 530
BG 40	OG 570
BG 64	RG 610
KG 1	UG 5

Tab. A.2. – Andover A.

Filter 1	Filter 2
BG 25	BG 25
BG 12	GG 420
BG 23	GG 495
OG 530	S 8612
BG 40	OG 570
KG 5	OG 590
KG 3	RG 665

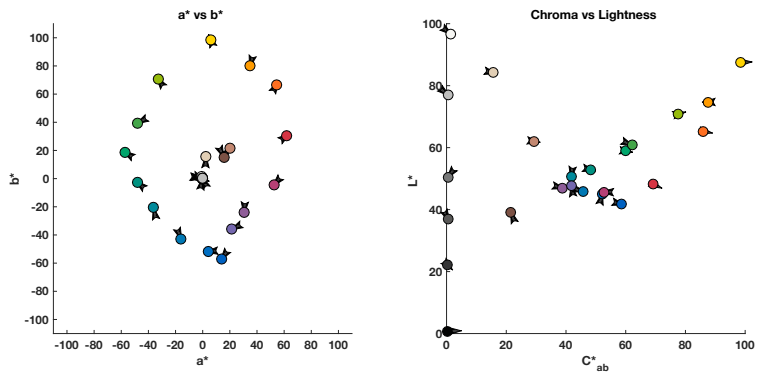
Tab. A.3. – Schott D.

Filter 1	Filter 2
BG 3	KG 5
BG 18	BG 25
GG 475	S 8022
BG 61	OG 530
BG 40	OG 570
BG 64	RG 610
KG 3	RG 665

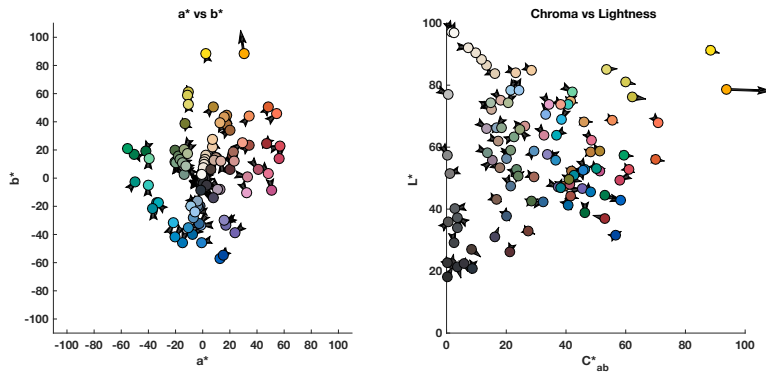
Tab. A.4. – Andover C.

Filter 1	Filter 2
BG 25	BG 25
BG 12	GG 420
BG 23	GG 495
OG 530	S 8612
BG 40	OG 570
BG 38	OG 590
KG 3	RG 665

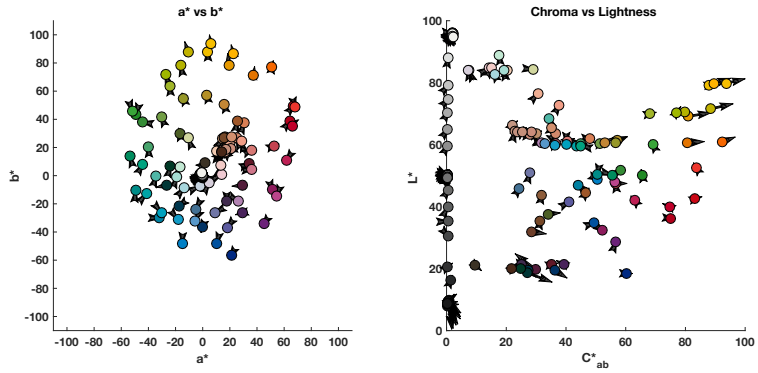
Appendix B: Spectral and colorimetric reproduction plots for Chapter 6



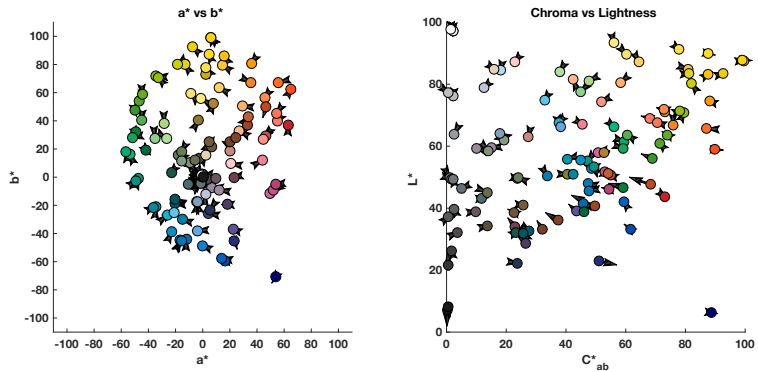
(a) Timo calibration. APT verification.



(b) Timo calibration. Justin verification.

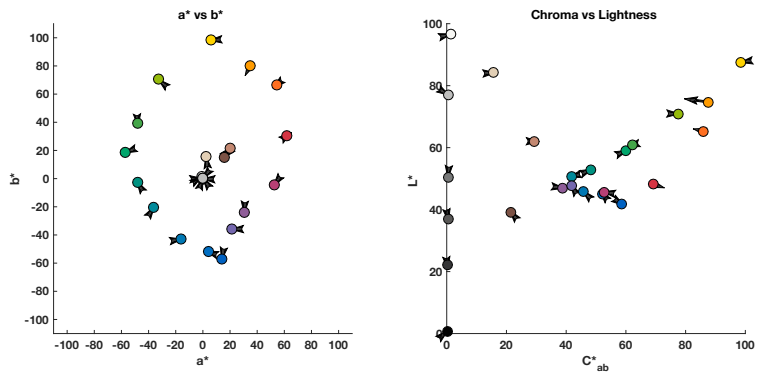


(c) Timo calibration. CCGS verification.

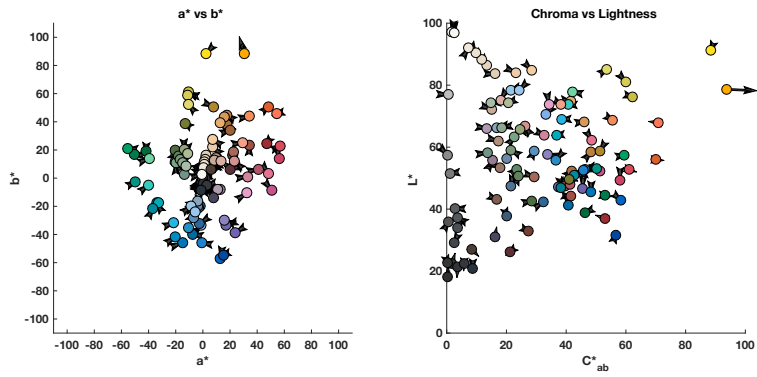


(d) Timo calibration. Timo verification.

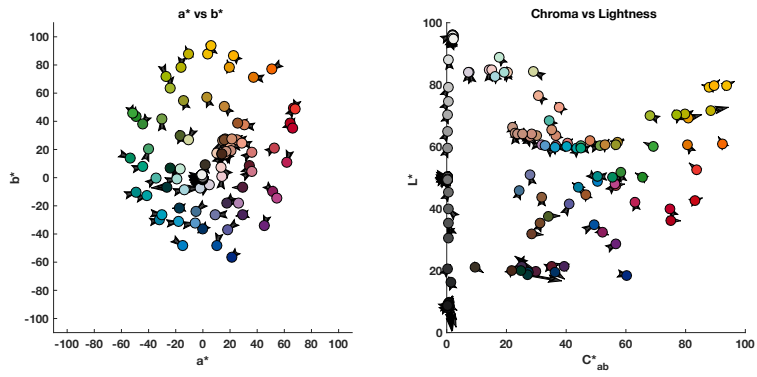
Fig. B.1. – Colorimetric reproduction comparison for the four targets used as the calibration targets for the sandwich absorption filters.



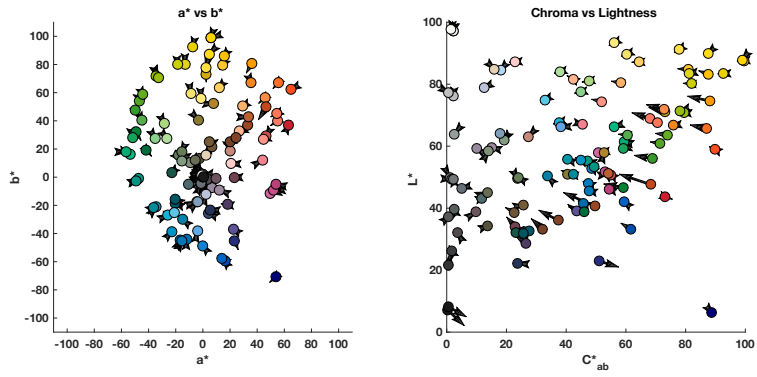
(e) APT calibration. APT verification.



(f) APT calibration. Justin verification.

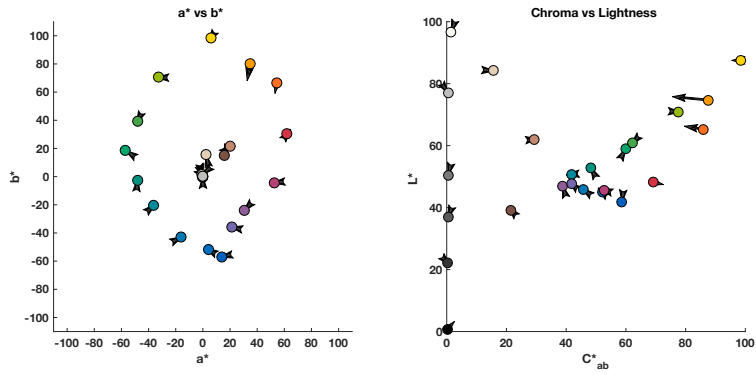


(g) APT calibration. CCSG verification.

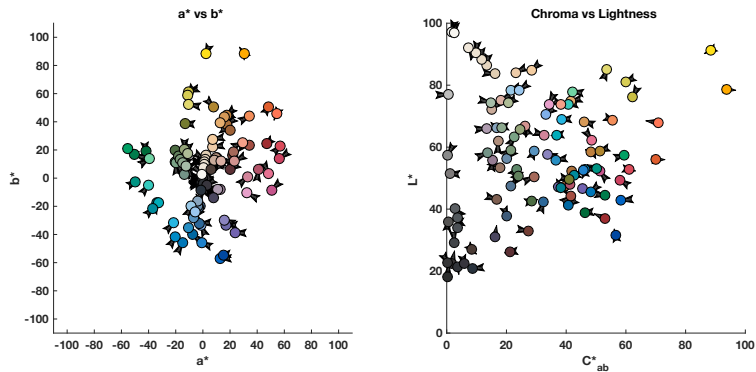


(h) APT calibration. Timo verification.

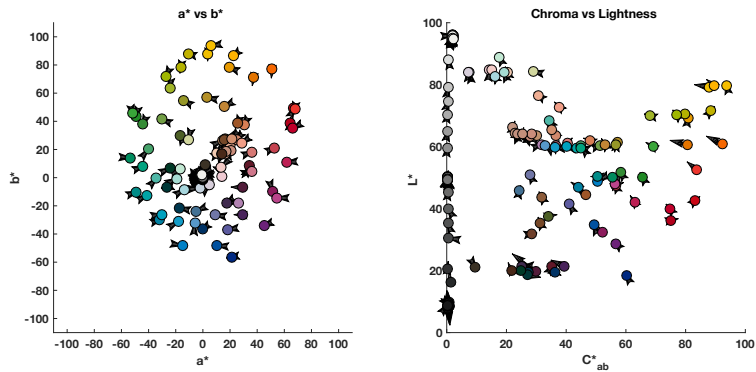
Fig. B.1. – Colorimetric reproduction comparison for the four targets used as the calibration targets for the sandwich absorption filters.



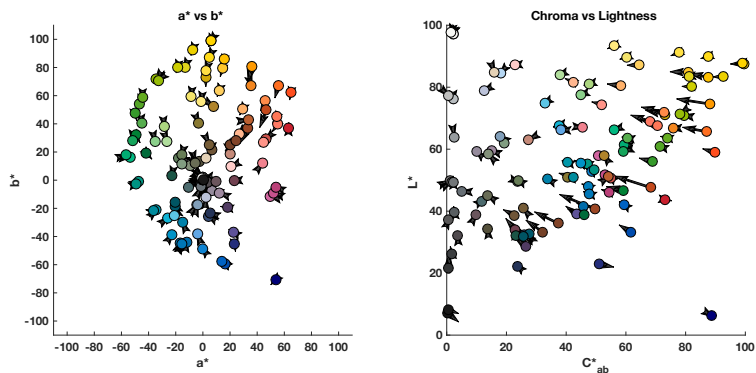
(i) Justin calibration. APT verification.



(j) Justin calibration. Justin verification.

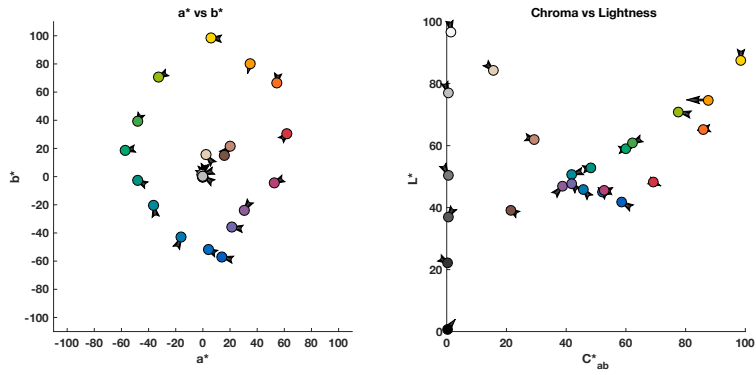


(k) Justin calibration. CCSG verification.

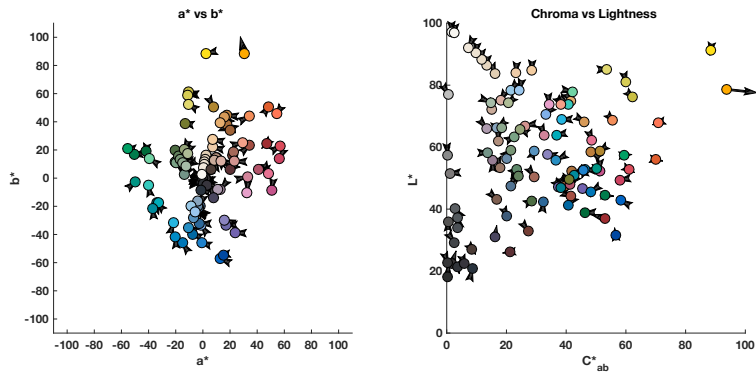


(l) Justin calibration. Timo verification.

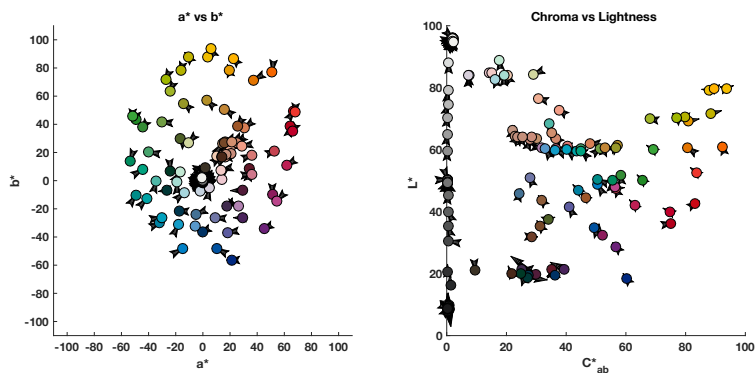
Fig. B.1. – Colorimetric reproduction comparison for the four targets used as the calibration targets for the sandwich absorption filters.



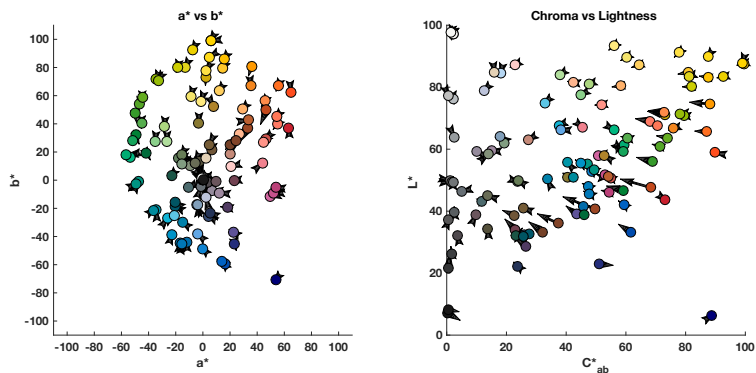
(m) CCSG calibration. APT verification.



(n) CCSG calibration. Justin verification.

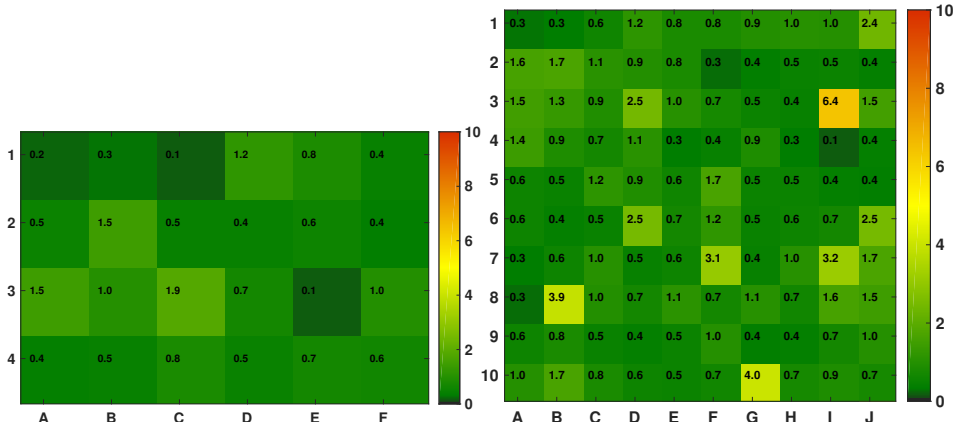


(o) CCSG calibration. CCSG verification.

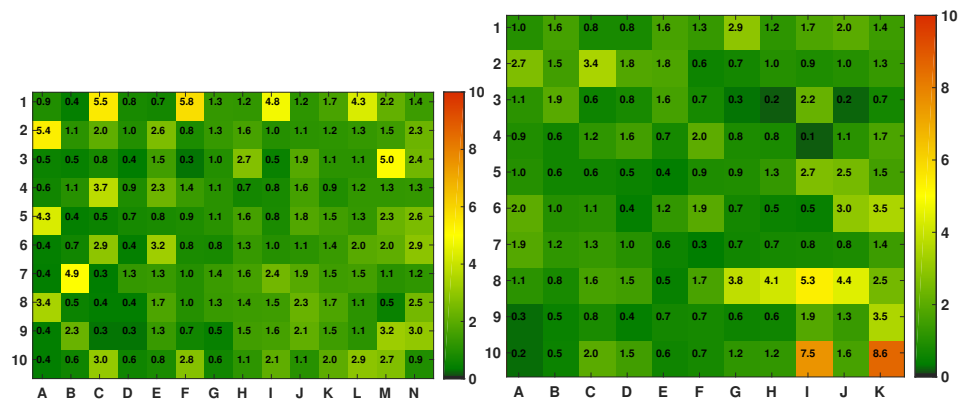


(p) CCSG calibration. Timo verification.

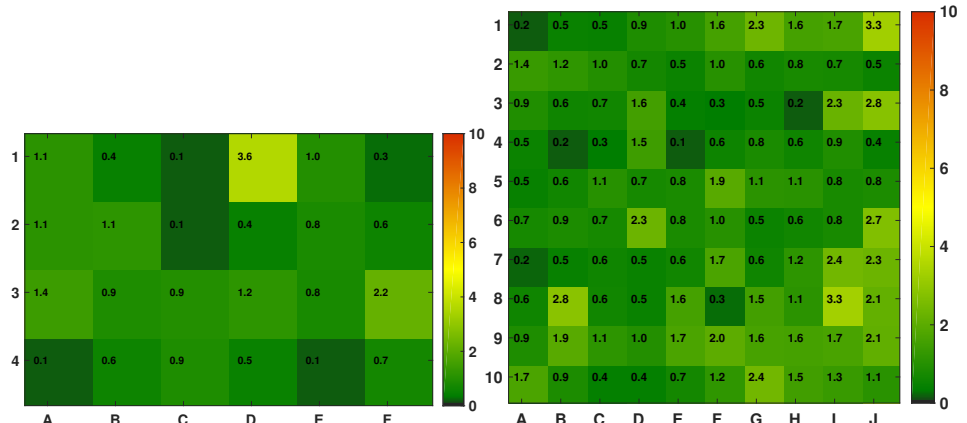
Fig. B.1. – Colorimetric reproduction comparison for the four targets used as the calibration targets for the sandwich absorption filters.



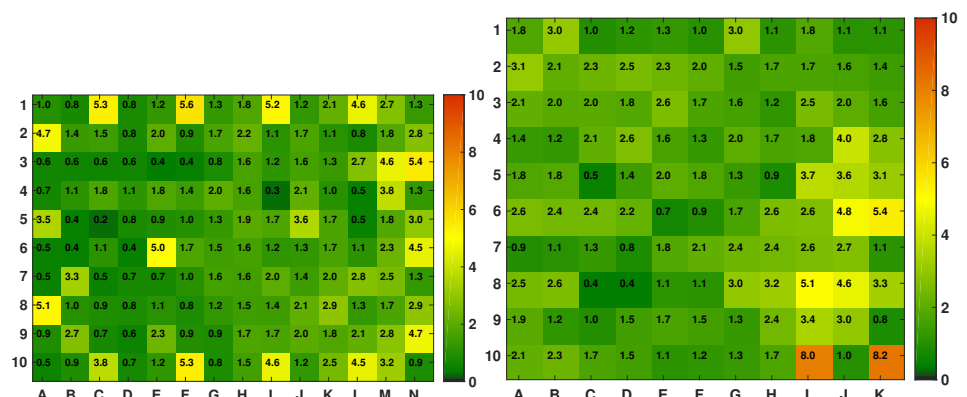
(a) Absorption filter APT verification. (b) Absorption filter Justin verification.



(c) Absorption filter CCSG verification. (d) Absorption filter Timo verification.

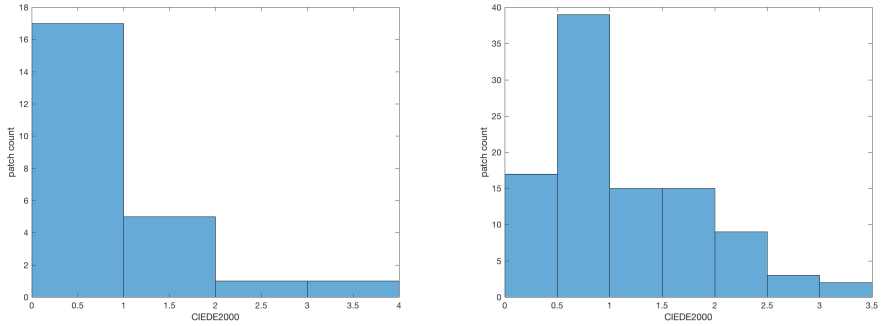


(e) Interference filter APT verification. (f) Interference filter Justin verification.

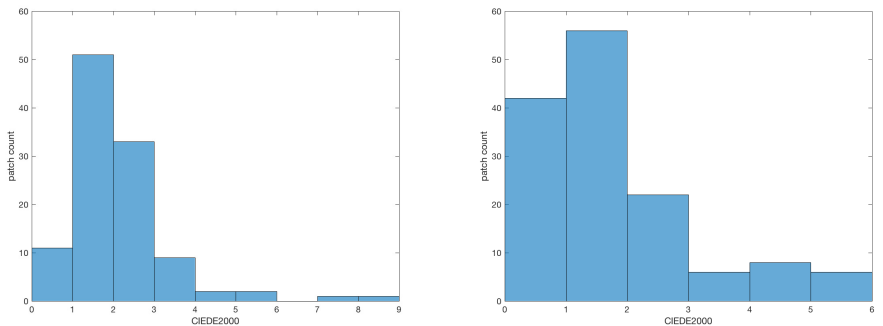


(g) Interference filter CCSG verification. (h) Interference filter APT verification.

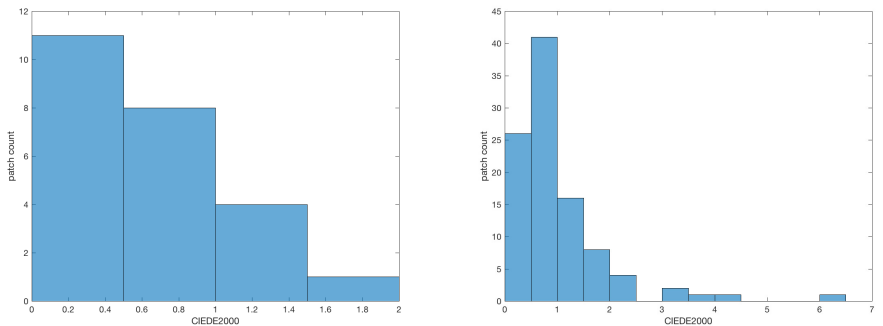
Fig. B.2. – ΔE_{00} for APT calibration.



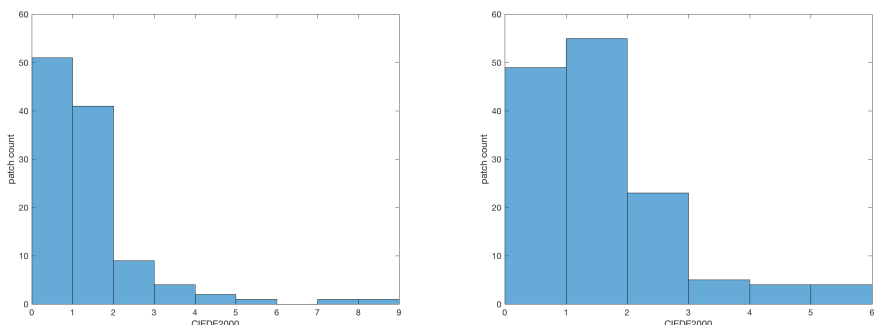
(a) Absorption filter APT verification. (b) Absorption filter Justin verification.



(c) Absorption filter Timo verification. (d) Absorption filter CCSG verification.

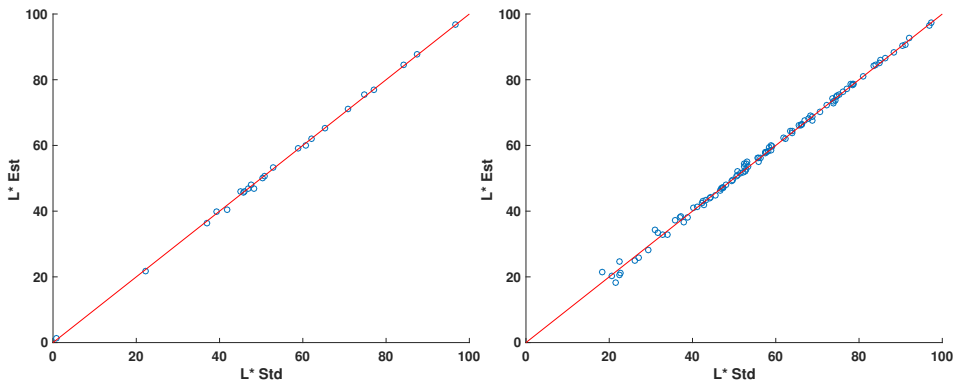


(e) Interference filter APT verification. (f) Interference filter Justin verification.

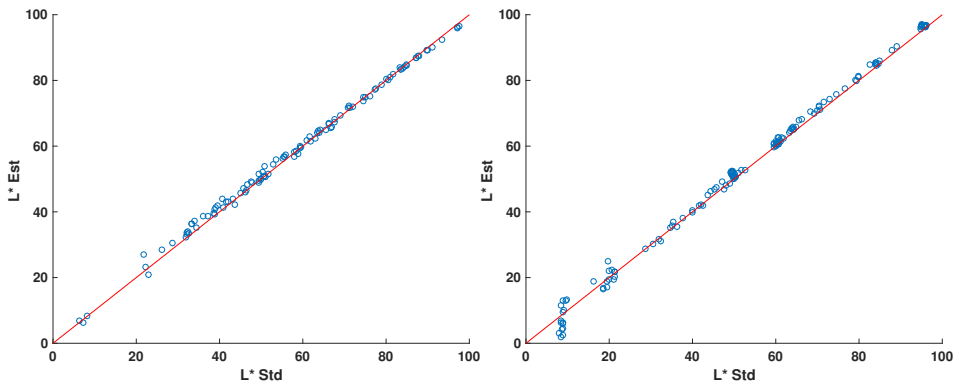


(g) Interference filter Timo verification. (h) Interference filter CCSG verification.

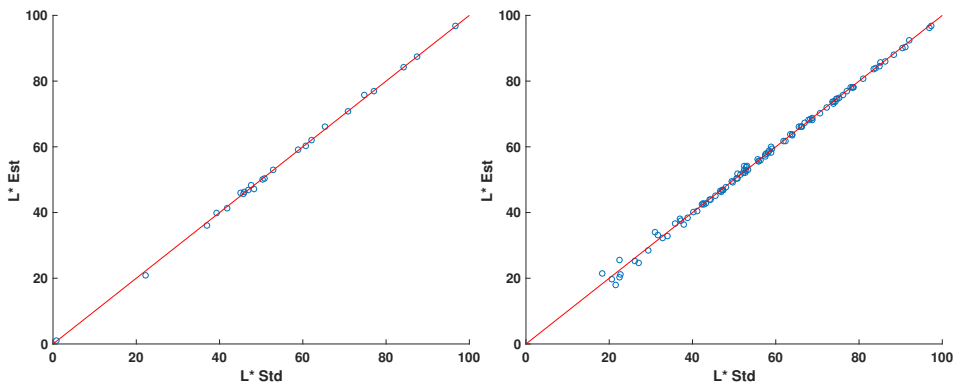
Fig. B.3. – ΔE_{00} histogram for APT calibration.



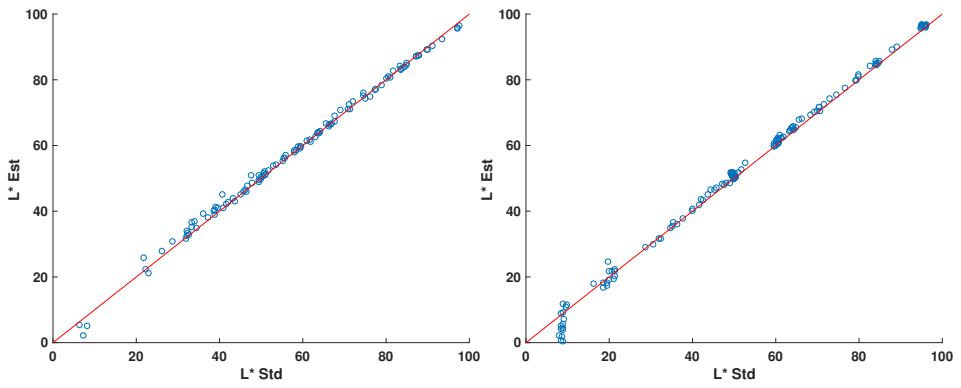
(a)Absorption filter APT verification. **(b)**Absorption filter Justin verification.



(c)Absorption filter Timo verification. **(d)**Absorption filter CCSG verification.

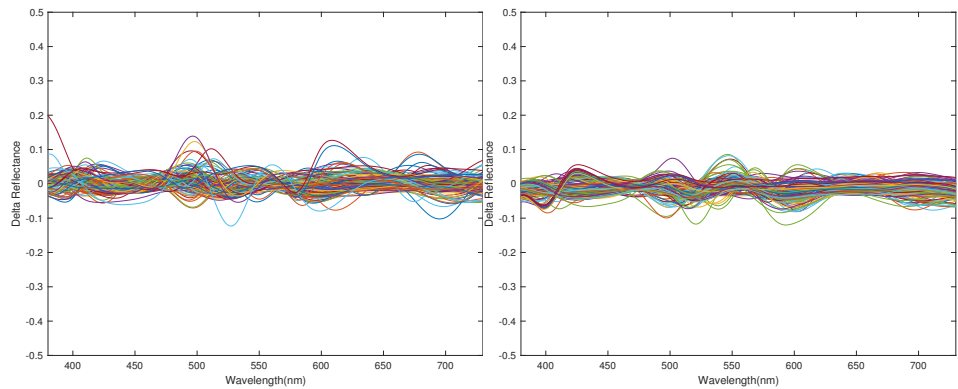


(e)Interference filter APT verification. **(f)**Interference filter Justin verification.

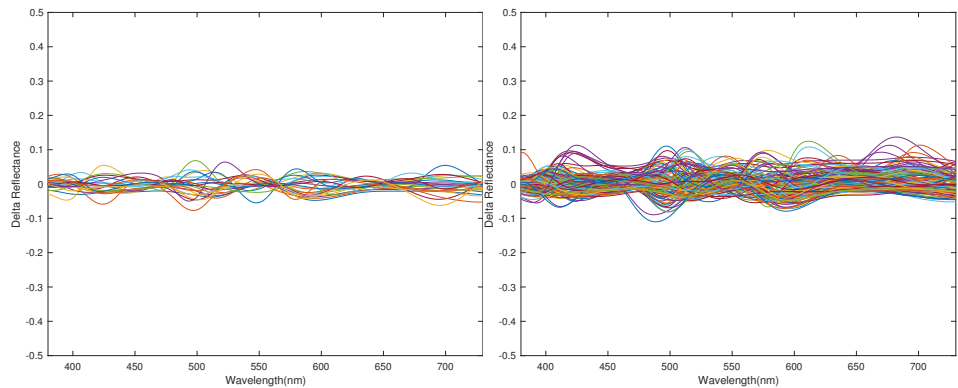


(g)Interference filter Timo verification.**(h)**Interference filter CCSG verification.

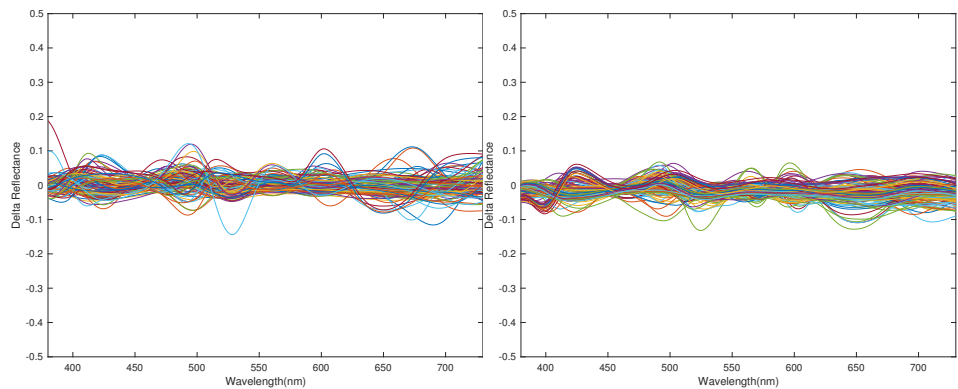
Fig. B.4. – Lightness reproduction for APT calibration.



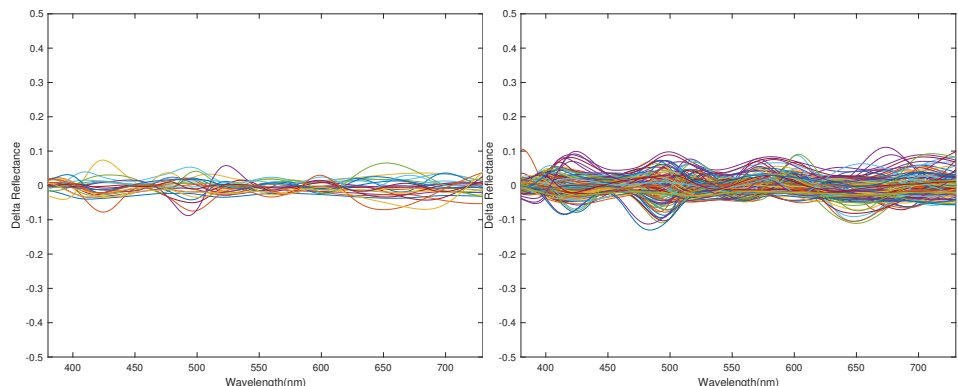
(a)Absorption filter Justin verification. **(b)**Absorption filter CCSG verification.



(c)Absorption filter APT verification. **(d)**Absorption filter Timo verification.

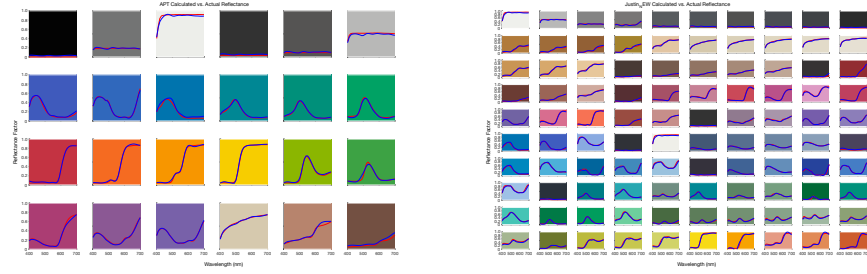


(e)Interference filter Justin verification. **(f)**Interference filter CCSG verification.

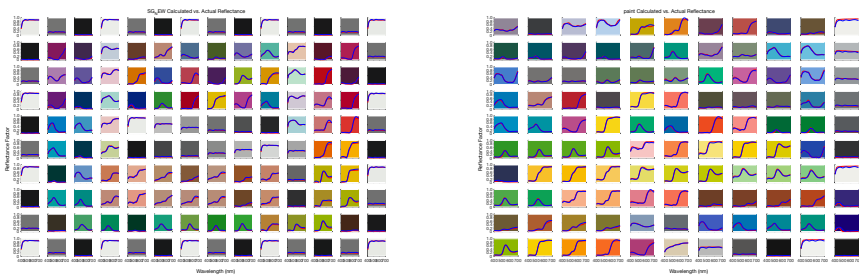


(g)Interference filter APT verification. **(h)**Interference filter Timo verification.

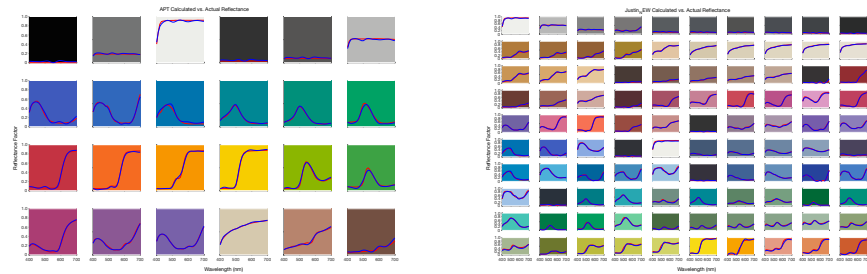
Fig. B.5. – Spectral reflectance estimation error for APT calibration.



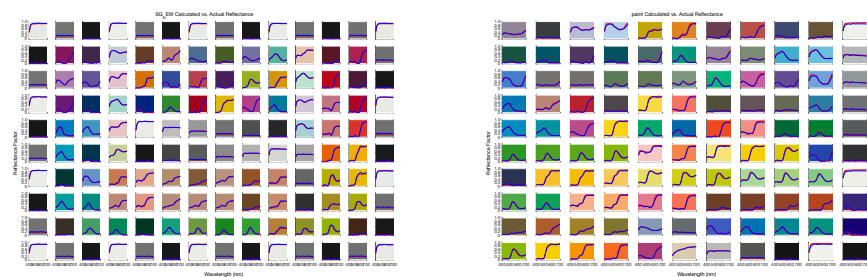
(a) Absorption filter APT verification. (b) Absorption filter Justin verification.



(c) Absorption filter CCSG verification. (d) Absorption filter Timo verification.



(e) Interference filter APT verification. (f) Interference filter Justin verification.



(g) Interference filter CCSG verification. (h) Interference filter Timo verification.

Fig. B.6. – Spectral reflectance estimation multiplots for APT calibration.

